

UNIVERSITY OF BELGRADE
FACULTY OF PHYSICS

Milan M. Radonjić

**ELECTROMAGNETICALLY INDUCED
COHERENT EFFECTS IN LASER
EXCITED RAMAN RESONANCES IN
RUBIDIUM VAPOR**

Doctoral Dissertation

Belgrade, 2012.

УНИВЕРЗИТЕТ У БЕОГРАДУ
ФИЗИЧКИ ФАКУЛТЕТ

Милан М. Радоњић

**ЕЛЕКТРОМАГНЕТСКИ ИНДУКОВАНИ
КОХЕРЕНТНИ ЕФЕКТИ У ЛАСЕРСКИ
ПОБУЂИВАНИМ РАМАНОВИМ
РЕЗОНАНЦАМА У ПАРАМА
РУБИДИЈУМА**

Докторска дисертација

Београд, 2012.

Thesis advisor, Committee member:

dr Branislav Jelenković

Principal Research Fellow

Institute of Physics, Belgrade

University of Belgrade

Committee member:

dr Milorad Kuraica

Associate Professor

Faculty of Physics

University of Belgrade

Committee member:

dr Bratislav Obradović

Assistant Professor

Faculty of Physics

University of Belgrade

Committee member:

dr Goran Poparić

Assistant Professor

Faculty of Physics

University of Belgrade

Committee member:

dr Dušan Arsenović

Principal Research Fellow

Institute of Physics, Belgrade

University of Belgrade

To my family

Захвалница

На пруженој љубави, разумевању и подршци, као и на свему што се не би могло ни побројати, захваљујем се својој породици, оцу Миливоју, мајци Љиљани, брату Милошу и сестри Миљани.

Хвала ментору др Браниславу Јеленковићу на вођењу и бројним саветима током истраживачког рада и израде докторске тезе. На многобројним дискусијама у вези истраживања, као и физике уопште, захваљујем се колеги др Александру Крмпоту. Хвала колегама Сенки, Станку, Зорану и Марини на тренуцима који су улепшали заједнички истраживачки рад.

Хвала и свим пријатељима који су непосредно или посредно допринели овом постигнућу.

Овај рад је урађен у Центру за фотонику Института за физику Универзитета у Београду и финансиран је у оквиру пројеката 141003, ИИИ45016 и ОИ171038 Министарства науке, односно Министарства просвете и науке Републике Србије.

Electromagnetically induced coherent effects in laser excited Raman resonances in rubidium vapor

Abstract

This thesis presents the theoretical analysis of various coherent effects in laser excited Raman resonances in multilevel systems in rubidium atoms. Studied coherent effects include electromagnetically induced transparency (EIT), electromagnetically induced absorption (EIA) and Stark-chirped rapid adiabatic passage (SCRAP). EIT and EIA resonances are examined in Hanle configuration in rubidium vapor vacuum cells using detailed theoretical modeling of related realistic systems. Developed numerical model provided excellent agreement with actual experimental results and their successful explanation. Furthermore, existent theory of SCRAP in two- and three-level systems is extended to the case of two and three degenerate-level manifolds with arbitrary number of substates.

Vacuum alkali-metal vapor cells are commonly used in quantum optics for research of coherent phenomena in laser-atom interaction. One of basic properties of laser radiation that influences the coherent atomic evolution is its local intensity. Generally, the coherent effects depend non-linearly on the laser intensity. Immediate consequence is that the laser beam intensity profile must affect the atomic coherent evolution. Moreover, different parts of the same laser beam should have different contribution to the coherent effects. Most common laser beam profile used in experiments is Gaussian, while theoretical models commonly assume constant intensity distribution (Π profile). One motivation of this work was the actual lack of investigation of the influence of different laser beam profiles on the coherent resonances in vacuum alkali-metal vapor cells. This thesis gives a contribution to the examination of Hanle EIT and EIA resonances using two common laser beam profiles, Gaussian and Π . Hanle EIT is studied on the open D_1 line transition $F_g = 2 \rightarrow F_e = 1$ of ^{87}Rb , while Hanle EIA is investigated on the closed transition $F_g = 2 \rightarrow F_e = 3$ at the D_2 line of the same rubidium isotope.

Study of Hanle EIT resonances from selected segments of the Gaussian laser beam cross section revealed the existence of Ramsey-like interference within a single laser beam. As the theoretical model suggested, low intensity wings of the Gaussian beam actually probe the coherently prepared atoms coming from intense

central parts of the laser beam. Hallmark of such scenario is the appearance of two Ramsey-like sideband transmission minima next to the central maximum of Hanle EIT resonances observed in the wings of the Gaussian beam. Combined with lower power broadening, this leads to narrowing of Hanle EIT resonances in the in the outer parts of the beam.

Hanle EIT from different parts of a Π -shaped laser beam cross section yielded apparently similar results, but having entirely different physical background. The sideband transmission minima appeared in EIT line shapes observed from the parts near the Π beam center. The theoretical model showed that the occurrence of these transmission minima is a joint effect of the coherent preparation of atoms into the dark state and the optical pumping into the uncoupled ground level $F_g = 1$. The optical pumping also caused the population-loss-induced transit time narrowing of EIT resonances toward the Π laser beam center. This study made clear that the profile of the laser beam determines the processes governing the evolution of atomic states during the interaction with the laser.

Hanle EIA investigations also demonstrated that the atoms experience completely different evolution depending on whether interact with one or the other profiled laser beam. This is evidenced by the analysis of EIA resonances obtained from small segments of the entire laser beam. Within the particular laser beam, Hanle EIA resonances were narrower in outer regions of the Gaussian beam, while for a Π -shaped laser beam, the narrowest resonances were obtained at the beam center. The theoretical analysis attributed the former to the lower power broadening in the Gaussian beam wings, while the latter was due to transit-time narrowing toward the center of the Π -shaped beam. These results unambiguously imply that it is important to take into account the real laser beam profile for proper modeling and analysis of coherent effects in alkali-metal vapors.

SCRAP extension for the case of two and three degenerate-levels having arbitrary number of sublevels is given as the last part of this thesis. The used approach represents a generalization of the Morris-Shore transformation to the case when the removed degeneracy of the sublevels leads to detuning from two-photon Raman resonance. Theoretical analysis of a multilevel system is facilitated by its subdivision into a set of smaller independently evolving subsystems related to the minimal-sized invariant subspaces of the Hamiltonian. Adiabatic population transfer from the starting to the final level is investigated for different types of the invariant subspaces. It is shown that the complete population transfer is achievable if the initial

state is prepared into specific coherent superpositions. An application of the developed SCRAP formalism to the ^{87}Rb atom is presented for illustration.

Keywords: coherent effects, Hanle configuration, Raman resonances, rubidium

Scientific field: Physics

Research area: Quantum optics

UDC number: 539:535.14(043.3)

Електромагнетски индуковани кохерентни ефекти у ласерски побуђиваним Рамановим резонанцама у парама рубидијума

Сажетак

Ова теза представља теоријску анализу различитих кохерентних ефеката у ласерски побуђиваним Рамановим резонанцама у системима са више нивоа у атомима рубидијума. Проучавани кохерентни ефекти укључују електромагнетски индуковану транспаренцију (ЕИТ), електромагнетски индуковану апсорпцију (ЕИА) и Штарковски брзи адијабатски прелаз (*енгл.* *SCRAP*). ЕИТ и ЕИА резонанце су испитиване у Ханле конфигурацији у вакуумским ћелијама пара рубидијума детаљним теоријским моделирањем одговарајућих реалистичних система. Развијени нумерички модел је показао одлично слагање са одговарајућим експерименталним резултатима и омогућио њихово успешно објашњење. Додатно, постојећа теорија *SCRAP*-а у системима са два и три нивоа је проширена на случајеве два и три нивоа са произвољним бројем дегенерисаних поднивоа.

Вакуумске ћелије пара алкалних метала су често коришћене у квантној оптици приликом истраживања кохерентних појава у интеракцији ласера са атомима. Једна од основних особина ласерског зрачења која утиче на кохерентну еволуцију атома је његов локални интензитет. Уопштено гледано, кохерентни ефекти зависе нелинеарно од интензитета ласера. Непосредна последица тога је да профил интензитета ласерског снопа мора утицати на кохерентну атомску еволуцију. Штавише, различити делови једног истог ласерског снопа требало би да различито доприносе кохерентним ефектима. У експериментима је Гаусов профил ласерског снопа најчешће коришћен, док теоријски модели обично претпостављају равномерну расподелу интензитета (П профил). Један од мотива овог рада је био присутни недостатак истраживања утицаја различитих профила ласерског снопа на кохерентне резонанце у вакуумским ћелијама пара алкалних метала. Ова теза даје допринос испитивању Ханле ЕИТ и ЕИА резонанци коришћењем двају честих ласерских профила, Гаусовог и П. Ханле ЕИТ је проучавана на отвореном прелазу $F_g = 2 \rightarrow F_e = 1$ линије D_1 изотопа ^{87}Rb , док је Ханле ЕИА испитивана на затвореном прелазу $F_g = 2 \rightarrow F_e = 3$

линије D_2 истог изотопа рубидијума.

Изучавање Ханле ЕИТ резонанци добијених од одређених делова попречног пресека Гаусовог ласерског снопа открило је постојање интерференције сличне Ремзијевој и то у оквиру једног ласерског снопа. Теоријски модел је указао да крила Гаусовог снопа која су ниског интензитета заправо пробају кохерентно припремљене атоме који долазе из врло интензивних централних делова ласерског снопа. Ознака поменутих процеса је појава двају трансмисионих минимума Ремзијевог типа непосредно уз централни максимум Ханле ЕИТ резонанци које су добијене у крилима Гаусовог снопа. У садејству са умањеним ширењем услед снаге, поменути процеси доводе до сужавања Ханле ЕИТ резонанци добијених у спољашњим деловима ласерског снопа.

Ханле ЕИТ добијена од различитих делова попречног пресека Π ласерског снопа дала је наизглед сличне резултате, али са сасвим другачијом физичком позадином. Два трансмисиона минимума су се појавила у ЕИТ облицима линија добијених од централних делова Π снопа. Теоријски модел је показао да је појава тих трансмисионих минимума последица садејства кохерентног припремања атома у тамно стање и оптичког пумпања у неспрегнути основни ниво $F_g = 1$. Оптичко пумпање је такође узроковало сужавање ЕИТ резонанци услед губитка насељености, током времена прелета атома ка центру Π ласерског снопа. Ово истраживање је јасно показало да профил ласерског снопа одређује који процеси управљају еволуцијом атомских стања током интеракције са ласером.

Проучавање Ханле ЕИА је такође показало да атоми еволуирају сасвим другачије зависно од тога да ли интерагују са ласерским снопом једног или другог профила. То је поткрепљено анализом ЕИА резонанци добијених од малих делова ласерског снопа. У једном одређеном снопу, Ханле ЕИА резонанце су биле уже у спољашњим деловима Гаусовог снопа, док су у случају Π снопа најуже резонанце добијене у самом његовом центру. Теоријска анализа је пређашње приписала смањеном ширењу услед снаге у крилима Гаусовог снопа, док је потоње последица сужавања током времена прелета атома ка центру Π снопа. Ови резултати недвосмислено указују да је неопходно узети у обзир стварни профил ласерског снопа ради моделирања и анализе кохерентних ефеката у парама алкалних метала.

Проширење *SCRAP*-а на системе два или три нивоа са поднивоима је дато у последњем делу тезе. Коришћени приступ представља уопштење Морис-

Шорове трансформације на случај када уклоњена дегенерација поднивоа доводи до раздешавања дво-фотонске Раманове резонанце. Теоријска анализа оваквог система са више нивоа је омогућена поделом на мање подсистеме који еволуирају независно и повезани су са минималним инваријантним потпросторима Хамилтонијана. Испитан је адијабатски пренос насељености од полазног до крајњег нивоа за различите врсте инваријантних потпростора. Показано је да се потпуни пренос насељености може остварити уколико почетно стање одговара одређеним кохерентним суперпозицијама. Дата је примена развијеног *SCRAP* формализма на атом ^{87}Rb ради сликовитости.

Кључне речи: кохерентни ефекти, Ханле конфигурација, Раманове резонанце, рубидијум

Научна област: Физика

Област истраживања: Квантна оптика

УДК број: 539:535.14(043.3)

Contents

Contents	x
1 Introduction	1
2 Theoretical basics	7
2.1 Interaction of laser radiation with two-level atomic system	7
2.2 Interaction of laser radiation with three-level atomic system	9
2.2.1 Electromagnetically induced transparency	11
2.3 Interaction of laser radiation with multilevel atomic system	13
3 Influence of laser intensity and beam profile on Hanle resonances	20
3.1 Influence of the laser beam profile on the transient atomic evolution .	21
3.2 Experimental setup	25
3.3 Hanle EIT resonances from selected segments of the Gaussian laser beam cross section	28
3.4 Hanle EIT resonances from selected segments of the Π -shaped laser beam cross section	34
3.5 Influence of laser beam profile on Hanle EIA	46
4 Stark-chirped rapid adiabatic passage	54
4.1 Adiabatic passage	54
4.1.1 Two-state SCRAP	58
4.1.2 Three-state SCRAP	59
4.2 SCRAP in a two-level atom	62
4.2.1 SCRAP among two hyperfine levels in ^{87}Rb	66
4.3 SCRAP in a three-level atom	71
4.3.1 SCRAP among three hyperfine levels in ^{87}Rb	74
5 Conclusion	80
References	84

1. Introduction

One of currently very attractive research areas in physics is quantum optics. It combines the opportunity to cope with fundamental quantum features of matter and the prospects of harnessing them for technological advancement. The groundwork of quantum optics is light-matter interaction. One of the extensively investigated aspects is the interaction of laser light and atomic vapors. That utterly rich playground keeps providing an ongoing interest for many emergent electromagnetically induced coherent effects, especially in laser excited alkali-metal-atom vapors. The main reason for such trend is the opportunity for numerous applications. Additionally, in-depth examination of coherent effects, transfer of coherence and transfer of population, leads to better understanding of various phenomena in quantum optics and laser-matter interaction in general.

Typical examples of coherent effects are those originating from coupling a single atomic excited state with two long-lived ground atomic states using two laser fields, pump and probe (so called Λ configuration). This system enables the realization of the interference between the two transition pathways generated by the laser fields and the creation of so called dark states - coherent superpositions between the long-lived states uncoupled to the excited state having quite remarkable features. Namely, when the pair of laser fields in Raman resonance between the ground atomic states prepare the absorbing medium into the dark state, it becomes more transparent for the pair of fields than it would be for each separate resonant laser field. This is basic physical picture of coherent population trapping (CPT) [1, 2] and electromagnetically induced transparency (EIT) [3, 4]. CPT and EIT can also be observed in multilevel systems as those involving two atomic degenerate-level manifolds having multiple Zeeman substates. The observation of CPT and EIT in such systems is also a direct consequence of the existence of a dark state(s) within the ground atomic level when $F_g \geq F_e$ (F_g and F_e being the angular momenta quantum numbers of the ground and excited state, respectively). The pump-probe spectroscopy of multilevel

systems with $0 < F_g < F_e$ also yields resonances in the laser transmission when the Raman resonance condition between ground-state Zeeman substates is fulfilled. However, in this case, the resonances show increased laser field absorption and have consequently being termed as electromagnetically induced absorption (EIA) [5, 6]. Contrary to CPT and EIT, the EIA resonances cannot be related to the existence of dark state(s) within the ground state. EIA is shown to be due to transfer of coherence via spontaneous emission, from the excited to the ground states, and due to transfer of population [7, 8]. Coherent effects can alternatively be studied in so called Hanle configuration [9, 10] consisting of a single linearly or elliptically polarized laser beam where external magnetic field provides detuning from the Raman resonance. Another coherent effect related to multilevel atomic systems is rapid adiabatic passage [11, 12] where using adiabatic evolution of the atomic states and the avoided crossings of diabatic energies, the complete population transfer among two atomic states can be obtained. Recently proposed technique of Stark-chirped rapid adiabatic passage (SCRAP) [13] presents a very robust and efficient method for producing complete population transfer between two bound states of an atomic or molecular system.

Narrow CPT and EIT resonances have important role in optical metrology, primarily in magnetometry [14, 15, 16], spectroscopy [17, 18] and frequency standards [19]. Availability of reliable diode lasers having tunable wavelength resulted in the expansion of the experiments and applications related to the coherent effects. Magnetometers based on the alkali-metal vapors are capable of measuring extremely weak magnetic fields, i.e. magnetic fields of the heart and of the brain [20]. Atomic clocks operating on the base of CPT and EIT effects are highly stable and can be made chip-scale [21]. For all applications narrowing of the resonances is the most important. For this to be achieved, it is essential thorough understanding of coherent effects, their mechanisms and consequences. Further development of the experimental methods for the narrowing of the emerging resonances is tied to our knowledge of the laser-matter interaction. On the other side, examination of the dependence of the resonance line-shapes on various experimental parameters reveals the details of the interaction of the laser and the atomic systems. In vacuum atomic vapor cells the resonance line-widths depend on the atomic interaction time with the laser beam as well as on the actual laser beam profile. In order to increase the atomic interaction time, buffer gas is added into the alkali-metal vapor cells. Collisions with the buffer gas preserve the alkali-metal laser induced coherence and

significantly reduce their mean free path. This can lead to the resonances of the width below 50 Hz [22]. Alternatively, vapor cells with paraffin-coated walls also provide resonance narrowing [23]. Paraffin coating enables the alkali-metal atoms to keep the coherence even after few thousands of collisions with the cell walls.

In the alkali-metal vapor vacuum cells the atomic motion at low pressures is rectilinear and disturbed only by the collisions with the cell walls. The atomic states continually evolve during the transient interaction with the laser beam. Therefore, different parts of the laser beam cross section, after passing through the cell, will carry different information about the atomic state and will yield different resonances. Additional narrowing of CPT, EIT and EIA resonances can be obtained by proper selection of the beam profile and the detected segment of the laser beam. There are only a few papers dealing with the influence of the laser beam profile on EIT resonance line-shapes. The dark resonances in cesium vacuum cell obtained using Gaussian laser beam are studied in [24]. It is shown that whole-beam dark resonance line-shapes are not Lorentzians due to inhomogeneous intensity distribution of the laser beam and repeated interaction of Cs atoms at different positions in the beam. CPT linewidths for open transitions in cases of Gaussian and Π transverse laser beam profile in vacuum gas cells are analyzed theoretically in [25]. Nonlinear, monotonically increasing square-root-like CPT linewidth dependence on laser intensity was obtained for both beam profiles. The linewidths were narrower for the Gaussian than for the Π transverse profile of the laser beam. The comparison of dark resonances obtained in alkali-metal atom buffer-gas cells using Gaussian and Π laser beam profile is presented in [26, 27]. Gaussian laser beam yields non-Lorentzian, so called Rabi-Lorentzian, whole-beam resonance line-shapes in dense ^4He vapor, while detection of the laser beam segments using small aperture gives purely Lorentzian resonances exhibiting Rabi broadening corresponding to the local intensities [28]. It is shown that Laguerre Gaussian beam profile provides significant narrowing in the line shape of the Hanle EIT and EIA resonances in comparison to the Gaussian beam [29].

The development of efficient schemes for selective population transfer and preparation of atoms and molecules in well-defined quantum states is of critical importance for modern atomic and molecular physics, atom optics and quantum information. Stark-chirped rapid adiabatic passage technique enables such efficient population transfer among two atomic or molecular states using two sequential laser pulses. The pump laser pulse transfers the population from one state to another, while an

intense far off-resonant Stark laser pulse modifies the transition probability between the two states by Stark-shifting their energies. It has been shown that the proper pump pulse intensity, duration, and partial overlap with the Stark pulse produce complete population transfer from one state to another [30]. SCRAP technique was extended for complete population transfer amongst three states [31]. In that case, all three states have to be coupled simultaneously using three laser pulses. Near resonant Stokes laser pulse is applied in addition to the pump and the Stark laser pulses. Population transfer from one state to another is performed via an intermediate third state while the population of the intermediate state is maintained minimized by the proper laser pulse timing and by adiabatic evolution of the states. SCRAP is robust against the fluctuations of Rabi frequencies and temporal shape of the laser pulses and does not rely on the exact two-photon Raman resonance condition. SCRAP technique was used for very successful and robust generation of population inversion in NO molecules [32, 33]. It appears as a highly promising building block of quantum state engineering [34] and quantum computing [35].

This thesis deals with theoretical examination of the coherent effects in laser excited rubidium vapor. Organization of the thesis is as follows. Important topic will be the influence of the laser beam intensity profile on the line-shapes of Hanle EIT and EIA resonances. Considered beam profiles will be Gaussian and Π -shaped (having constant intensity all-over its cross section). It will be shown that the laser beam intensity profile strongly affects the resonance line-shapes. The same laser beam can have twofold role: role of the pump beam that coherently prepares the atoms and role of the probe beam that interferes with the coherently prepared atoms. Further study will focus on the Hanle EIT resonances from selected segments of the Gaussian laser beam cross section and the related appearance of the Ramsey effect in the single-beam EIT resonances. Different positioning of the segments along the beam radius yields markedly different resonance line-shapes, with Ramsey-like features appearing in the wings of the Gaussian beam. Analysis of the Hanle EIT resonances obtained from selected segments of the Π -shaped laser beam will reveal joint effect of the preparation of atoms into the dark state and the optical pumping into the uncoupled ground level. Hanle EIA resonances obtained using both beam profiles will also be tackled. It will be shown that outer regions of Gaussian beam, and central regions of the Π -shaped beam generate the narrowest resonances and that an atom experiences completely different evolution depending on whether traverses one or the other profiled beam. This indicates that different physical processes

determine the atomic evolution depending on the used laser beam profile. Proper understanding and interpretation of these results requires the development of the appropriate theoretical model enabling the investigation of the interaction of the Rb vapor with the laser beam of arbitrary intensity profile. Theoretical examination is based on time dependent optical Bloch equations including Maxwell-Boltzmann velocity distribution, diversity of atomic trajectories through the laser beam of a custom cylindrical symmetric intensity profile and laser induced polarization of the Rb vapor. The complete Zeeman sublevel structure of the involved hyperfine transitions is taken into account. Results of the computer simulations will enable detailed insight into various physical processes during the interaction of the atoms with the laser light in the selected beam segments and the accompanying atomic state transient evolution. Comparison of the theoretical results with the actual measurements will provide an additional support for the analysis of the related coherent effects.

Additionally, an extension of the SCRAP technique will be given. It applies to the atomic systems having two or three levels that can be degenerated with arbitrary number of substates. Employed formalism relies on the decomposition of the Hilbert space of the system into minimal invariant subspaces to which the evolution of the system is restricted. It is a generalization of the Morris-Shore transformation [36, 37] to the case when the removed degeneracy of the substates leads to detuning from two-photon Raman resonance. The possibility of SCRAP population transfer among two degenerate-level manifolds will be examined first in detail, and afterward the case of three degenerate-level manifolds will be discussed. It will be shown that the complete transfer is feasible if the initial state is prepared into specific coherent superpositions. The method will be applied to the adiabatic passage among two and three hyperfine levels in the rubidium atom.

Contents of this thesis are based on the following papers of the author:

- 1) M. Radonjić, D. Arsenović, Z. Grujić, and B. M. Jelenković, *Coherent population trapping linewidths for open transitions: Cases of different transverse laser intensity distribution*, *Physical Review A* **79**, 023805 (2009),
- 2) M. Radonjić and B. M. Jelenković, *Stark-chirped rapid adiabatic passage among degenerate-level manifolds*, *Physical Review A* **80**, 043416 (2009),
- 3) A. J. Krmpot, S. M. Ćuk, S. N. Nikolić, M. Radonjić, D. G. Slavov, and B.

M. Jelenković, *Dark Hanle resonances from selected segments of the Gaussian laser beam cross-section*, *Optics Express* **17**, 22491 (2009),

4) S. M. Ćuk, M. Radonjić, A. J. Krmpot, S. N. Nikolić, Z. D. Grujić, and B. M. Jelenković, *Influence of laser beam profile on electromagnetically induced absorption*, *Physical Review A* **82**, 063802 (2010),

5) A. J. Krmpot, M. Radonjić, S. M. Ćuk, S. N. Nikolić, Z. D. Grujić, and B. M. Jelenković, *Evolution of dark state of an open atomic system in constant intensity laser field*, *Physical Review A* **84**, 043844 (2011).

Other papers of the author not included in the thesis:

1) Nikola Burić and Milan Radonjić, *Uniquely defined geometric phase of an open system*, *Physical Review A* **80**, 014101 (2009),

2) M. M. Mijailović, Z. D. Grujić, M. Radonjić, D. Arsenović, and B. M. Jelenković, *Nonlinear magneto-optical rotation narrowing in vacuum gas cells due to interference between atomic dark states of two spatially separated laser beams*, *Physical Review A* **80**, 053819 (2009),

3) Milan Radonjić, Slobodan Prvanović, and Nikola Burić, *System of classical nonlinear oscillators as a coarse-grained quantum system*, *Physical Review A*, **84**, 022103 (2011),

4) M. Radonjić, S. Prvanović, and N. Burić, *Emergence of classical behavior from the quantum spin*, *Physical Review A* **85**, 022117 (2012),

5) M. Radonjić, S. Prvanović, and N. Burić, *Hybrid quantum-classical models as constrained quantum systems*, *Physical Review A* **85**, 064101 (2012),

6) N. Burić, I. Mendaš, D. B. Popović, M. Radonjić, and S. Prvanović, *Statistical ensembles in the Hamiltonian formulation of hybrid quantum-classical systems*, *Physical Review A* **86**, 034104 (2012).

2. Theoretical basics

2.1 Interaction of laser radiation with two-level atomic system

The state of a closed quantum system is described by its state vector $|\Psi(t)\rangle$ that is member of some Hilbert space \mathcal{H} . Unitary evolution of the system is described by time-dependent Schrödinger equation (TDSE)

$$i\hbar \frac{d|\Psi(t)\rangle}{dt} = \hat{H}(t)|\Psi(t)\rangle, \quad (2.1)$$

where $\hat{H}(t)$ is (possibly time-dependent) Hamiltonian operator of the system acting on the space \mathcal{H} . Schrödinger equation is linear and allows coherent superpositions. When describing the interaction of an atomic system with the laser light, the Hamiltonian has two parts:

$$\hat{H}(t) = \hat{H}^{at} + \hat{V}^{int}(t), \quad (2.2)$$

where the first, constant, part \hat{H}^{at} incorporates the unperturbed eigenenergies of the (bare) atom in the absence of the laser radiation

$$\hat{H}^{at}|\psi_n\rangle = \varepsilon_n|\psi_n\rangle, \quad n \in \{1, 2, \dots\}, \quad (2.3)$$

where $|\psi_n\rangle$ are the eigenstates corresponding to the bare atomic eigenenergies ε_n . The matrix elements of the interaction part $\hat{V}^{int}(t)$ can, in principle, be obtained from the eigenstates of the system $V_{mn}^{int}(t) = \langle\psi_m|\hat{V}^{int}(t)|\psi_n\rangle$. Usually, when dealing with the laser excitation the laser carrier frequency ω is close to some Bohr transition frequency, i.e., $\omega \approx \omega_{nm} \equiv (\varepsilon_n - \varepsilon_m)/\hbar$. In such case, there is no any appreciable population in quantum states other than those initially populated or excited by the laser. Thus although there may be an infinite number of quantum states, very few of those participate in the excitation dynamics. One can restrict attention to only a

finite N -dimensional subspace \mathcal{H}_N of the infinite Hilbert space \mathcal{H} . In this subspace the state vector $|\Psi(t)\rangle$ has the expansion

$$|\Psi(t)\rangle = \sum_{n=1}^N c_n(t) |\psi_n\rangle, \quad (2.4)$$

where the time-varying complex numbers $c_n(t)$ (termed probability amplitudes) must be chosen such that the resulting state vector satisfies the TDSE (2.1). This requirement leads to the following vectorial form of the system of N coupled ordinary differential equations for the probability amplitudes:

$$i\hbar \frac{d\mathbf{C}(t)}{dt} = \mathbf{H}(t)\mathbf{C}(t), \quad (2.5)$$

where the vector $\mathbf{C}(t) = (c_1(t), \dots, c_N(t))^T$ and the matrix $\mathbf{H}(t)$ represent the state $|\Psi(t)\rangle$ and the Hamiltonian $\hat{H}(t)$, respectively, in the basis $\{|\psi_1\rangle, \dots, |\psi_N\rangle\}$.

Although only N states appear explicitly in the expansion (2.4), the influence of other states can have important consequences. Other states are responsible for the polarizability of the atom, i.e. for the occurrence of an induced dipole moment which, when the laser field is present, supplements the direct transition dipole moment. These produce multiphoton transitions and laser-induced energy (Stark) shifts.

The predominant part of the interaction of bound particles with laser light is almost always the electric dipole interaction. In that case the interaction energy operator is associated with the projection of the electric dipole operator $\hat{\mathbf{d}}$ onto the electric field $\hat{V}^{int}(t) = -\hat{\mathbf{d}} \cdot \mathbf{E}(t)$, where $\mathbf{E}(t)$ is the time varying electric field at the center of mass of the particle. This applies to almost all commonly considered (i.e. “allowed”) transitions. The interaction operator leads to selection rules such that, for a given pair of states ψ_m and ψ_n only one polarization direction $\hat{\mathbf{e}}$ gives a nonzero transition moment $d_{mn} = \langle \psi_m | \hat{\mathbf{d}} \cdot \hat{\mathbf{e}} | \psi_n \rangle$. It is common to introduce the appropriate Rabi frequency as $\Omega_{mn}(t) = -d_{mn}\mathcal{E}(t)/\hbar$, where $\mathcal{E}(t)$ is the electric field envelope, i.e., $E(t) = \mathcal{E}(t) \cos(\omega t + \phi)$. The set of nonzero moments for the interaction operator can be viewed as a linkage pattern. The possible dipole transition moments - the possible linkages - are characteristic for any given atom or molecule. Manipulation of the state vector of an atom or molecule is possible through control of the magnitude and direction of the laser electric field $\mathbf{E}(t)$.

Consider now a two-level system with ground state $|\psi_1\rangle$ having the energy $\hbar\omega_1$

and excited state $|\psi_2\rangle$ having the energy $\hbar\omega_2$. For optical wavelengths of used laser pulses, the Rabi frequency is typically 4 or 5 orders of magnitude smaller than the laser carrier frequency ω . That is, the photon energy $\hbar\omega$ is much larger than the interaction energy. Rapid oscillations associated with the carrier frequency are not of interest. One is concerned with processes that take place over very many optical cycles. Thus, it is necessary to focus on slow dynamics by making rotating-wave approximation (RWA). It consists of replacing terms in the evolution equations rotating at optical frequencies by their zero average value. In the rotating basis of so called *adiabatic* states

$$\begin{aligned} |\tilde{\psi}_1(t)\rangle &= e^{-i\omega_1 t} |\psi_1\rangle, \\ |\tilde{\psi}_2(t)\rangle &= e^{-i(\omega_1 + \omega)t} |\psi_1\rangle \end{aligned} \quad (2.6)$$

the two-level RWA Schrödinger equation has the form

$$i\hbar \frac{d}{dt} \begin{bmatrix} c_1(t) \\ c_2(t) \end{bmatrix} = \hbar \begin{bmatrix} 0 & \frac{1}{2}\Omega(t) \\ \frac{1}{2}\Omega^*(t) & \Delta \end{bmatrix} \begin{bmatrix} c_1(t) \\ c_2(t) \end{bmatrix}, \quad (2.7)$$

where the time-dependent complex Rabi frequency is $\Omega(t) = -d_{21}\mathcal{E}(t)e^{i\phi}/\hbar$ and the laser detuning is $\Delta = \omega_2 - \omega_1 - \omega$.

2.2 Interaction of laser radiation with three-level atomic system

Extension of a two-level system with another state leads to a three-level system whose enriched complexity enables additional coherent phenomena. Let the three-level system be composed from the states $|\psi_1\rangle$, $|\psi_2\rangle$ and $|\psi_3\rangle$, having the energies $\hbar\omega_1$, $\hbar\omega_2$ and $\hbar\omega_3$, respectively. In case of the electric-dipole interaction the selection rules require that coupled states must have opposite parity. Therefore, three-level system can be dipole-excited by two distinct laser fields coupling two different dipole-allowed transitions. These two laser fields, labeled by the letters p and S are often called pump and Stokes fields, respectively. The carrier frequencies of the two fields, ω_p and ω_S , respectively, are both taken to be close to resonance with exactly one of the possible transitions. In that manner, each laser field can be uniquely associated with a single transition. Let the pump field is (near) resonant only with the $1 \rightarrow 3$ transition, while the Stokes field is (near) resonant only with the $2 \rightarrow 3$ transition.

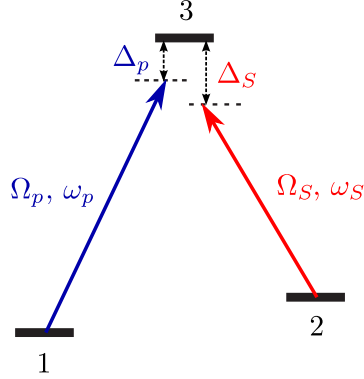


Figure 2.1: Three-level Λ system. Pump field (label p) couples the transition $1 \rightarrow 3$, while Stokes field (label S) couples the transition $2 \rightarrow 3$. Ω_p and Ω_S are Rabi frequencies of the fields, ω_p and ω_S are carrier frequencies, while Δ_p and Δ_S are transition detunings.

The transition $1 \rightarrow 2$ is dipole-forbidden and the states 1 and 2 are long-lived (ground states) comparing to the state 3 (excited state). Then, the nonzero dipole interactions are

$$V_p(t) = -d_{31}\mathcal{E}_p(t) \cos(\omega_p t + \phi_p), \quad V_S(t) = -d_{32}\mathcal{E}_S(t) \cos(\omega_S t + \phi_S), \quad (2.8)$$

where d_{13} and d_{23} are the dipole moments of the transitions and $\mathcal{E}_p(t)$ and $\mathcal{E}_S(t)$ are slowly varying amplitudes of the laser fields. One can introduce the corresponding Rabi frequencies as $\Omega_p(t) = -d_{31}\mathcal{E}_p(t)/\hbar$ and $\Omega_S(t) = -d_{32}\mathcal{E}_S(t)/\hbar$.

The state vector of a three-level system can be expanded as

$$|\Psi(t)\rangle = c_1(t)|\tilde{\psi}_1(t)\rangle + c_2(t)|\tilde{\psi}_2(t)\rangle + c_3(t)|\tilde{\psi}_3(t)\rangle, \quad (2.9)$$

where

$$\begin{aligned} |\tilde{\psi}_1(t)\rangle &= e^{-i\omega_1 t}|\psi_1\rangle, \\ |\tilde{\psi}_2(t)\rangle &= e^{-i(\omega_1 + \omega_p - \omega_S)t}|\psi_2\rangle, \\ |\tilde{\psi}_3(t)\rangle &= e^{-i(\omega_1 + \omega_p)t}|\psi_3\rangle \end{aligned} \quad (2.10)$$

are the diabatic basis states in the rotating frame. The evolution is governed by the

three-level RWA Schrödinger equation which in the diabatic basis has the form

$$i\hbar \frac{d}{dt} \begin{bmatrix} c_1(t) \\ c_2(t) \\ c_3(t) \end{bmatrix} = \hbar \begin{bmatrix} 0 & 0 & \frac{1}{2}\Omega_p(t) \\ 0 & \Delta_p - \Delta_S & \frac{1}{2}\Omega_S(t) \\ \frac{1}{2}\Omega_p^*(t) & \frac{1}{2}\Omega_S^*(t) & \Delta_p \end{bmatrix} \begin{bmatrix} c_1(t) \\ c_2(t) \\ c_3(t) \end{bmatrix}, \quad (2.11)$$

where $\Delta_p = \omega_3 - \omega_1 - \omega_p$ and $\Delta_S = \omega_3 - \omega_2 - \omega_S$ are appropriate single-photon detunings of the pump and Stokes field, respectively. Difference between two detunings $\Delta_R = \Delta_p - \Delta_S$ is known as Raman two-photon detuning and $\Delta_R = 0$ corresponds to a Raman two-photon resonance condition. The type of three-level system relevant for this thesis, called Λ system, is given in Figure 2.1. Other two possible types, V and ladder, are not of present interest.

2.2.1 Electromagnetically induced transparency

Three-level Λ system represents the simplest system presenting two physically closely related coherent phenomena - coherent population trapping (CPT) and electromagnetically induced transparency (EIT). Basic physical picture of these phenomena is based on the existence of *dark states* that are uncoupled to the laser fields. The atoms trapped into the dark state cannot be further excited by the laser fields and cannot fluoresce - they are dark.

Let us consider the case when the two fields are in Raman resonance $\Delta_R = 0$, i.e., single-photon detunings are equal $\Delta_p = \Delta_S = \Delta$. The Λ system Hamiltonian

$$W(t) = \hbar \begin{bmatrix} 0 & 0 & \frac{1}{2}\Omega_p(t) \\ 0 & 0 & \frac{1}{2}\Omega_S(t) \\ \frac{1}{2}\Omega_p^*(t) & \frac{1}{2}\Omega_S^*(t) & \Delta \end{bmatrix} \quad (2.12)$$

has the following eigenstates and eigenenergies

$$\Phi_0(t) = \frac{1}{\Omega(t)} \begin{bmatrix} \Omega_S^*(t) \\ -\Omega_p^*(t) \\ 0 \end{bmatrix}, \quad \varepsilon_0(t) = 0, \quad (2.13)$$

$$\Phi_-(t) = \frac{1}{\Omega(t)} \begin{bmatrix} \Omega_p(t) \cos \theta(t) \\ \Omega_S(t) \cos \theta(t) \\ -\Omega(t) \sin \theta(t) \end{bmatrix}, \quad \varepsilon_-(t) = \frac{\hbar}{2}(\Delta - \sqrt{\Delta^2 + \Omega(t)^2}), \quad (2.14)$$

$$\Phi_+(t) = \frac{1}{\Omega(t)} \begin{bmatrix} \Omega_p(t) \sin \theta(t) \\ \Omega_S(t) \sin \theta(t) \\ \Omega(t) \cos \theta(t) \end{bmatrix}, \quad \varepsilon_+(t) = \frac{\hbar}{2}(\Delta + \sqrt{\Delta^2 + \Omega(t)^2}), \quad (2.15)$$

where the ‘‘mixing angle’’ $\theta(t)$ is introduced as $\cot(2\theta(t)) = \Delta/\Omega(t)$, with $\Omega(t) = \sqrt{|\Omega_p(t)|^2 + |\Omega_S(t)|^2}$. It is important to note that the states $\Phi_{\pm}(t)$ retain components of all of the atomic states. In contrast, the state $\Phi_0(t)$ is composed entirely from ground states 1 and 2 and has no contribution of the excited state 3. Moreover, the state $\Phi_0(t)$ is a dark state that is effectively decoupled from the excited state 3, since $W(t)\Phi_0(t) = 0$. This decoupling is consequence of destructive interference of probability amplitude for the transition $1 \rightarrow 3$ with probability amplitude for the transition $2 \rightarrow 3$. If the medium is prepared in this state, there is no possibility of excitation by means of the coupling laser fields. This leads to an enhanced transparency of the medium when the laser fields are close to Raman resonance. Increased transparency for near resonant coupling fields is common to CPT and EIT. Preparation into the dark state via optical pumping (via spontaneous decay from the excited state 3) is one way to trap population into that state. Note once again that necessary conditions for the CPT and EIT appearance are the existence of dark states and two-photon Raman resonance of the coupling laser fields.

In a strict sense, EIT relates to the induced transparency of a weak probe field in addition of a strong pump field, coupling one of the states of the original transition to a third state. The difference between EIT and CPT is that CPT relates to two fields of nearly equal Rabi frequencies. EIT and CPT can be found in systems with different types of level structures having different number of levels [2]. Possible realizations include pump-probe and Hanle configuration. The later utilizes single linearly or elliptically polarized laser beam whose circular components couple Zeeman sublevels of appropriate level manifolds and form Λ scheme(s). Detuning from the Raman resonance is realized by an external axial magnetic field that lifts Zeeman degeneracy. The material presented in this thesis deals with Hanle EIT in multilevel systems in rubidium atoms. Previous exposition of EIT and CPT is very simplistic, capturing the essence of the phenomena. Full treatment must include the relaxation effects that are inevitable in atomic systems, like spontaneous emission. This is naturally carried out using the master equation approach where the relaxation effects are treated via appropriate Lindblad-form terms [38, 39, 40].

2.3 Interaction of laser radiation with multilevel atomic system

Hyperfine atomic structure offers the possibility of studying coherent effects in multilevel systems. Hyperfine levels are degenerate in the absence of a magnetic field. The Zeeman degeneracy can be intentionally lifted by applying an external magnetic field, like in Hanle configuration experiments. Hanle EIT (EIA) resonances are usually related to hyperfine atomic transitions $F_g \rightarrow F_e = F_g - 1$ ($F_g \rightarrow F_e = F_g + 1$), where F_g and F_e are angular momentum quantum numbers of the ground- and excited-state hyperfine levels, respectively. External magnetic field \mathbf{B} removes the degeneracy of Zeeman sublevels of both the ground and the excited hyperfine levels and favors the choice of quantization axis. Hence, the quantization z axis is chosen to be parallel to the external magnetic field, i.e. $\mathbf{B} = B\mathbf{e}_z$. The ground and the excited hyperfine states are coupled by a linearly polarized laser beam propagating along the z axis. The laser frequency ω_0 is chosen to be resonant with the considered atomic transition. The theoretical model is based on time-dependent optical Bloch equations (OBEs) for the density matrix of a moving atom. Under the assumption of purely radiative relaxation the equations are of the form [41]

$$\frac{d\hat{\rho}}{dt} = -\frac{i}{\hbar} [\hat{H}_{\text{atom}}(B) + \hat{V}_{\text{int}}(t), \hat{\rho}] + \left(\frac{d\hat{\rho}}{dt} \right)_{\text{SE}}, \quad (2.16)$$

where

$$\hat{H}_{\text{atom}}(B) = \sum_{j=-F_g}^{F_g} \hbar\omega_{g_j}(B) |g_j\rangle\langle g_j| + \sum_{k=-F_e}^{F_e} \hbar\omega_{e_k}(B) |e_k\rangle\langle e_k|, \quad (2.17)$$

is the atomic Hamiltonian related to ground (excited) states $|g_j\rangle \equiv |F_g, m_{g_j} = j\rangle$ ($|e_k\rangle \equiv |F_e, m_{e_k} = k\rangle$) with Zeeman-shifted energies $\hbar\omega_{g_j}(B) = \hbar\omega_{g_0} + \mu_B g_{F_g} B m_{g_j}$ ($\hbar\omega_{e_k}(B) = \hbar\omega_{e_0} + \mu_B g_{F_e} B m_{e_k}$). μ_B is the Bohr magneton and g_{F_g} and g_{F_e} are the Landé factors for the appropriate hyperfine levels. Dipole laser-atom interaction is

$$\hat{V}_{\text{int}}(t) = - \sum_{j=-F_g}^{F_g} \sum_{k=-F_e}^{F_e} \mathbf{E}(t) \cdot \mathbf{d}_{jk} (|g_j\rangle\langle e_k| + |e_k\rangle\langle g_j|), \quad (2.18)$$

where $\mathbf{E}(t)$ is the time-dependent laser electric field and $\mathbf{d}_{jk} = \langle g_j | \hat{\mathbf{d}} | e_k \rangle$ is the atomic electric dipole moment for the transition between the states $|g_j\rangle$ and $|e_k\rangle$.

Spontaneous emission is included through the Lindblad-form term

$$\left(\frac{d\hat{\rho}}{dt}\right)_{\text{SE}} = \frac{\Gamma}{2} \sum_{j,k} (2\hat{A}_{jk}\hat{\rho}\hat{A}_{jk}^\dagger - \hat{A}_{jk}^\dagger\hat{A}_{jk}\hat{\rho} - \hat{\rho}\hat{A}_{jk}^\dagger\hat{A}_{jk}), \quad (2.19)$$

where Γ is the decay rate of each excited sublevel and \hat{A}_{jk} are Lindblad operators corresponding to dipole transitions from the excited- to ground-state manifold. In the rotating wave approximation the OBEs for the density matrix of a moving atom have the form [25]

$$\begin{aligned} \frac{d\rho_{g_j g_k}}{dt} &= i(\omega_{g_k} - \omega_{g_j}) \rho_{g_j g_k} + \frac{i}{\hbar} \sum_{m=-F_e}^{F_e} \left(\tilde{\rho}_{g_j e_m} V_{-e_m g_k} - V_{+g_j e_m} \tilde{\rho}_{e_m g_k} \right) \\ &+ (-1)^{j+k} (2F_e + 1) \Gamma_{F_e \rightarrow F_g} \sum_{q=-1}^1 \rho_{e_{j+q} e_{k+q}} \begin{pmatrix} F_e & 1 & F_g \\ k+q & -q & -k \end{pmatrix} \begin{pmatrix} F_e & 1 & F_g \\ j+q & -q & -j \end{pmatrix}, \\ \frac{d\tilde{\rho}_{e_k g_j}}{dt} &= \left(i(\omega_L + \omega_{g_j} - \omega_{e_k}) - \frac{\Gamma}{2} \right) \tilde{\rho}_{e_k g_j} + \frac{i}{\hbar} \left(\sum_{m=-F_e}^{F_e} \rho_{e_k e_m} V_{-e_m g_j} - \sum_{\ell=-F_g}^{F_g} V_{-e_k g_\ell} \rho_{g_\ell g_j} \right), \\ \frac{d\rho_{e_j e_k}}{dt} &= \left(i(\omega_{e_k} - \omega_{e_j}) - \Gamma \right) \rho_{e_j e_k} + \frac{i}{\hbar} \sum_{\ell=-F_g}^{F_g} \left(\tilde{\rho}_{e_j g_\ell} V_{+g_\ell e_k} - V_{-e_j g_\ell} \tilde{\rho}_{g_\ell e_k} \right), \end{aligned} \quad (2.20)$$

where $(:::)$ denotes Wigner $3-j$ symbol. Diagonal density matrix elements $\rho_{g_j g_j}$ ($\rho_{e_k e_k}$) are populations of g_j (e_k) Zeeman sublevels, while off-diagonal elements $\rho_{g_j g_k}$ ($\rho_{e_j e_k}$) are Zeeman coherences between $g_j g_k$ ($e_j e_k$) sublevels. Fast oscillations of the optical coherences $\rho_{e_j g_k}$ were eliminated by standard substitution $\rho_{e_j g_k} = \tilde{\rho}_{e_j g_k} e^{-i\omega_0 t}$. $\omega_L = \omega_0(1 - v_{\parallel}/c)$ is the Doppler-shifted laser frequency seen by a moving atom and v_{\parallel} is the of the atomic velocity component parallel to the laser propagation direction. $\Gamma_{F_e \rightarrow F_g}$ is the decay rate from each sublevel of the excited level F_e to one ground hyperfine level F_g [41]

$$\Gamma_{F_e \rightarrow F_g} = (2J_e + 1)(2F_g + 1) \left\{ \begin{matrix} J_g & J_e & 1 \\ F_e & F_g & I_n \end{matrix} \right\}^2 \Gamma, \quad (2.21)$$

where J_g , J_e and I_n represent the electron and nuclear angular momentum quantum numbers and $\{:::\}$ represents Wigner $6-j$ symbol. According to sum rule $\sum_{F'_g} \Gamma_{F_e \rightarrow F'_g} = \Gamma$, openness of the atomic system is quantitatively given by the ratio $\Gamma_{F_e \rightarrow F_g}/\Gamma$. The ratio is less than 1 for open and exactly 1 for closed systems. In

case of an open system, one could also include the equations for the density matrix elements related to the other ground levels $F'_g \neq F_g$. However, those equations can be safely disregarded since those levels are not coupled by the laser. Because a Doppler-broadened atomic vapor is considered, inclusion of higher excited levels into the analysis may become necessary depending on the ratio of the Doppler-width and excited level hyperfine splittings.

In a general case, the laser electric field is given by

$$\mathbf{E}(\mathbf{r}, t) = \mathbf{e}_x E_{0x}(\mathbf{r}, t) \cos(\omega_0 t - \mathbf{k}\mathbf{r}) + \mathbf{e}_y E_{0y}(\mathbf{r}, t) \cos(\omega_0 t - \mathbf{k}\mathbf{r} + \varphi_{yx}). \quad (2.22)$$

For symmetry reasons it is suitable to express the laser electric field in terms of the spherical basis unit vectors $\mathbf{u}_{\pm 1} = (\mp \mathbf{e}_x - i \mathbf{e}_y) / \sqrt{2}$

$$\mathbf{E} = \mathbf{u}_1 (E_{1,+} e^{i(\omega_0 t - \mathbf{k}\mathbf{r})} + E_{1,-} e^{-i(\omega_0 t - \mathbf{k}\mathbf{r})}) + \mathbf{u}_{-1} (E_{-1,+} e^{i(\omega_0 t - \mathbf{k}\mathbf{r})} + E_{-1,-} e^{-i(\omega_0 t - \mathbf{k}\mathbf{r})}), \quad (2.23)$$

where we used the notation $E_{\pm 1, \pm} = (\mp E_{0x} + i e^{\pm i \varphi_{yx}} E_{0y}) / (2\sqrt{2})$. Terms $V_{\pm g_j e_k}$ in OBEs (2.20) are of the form

$$V_{\pm g_j e_k} = -\mu_{g_j e_k, -1} E_{-1, \pm} - \mu_{g_j e_k, 1} E_{1, \pm}. \quad (2.24)$$

Here $\mu_{g_j e_k, q}$ is the electric dipole matrix element between the ground and excited states $|g_j\rangle$ and $|e_k\rangle$, respectively, and it can be calculated as [41]

$$\begin{aligned} \mu_{g_j e_k, q} &= \langle F_g, m_{g_j} | \mathbf{u}_q \cdot \hat{\mathbf{d}} | F_e, m_{e_k} \rangle \\ &= \langle J_g || \hat{\mathbf{d}} || J_e \rangle (-1)^{J_g + I_n + m_{g_j}} \sqrt{(2F_g + 1)(2F_e + 1)(2J_g + 1)} \\ &\quad \times \begin{Bmatrix} J_g & J_e & 1 \\ F_e & F_g & I_n \end{Bmatrix} \begin{pmatrix} F_e & 1 & F_g \\ m_{e_k} & q & -m_{g_j} \end{pmatrix}, \end{aligned} \quad (2.25)$$

where $\langle J_g || \hat{\mathbf{d}} || J_e \rangle$ is the reduced matrix element of the electric dipole operator between the appropriate ground and excited states. Due to the relation $\mu_{e_k g_j, q}^* = (-1)^q \mu_{g_j e_k, -q}$, the terms $V_{\pm e_k g_j}$ are completely determined by the terms $V_{\mp g_j e_k}$.

It is assumed that after colliding with cell walls, atoms reset into an internal state with equally populated ground magnetic sublevels. Between collisions with cell walls, rubidium atoms interact only with the axially oriented homogeneous magnetic field and spatially dependent stationary laser electric field. The magnetic field is

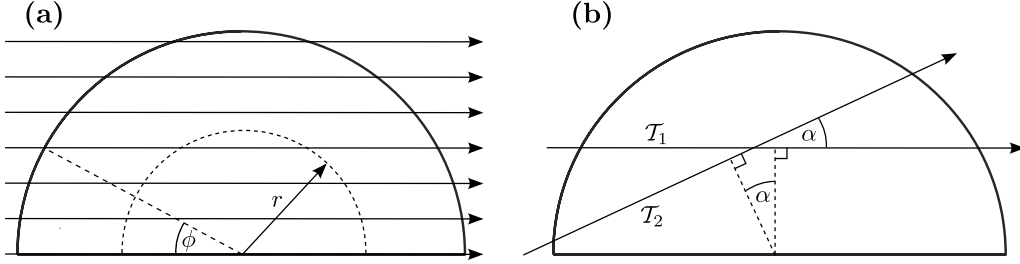


Figure 2.2: (a) Schematic of atomic trajectories chosen to cover the entire laser beam cross section (horizontal straight lines). Each trajectory defines certain angle ϕ . All trajectories intersecting the circle of radius r contribute to density matrix $\rho(B; r)$. (b) Two atomic trajectories \mathcal{T}_1 and \mathcal{T}_2 , related by rotation by the angle α about the beam axis, are equivalent due to cylindrical symmetry.

taken constant during the atomic transit through the laser beam. Collisions among Rb atoms are negligible due to very low Rb vapor pressure at room temperature, so an atom moves through the laser beam with constant velocity $\mathbf{v} = \mathbf{v}_{\parallel} + \mathbf{v}_{\perp}$, where \mathbf{v}_{\parallel} and \mathbf{v}_{\perp} are velocity components parallel and perpendicular to laser propagation direction, respectively. The former affects the longitudinal direction of the atomic trajectory and Doppler shift of the laser frequency seen by a moving atom, while the latter determines the transverse direction of the trajectory and the interaction time. Longitudinal changes of the beam profile are negligible comparing to transverse ones so that only the transverse direction of the trajectory matters. Therefore, the explicit dependence on z of all physical quantities related to the Rb vapor is dropped. From the reference frame of the moving atom, the electric field varies and the rate of variation depends only on \mathbf{v}_{\perp} . Assume that the transverse projection of the atomic trajectory is given by $\mathbf{r}_{\perp}(t) = \mathbf{r}_{0\perp} + \mathbf{v}_{\perp}t$, where $\mathbf{r}_{0\perp}$ is the perpendicular component of the atom position vector at $t = 0$. The temporal variation of the laser electric field seen by the moving atom is given by

$$\mathbf{E}(t) \equiv \mathbf{E}(\mathbf{r}_{\perp}(t)) = \mathbf{E}(\mathbf{r}_{0\perp} + \mathbf{v}_{\perp}t), \quad (2.26)$$

representing the spatial laser electric field variation along the trajectory of the atom in the laboratory frame. When the beam profile is cylindrical symmetric, the spatial dependence becomes purely radial dependence.

The observed resonances in EIT and EIA experiments are a probabilistic average of the contributions of many individual, mutually non-interacting atoms. Ru-

idium atoms traverse the laser beam at different trajectories with different velocities. Maxwell-Boltzmann velocity distribution and diversity of atomic trajectories through the laser beam are taken into account. The trajectories having different distances from the laser beam center are chosen so that the beam cross section is suitably covered (Fig. 2.2(a)). Each trajectory corresponds to a certain azimuthal angle ϕ_v of the atomic velocity $\mathbf{v} \equiv (v_{\parallel}, v_{\perp}, \phi_v)$. Let trajectories \mathcal{T}_1 and \mathcal{T}_2 , shown in Fig. 2.2(b), correspond to velocities $\mathbf{v}_1 \equiv (v_{\parallel}, v_{\perp}, \phi_{v1})$ and $\mathbf{v}_2 \equiv (v_{\parallel}, v_{\perp}, \phi_{v2})$, respectively. Owing to the cylindrical symmetry of the laser beam profile, atomic density matrices $\rho(B; \mathbf{v}_1; \mathbf{r}_{\perp})$ and $\rho(B; \mathbf{v}_2; \mathbf{r}_{\perp})$ calculated along those trajectories are the same up to a rotation by the angle α about the laser beam axis. Therefore, the trajectories \mathcal{T}_1 and \mathcal{T}_2 may be considered as equivalent and it is enough to perform the actual calculations only along the trajectories like those in Fig. 2.2(a).

The goal is to obtain the atomic ensemble density matrix $\rho(B; r)$ across the beam cross section. Starting step is to calculate the atomic density matrix $\rho(B; \mathbf{v}; \mathbf{r}_{\perp})$ along a given trajectory for a representative set of atomic velocities. The calculated density matrices are then averaged over the longitudinal and transverse parts of the Maxwell-Boltzmann distribution of velocities yielding

$$\rho(B; \phi_v; \mathbf{r}_{\perp}) = \int_0^{\infty} dv_{\perp} W_{\perp}(v_{\perp}) \int_{-\infty}^{\infty} dv_{\parallel} W_{\parallel}(v_{\parallel}) \rho(B; v_{\parallel}, v_{\perp}, \phi_v; \mathbf{r}_{\perp}), \quad (2.27)$$

with

$$W_{\parallel}(v_{\parallel}) = \frac{1}{u\sqrt{\pi}} \exp(-v_{\parallel}^2/u^2), \quad W_{\perp}(v_{\perp}) = \frac{2v_{\perp}}{u^2} \exp(-v_{\perp}^2/u^2), \quad (2.28)$$

where $u = (2k_B T/m_{\text{Rb}})^{1/2}$ is the most probable velocity of Rb atoms at temperature T . Final step is to average the density matrix $\rho(B; \phi_v; \mathbf{r}_{\perp})$ over all azimuthal angles ϕ_v in the range $(0, 2\pi)$, i.e. over all equivalent trajectories. Due to the cylindrical symmetry of the atomic velocity distribution, the resulting density matrix will also be cylindrical symmetric. Thus, the angular integral appearing in the averaging over ϕ_v can be replaced by an angular integral over space

$$\rho(B; r) = \int_0^{2\pi} \frac{d\phi_v}{2\pi} \rho(B; \phi_v; \mathbf{r}_{\perp}) = \int_0^{2\pi} \frac{d\phi}{2\pi} \rho(B; \phi_v = 0; r \cos \phi, r \sin \phi), \quad (2.29)$$

where $\phi_v = 0$ is chosen only for convenience and does not influence the result.

The effects of the laser propagation along the cell and induced atomic polarization of the Rb vapor are included using the following approximations. The Rb vapor ensemble density matrix $\rho(B; r)$ and polarization \mathbf{P} are first computed assuming the constant value of the electric field \mathbf{E} along the z direction of laser propagation within the cell. The polarization of Rb vapor is obtained from the ensemble density matrix

$$\begin{aligned} \mathbf{P}(B; r) &= n(T) \text{Tr}(\rho(B; r) \hat{\mathbf{d}}) = n(T) e^{-i(\omega_0 t - \mathbf{k}\mathbf{r})} \times \\ &\times \sum_{j=-F_g}^{F_g} \sum_{k=-F_e}^{F_e} \tilde{\rho}_{e_k g_j}(B; r) \left(\frac{\mu_{g_j e_k, -1} - \mu_{g_j e_k, 1}}{\sqrt{2}} \mathbf{e}_x + i \frac{\mu_{g_j e_k, -1} + \mu_{g_j e_k, 1}}{\sqrt{2}} \mathbf{e}_y \right) + \text{c.c.}, \end{aligned} \quad (2.30)$$

where the ^{87}Rb concentration at temperature T is given by [42]

$$\log_{10} n(T) = \log_{10} \left(0.2783 \cdot \frac{133.322}{k_B T} \right) - 2.881 + 4.857 - \frac{4215}{T}. \quad (2.31)$$

Due to trace operation including dipole operator $\hat{\mathbf{d}}$, the polarization \mathbf{P} depends only on the optical coherences $\tilde{\rho}_{e_k g_j}$ between the excited and the ground Zeeman sublevels. Using the computed Rb polarization, the change of the electric field due to propagation of the laser through the Rb vapor is calculated. Let $\mathcal{E}(B; \mathbf{r})$ and $\mathcal{P}(B; \mathbf{r})$ denote complex slowly varying envelopes of the electric field and the polarization, respectively, defined by $\mathbf{E}(B; \mathbf{r}, t) = \text{Re}(\mathcal{E}(B; \mathbf{r}) e^{-i(\omega_0 t - \mathbf{k}\mathbf{r})})$ and $\mathbf{P}(B; \mathbf{r}, t) = \text{Re}(\mathcal{P}(B; \mathbf{r}) e^{-i(\omega_0 t - \mathbf{k}\mathbf{r})})$. Assuming that the change of electric field along the length L of the Rb cell is small enough, the exact relation for the slowly varying envelopes

$$\frac{\partial \mathcal{E}(B; r, z)}{\partial z} = \frac{i\omega_0}{2\epsilon_0 c} \mathcal{P}(B; r, z) \quad (2.32)$$

in the first approximation takes the form

$$\mathcal{E}(B; r, z = L) = \mathcal{E}(B; r, z = 0) + \frac{i\omega_0}{2\epsilon_0 c} \mathcal{P}(B; r) L, \quad (2.33)$$

where ϵ_0 is the vacuum dielectric constant. The laser electric field at the entrance to the Rb cell is $\mathcal{E}(B; r, z = 0)$, while the transmitted electric field is $\mathcal{E}(B; r, z = L)$.

In the experiments, the Hanle resonances are obtained by measuring the trans-

mitted power of the whole laser beam or of some small circular segment of the laser beam cross section. Local intensity of the laser beam is given by

$$I(\mathbf{r}) = \frac{c\epsilon_0}{2} |\mathbf{E}(\mathbf{r})|^2 = \frac{c\epsilon_0}{2} |\mathcal{E}(\mathbf{r})|^2. \quad (2.34)$$

Hence, the total transmitted power of the laser beam is

$$\mathbb{P}_{tot}(B) = \int_0^\infty I(B; r, z = L) 2\pi r dr = \pi c\epsilon_0 \int_0^\infty |\mathcal{E}(B; r, z = L)|^2 r dr. \quad (2.35)$$

The transmitted power in the case of detecting the light from the small circular segment of the laser beam cross section, centered at the distance ℓ from the beam axis and having the radius a , is

$$\mathbb{P}_{seg}(B) = \frac{c\epsilon_0}{2} \int_0^{2\pi} \int_0^a |\mathcal{E}(B; R(r, \phi), z = L)|^2 r dr d\phi, \quad (2.36)$$

where $R(r, \phi) = (\ell^2 - 2\ell r \cos \phi + r^2)^{1/2}$. The transmitted power of Eqs. (2.35) and (2.36) is used in the calculations of Hanle EIT and EIA resonances that are compared with the experiment.

The OBEs (2.20) represent a set of ordinary differential equations (ODEs). In order to solve these equations, a Fortran program is developed that uses BiM code [43]. BiM code implements a variable order-variable stepsize Blended Implicit Methods for (stiff) initial value problems for ODEs.

3. Influence of laser intensity and beam profile on Hanle resonances

All coherent phenomena strongly depend on the intensity of the applied laser field. Laser intensity dependence of EIT line-shapes has been studied extensively. It is shown that EIT line-widths at lower intensities have a linear dependence on the laser electric field, i.e. laser Rabi frequency, and a linear dependence on laser intensity at higher intensities [44, 45, 46]. The EIA line-widths, in contrast, have a maximum near the saturation limit [47]. Theoretical models usually assume a Λ atomic scheme, a steady state solution of the optical Bloch equations, and single values for the relaxation rates of the populations and coherences between the ground hyperfine levels. The relaxation rates for coherences are constants determined either by the diffusion rate (buffer gas cells) or by the reciprocal of the atom transit time through the laser beam (vacuum cells).

The term “laser intensity” is commonly used in the sense of an average beam intensity (laser power divided by the beam area), regardless of the laser beam profile used in the study. Since coherent phenomena are generally nonlinear, they depend strongly not only on the average beam intensity but also on the radial intensity distribution of the used laser beam. The typical laser beam profile used in experiments is Gaussian, while theoretical descriptions commonly assume a Π -shaped beam profile. The influence of different laser beam profiles has been studied only for EIT line-shapes in a few papers [26, 28, 27, 25, 29].

In the sequel, the presented theoretical model will be applied to the investigation of Hanle EIT and EIA resonances in ^{87}Rb vapor vacuum cell obtained using Gaussian and Π laser beam profiles. For the interaction of the Gaussian or Π laser beam with alkali-metal atom vapor, different effects such as Ramsey and Dicke narrowing, transit time, and Doppler broadening are examined either in vacuum [24, 48] or in buffer gas cells [49, 50, 51, 52]. The differences in EIT line shapes for Gaussian and Π laser beams were presented in [26, 27, 25] by considering only the entire laser

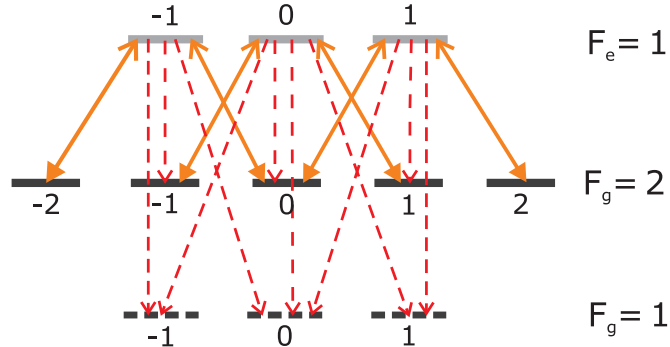


Figure 3.1: Zeeman sublevel scheme in ^{87}Rb at the D_1 line. The solid lines denote coupling with σ^+ and σ^- components of linearly polarized laser light. Dashed lines represent spontaneous emission.

beam contribution without focusing on the details of laser-atom interaction within the laser beam. However, different parts of the laser beam cross section, after passing through the alkali-metal vapor cell, carry different information about the atomic state and should yield different EIT and EIA resonances. The contribution of different segments of the Gaussian laser beam to the dark resonance line-shapes in a dense ^4He vapor was presented in Ref. [28] where deviation of overall resonance profile from pure Lorentzian shape is shown and attributed to observed spatial variation of line-shapes for different positions in the Gaussian laser beam. Therefore, it is important to take into account the real laser beam profile for proper modeling and analysis of coherent effects in alkali-metal vapors. Subsequent sections will present the details of the work published in [53, 54, 55].

3.1 Influence of the laser beam profile on the transient atomic evolution

This section illustrates that the transient evolution of the atoms passing through the laser beam is significantly affected by the beam intensity profile. Considered atomic transition is $F_g = 2 \rightarrow F_e = 1$ from D_1 line of ^{87}Rb . The transition is open because excited states can decay to another $F_g = 1$ ground state level. The energy level diagram given in Fig. 3.1 shows hyperfine levels either coupled by the linearly polarized laser light or populated due to spontaneous emission.

In what follows, the dependence of the laser intensity on the radial distance r

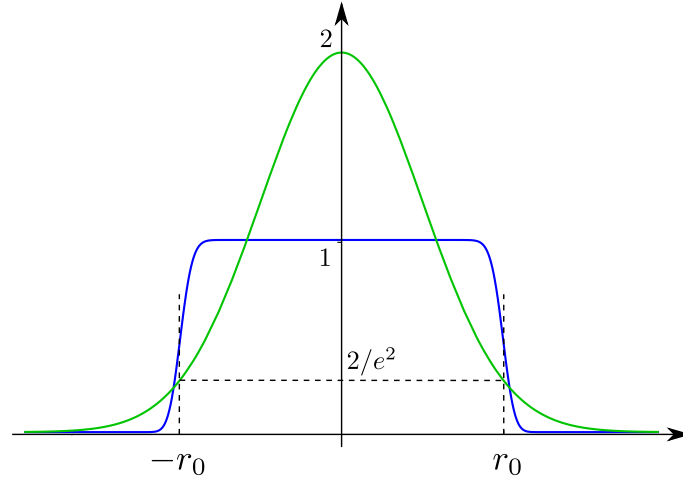


Figure 3.2: Π -shaped (blue curve) and Gaussian (green curve) intensity profiles of the laser beam of radius r_0 and unit average beam intensity.

from the beam axis for the Gaussian profile is

$$I(r) = 2\bar{I} \exp(-2r^2/r_0^2), \quad (3.1)$$

where r_0 is $1/e^2$ beam radius and \bar{I} is average beam intensity (total laser power divided by πr_0^2). A Π -shaped profile of the same intensity and radius was modeled using the equation

$$I(r) = \bar{I}a [1 + \operatorname{erf}(p(r - r_0))]^2, \quad (3.2)$$

where a is the normalization constant, p is a positive parameter affecting the steepness of the profile near $r = r_0$ and $\operatorname{erf}(\cdot)$ is the error function. The two beam profiles are illustrated in Fig. 3.2.

Figure 3.3 presents the spatial variation of the total population of the ground and the excited hyperfine states for the atom with specific values of the transverse v_\perp and of the longitudinal v_\parallel velocity components, for two laser intensities. These results were obtained for atoms traversing the laser beam along its diameter ($\phi = 0$), and for an axial magnetic field $B = 2 \mu\text{T}$. As the dashed lines indicate, the left sides are for the Π while the right sides are for the Gaussian transverse laser beam profile. It is evident that the atomic population of excited and ground states vary differently, both qualitatively and quantitatively, along the two laser beam profiles. After entering the laser beam, some fraction of the excited atoms decays into the uncoupled hyperfine

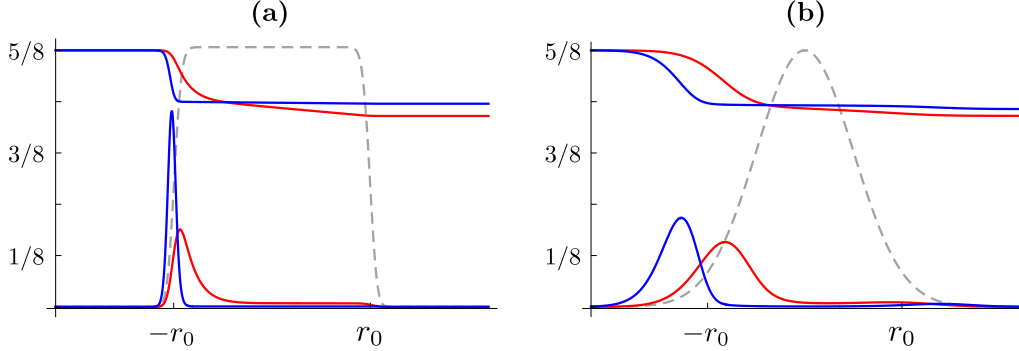


Figure 3.3: Calculated spatial dependence of the total Zeeman sublevel populations of the ground $F_g = 2$ (two upper curves in each figure) and the excited $F_e = 1$ (two lower curves in each figure) hyperfine levels for a single atom entering the laser beam from the left. (a) and (b) show the effects of the laser intensity for $\bar{I} = 0.5 \text{ mW/cm}^2$ (red lines) and $\bar{I} = 5 \text{ mW/cm}^2$ (blue lines). Results are for $v_\perp = 180 \text{ m/s}$, $v_\parallel = 0 \text{ m/s}$ and $B = 2 \text{ } \mu\text{T}$. Beam profiles are shown in dashed lines and have $r_0 = 1.5 \text{ mm}$. Excited level populations are multiplied by 20 in the case of a Π and by 40 in the case of a Gaussian profile.

level $F_g = 1$, resulting in loss of population from the transition $F_g = 2 \rightarrow F_e = 1$. The atoms decaying back to the $F_g = 2$ hyperfine level can populate two dark states composed of Zeeman ground state sublevels $|F_g = 2, m_g = m\rangle \equiv |2, m\rangle_g$. In the case of linearly polarized laser light these dark states are

$$|DS_1\rangle = \frac{1}{\sqrt{2}}|2, -1\rangle_g + \frac{1}{\sqrt{2}}|2, 1\rangle_g, \quad (3.3a)$$

$$|DS_2\rangle = \frac{1}{2\sqrt{2}}|2, -2\rangle_g + \frac{\sqrt{3}}{2}|2, 0\rangle_g + \frac{1}{2\sqrt{2}}|2, 2\rangle_g. \quad (3.3b)$$

During evolution in non-zero magnetic field B , the phase of each state $|2, m\rangle_g$ oscillates with frequency $\propto m \cdot B$, so that different Zeeman states will acquire different phases. This would alter relative phases between the states $|2, m\rangle_g$ in Eqns. (3.3) and deteriorate the dark states. Thus, the dark states are ideally non-coupled by the laser only when there is no magnetic field. However, when the magnetic field is sufficiently small and the laser intensity is high enough, a quasi-steady state can be reached, as can be seen in Fig. 3.3. In that case one part of the initial ground state population is pumped into an uncoupled hyperfine level $F_g = 1$ while the rest is in an almost non-coupled dark states. Because the rate of this population redistribution is higher for more intense laser light, the quasi-steady state is reached more rapidly

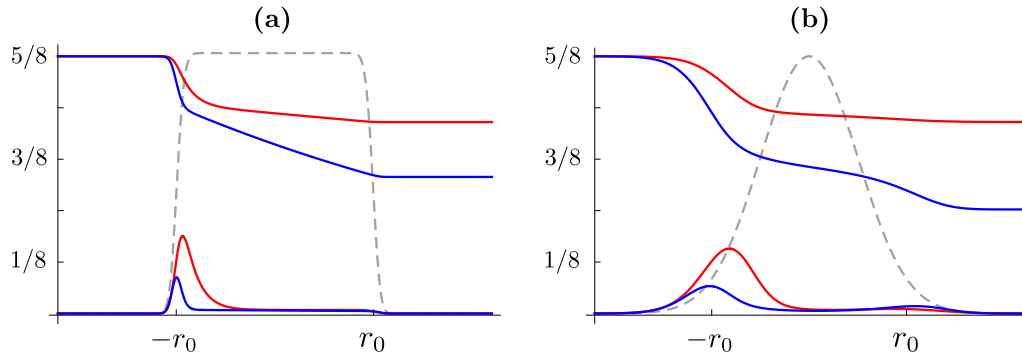


Figure 3.4: Calculated spatial dependence of the total Zeeman sublevel populations of the ground $F_g = 2$ (two upper curves in each figure) and the excited $F_e = 1$ (two lower curves in each figure) hyperfine levels for a single atom entering the laser beam from the left. (a) and (b) show the effects of the transverse velocity component for $v_{\perp} = 40$ m/s (blue lines) and $v_{\perp} = 180$ m/s (red lines). Results are for $v_{\parallel} = 0$ m/s, $B = 2 \mu\text{T}$, $\bar{I} = 0.5 \text{ mW/cm}^2$ and $r_0 = 1.5$ mm. Excited level populations are multiplied by 20 in the case of a Π and by 40 in the case of a Gaussian profile.

for larger laser intensities. At $B = 2 \mu\text{T}$ the Rb atoms can be excited from the dark states and the populations vary continuously while an atom is illuminated by the laser light. Changes in the populations as an atom enters the laser beam are much more rapid for Π -shaped beam profile as a consequence of steep intensity increase. In a Gaussian beam, atoms are at first slowly pumped out from the $F_g = 2$ level, resulting in the total excited population peak delay until the atom reaches higher light intensities of the Gaussian beam. Also, optical pumping is lower and the total excited population is higher for faster atoms, as shown in Fig. 3.4. The influence of longitudinal velocity component is presented in Fig. 3.5. Due to Doppler detuning, the atoms having nonzero longitudinal velocity interact with non-resonant laser light. Detuning from the exact resonance reduces the total excited state population and lowers the optical pumping. In a Gaussian beam, the total excited population peak is shifted toward more intense central parts of the Gaussian beam. It is apparent that the atomic transient evolution is influenced by the atomic motion all the time as the atom traverses the laser beam. Additional differences come from different velocities of the traversing atoms, i.e. from different time variation of the laser electric field as seen by the moving atom. Hence, in order to have a proper description of atomic interaction with the laser beam of some radial profile, it is mandatory to deal with time-dependent OBEs.

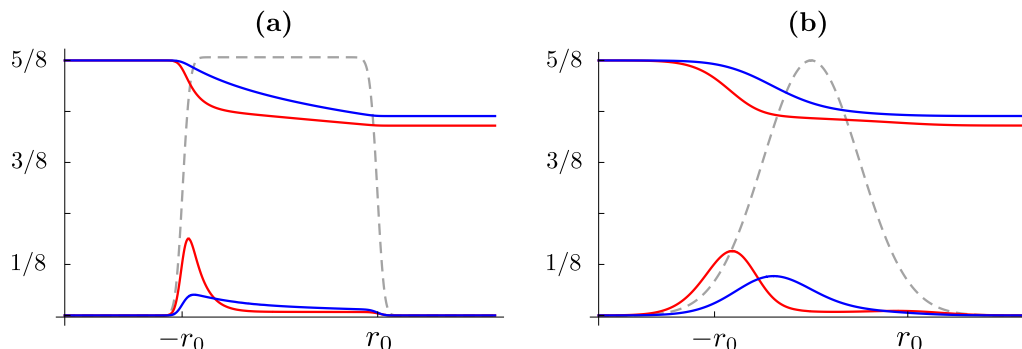


Figure 3.5: Calculated spatial dependence of the total Zeeman sublevel populations of the ground $F_g = 2$ (two upper curves in each figure) and the excited $F_e = 1$ (two lower curves in each figure) hyperfine levels for a single atom entering the laser beam from the left. (a) and (b) show the effects of the longitudinal velocity component for $v_{\parallel} = 0$ m/s (red lines) and $v_{\parallel} = 5$ m/s (blue lines). Results are for $v_{\perp} = 180$ m/s, $B = 2 \mu\text{T}$, $\bar{I} = 0.5 \text{ mW/cm}^2$ and $r_0 = 1.5 \text{ mm}$. Excited level populations are multiplied by 20 in the case of a Π and by 40 in the case of a Gaussian profile.

The following sections will present the theoretical results for Hanle EIT and EIA resonances for different laser beam profiles. Theoretical results will be compared with actual measurements done by the colleagues Aleksandar Krmpot, Senka Ćuk and Stanko Nikolić, members of the Photonics Center of the Institute of Physics, University of Belgrade.

3.2 Experimental setup

This section gives an outline of the experimental setup shown in Fig. 3.6. The external cavity diode laser is frequency locked to the appropriate transition of Rb. Laser locking is performed in an auxiliary vacuum Rb cell using the Doppler-free dichroic atomic vapor laser lock (DDAVLL) method [56, 57]. The variable neutral density filter is used for laser power adjustments. Single-mode fiber was used to provide the Gaussian laser beam. After passing through the Glan-Thompson polarizer, the laser beam becomes linearly polarized.

For experiments with the Gaussian profile, the laser beam is expanded to 3 mm in diameter. Laser beam diameters are determined from the $1/e^2$ value. The Π -shaped laser beam profile was obtained after expanding the Gaussian laser beam to 20 mm in diameter and then extracting its central part via the circular aperture placed on

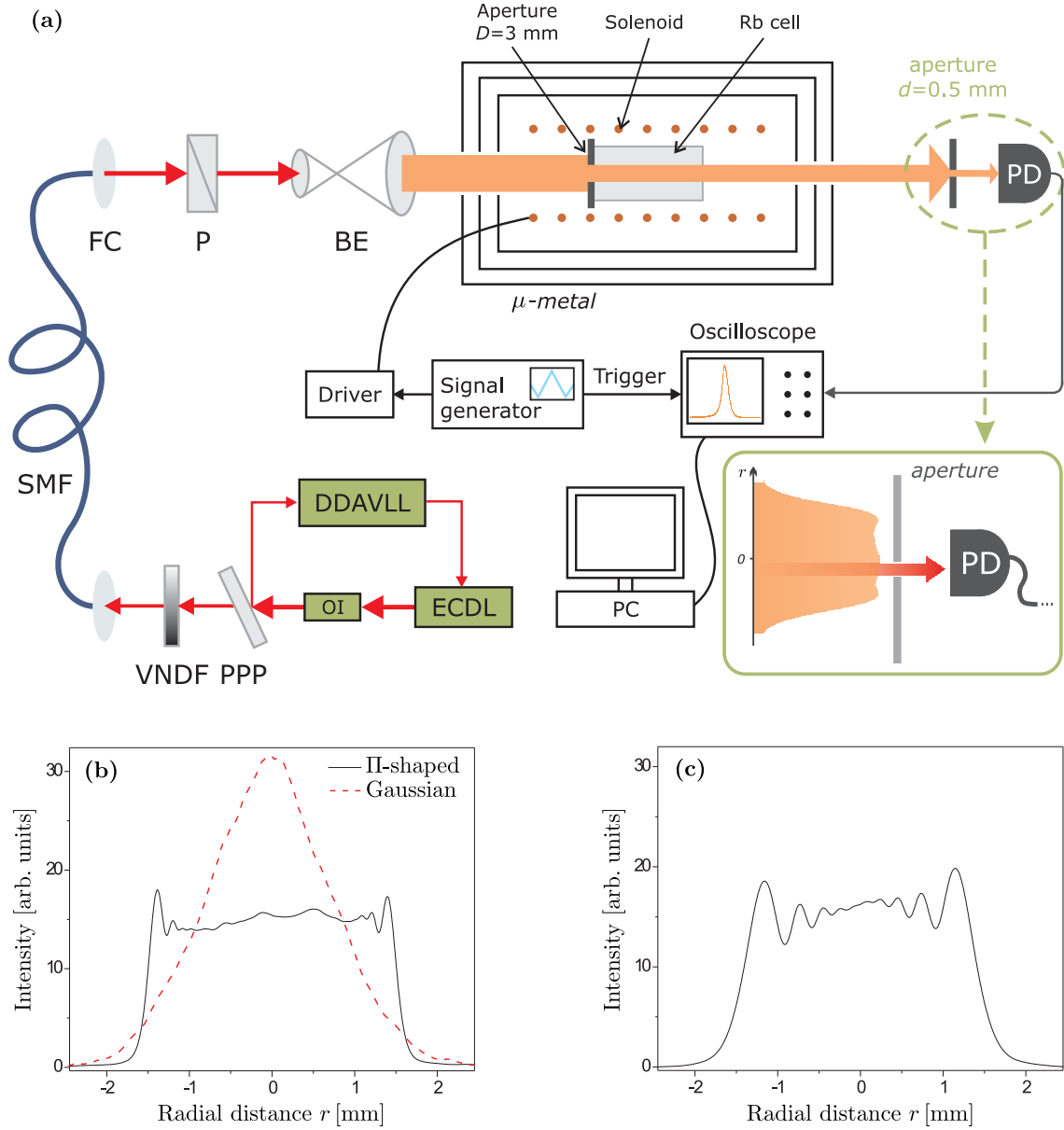


Figure 3.6: (a) Experimental setup: ECDL, external cavity diode laser; OI, optical isolator; DDAVLL, Doppler-free dichroic atomic vapor laser lock; VNDF, variable neutral density filter; SMF, single-mode fiber; FC, fiber collimator; P, polarizer; BE, beam expander; PD, photodiode. Moving the aperture on the translation stage allows only a selected part of the laser beam to reach the detector, while the rest of the laser beam is blocked. Π -shaped beam profiles were recorded by a beam profiler placed at 3 cm (b) and 30 cm (c) from the 3-mm circular aperture. (b) The dashed (red) curve is the profile of a Gaussian laser beam of the same power and diameter as the Π -shaped beam.

the entrance window of the cell. Diffraction affects the beam shape in the Rb cell and one has to settle for an approximation of the Π shape of the laser beam. After experimenting with different diameters of the expanded Gaussian laser beam, sizes of apertures, and thicknesses of the foil used for the apertures, Π -shaped laser beam whose radial intensity profiles presented in Figs. 3.6(b) and 3.6(c) is obtained. The beam profiles measured by the beam profiler are 3 and 30 cm away from the 3-mm aperture on 0.1-mm thick foil. The first profile is at a distance equal to the distance between the aperture and the mid section of the Rb cell. This profile is referred to as Π -shaped throughout the thesis. The beam profile at 30 cm from the aperture is used to show relatively small changes in the profile with distance and to justify use of the Π -shaped profile in the theoretical model. Together with the Π -shaped laser beam profile, the profile of the Gaussian laser beam is also presented in Fig. 3.6(b). The two beam profiles shown together have the same power and the same diameter. The laser beam passes through the 6-cm-long vacuum Rb cell containing a natural abundance of rubidium isotopes. The cell is placed in the solenoid used for scanning the axial magnetic field. The cell and the solenoid are placed inside triple-layered μ -metal cylinders to eliminate Earth's and stray magnetic fields. In the parts of the experiment studying the effects of the laser beam profile on the intensity dependence of whole-laser-beam EIT (EIA), the entire transmitted laser beam was detected while scanning the external magnetic field. To measure Hanle EIT (EIA) from only small parts of the laser beam, a movable aperture 0.5 mm in diameter is placed in front of the large detection surface photodiode (area of 80 mm²). By moving the aperture with the fine translation stage only light from a small segment of transmitted laser beam is allowed to reach the photodiode. The signal obtained from the photodiode while scanning the external magnetic field is recorded by the digital oscilloscope and transferred to the computer.

3.3 Hanle EIT resonances from selected segments of the Gaussian laser beam cross section

Typical transverse laser beam profile in experiments studying EIT is Gaussian. The intensities in the central parts and in the wings of the Gaussian laser beam are very different. Nevertheless, the order of magnitude lower intensity in the wings can still significantly affect the atomic coherent evolution. The lifetime of alkali-metal atomic coherence in vacuum cell is longer than the atom transit time through the laser beam. Thus, the light in the wings can “probe” the induced coherence of the atoms coming from central parts of the Gaussian laser beam leading to Ramsey-like interference. The reversed order of events, interaction of atoms with the light first in the beam wings and afterward in the intense central parts of the laser beam, will not reveal such effect of the coherently prepared atomic state due to overwhelming influence of the intense light at the center of the Gaussian beam. Therefore, different Hanle EIT resonances should be obtained from different parts of the Gaussian laser beam. This section refers to the first confirmation that Ramsey-like repeated excitation of atoms *within the same laser beam* significantly affects the resonance line-shapes observed from the segments of the Gaussian laser beam cross section [53].

The contribution of different segments of the Gaussian laser beam to the EIT resonance line-shapes in a dense ^4He vapor was presented in [28]. The results of Ref. [28] show deviation of overall resonance profile from pure Lorentzian shape attributed to observed spatial variation of line-shapes for different positions in the Gaussian laser beam. However, no Ramsey-like repeated excitation of atoms was found. This will be discussed later. There are several papers showing significance of the repeated interaction of atoms by separated, in space and/or time, laser beams tuned to Raman resonance of the atomic transitions. Narrowing of EIT resonances in cells with anti-relaxation coatings [23] and in buffer gas cells [49, 50] is attributed to repeated excitation by the laser beam after the atoms spend some time in the “dark” part of the cell, not illuminated by the laser light.

This section presents the study of EIT resonances originating from different parts of the Gaussian laser beam cross section, after the whole laser beam passes through the Rb vapor cell. The investigation was performed on ^{87}Rb atoms at D_1 line transition $F_g = 2 \rightarrow F_e = 1$ in the Hanle configuration. Hanle resonance line-shapes were calculated using the model introduced in the section 2.3, i.e. by including the effects of the atomic polarization, the time evolution and the interaction of the

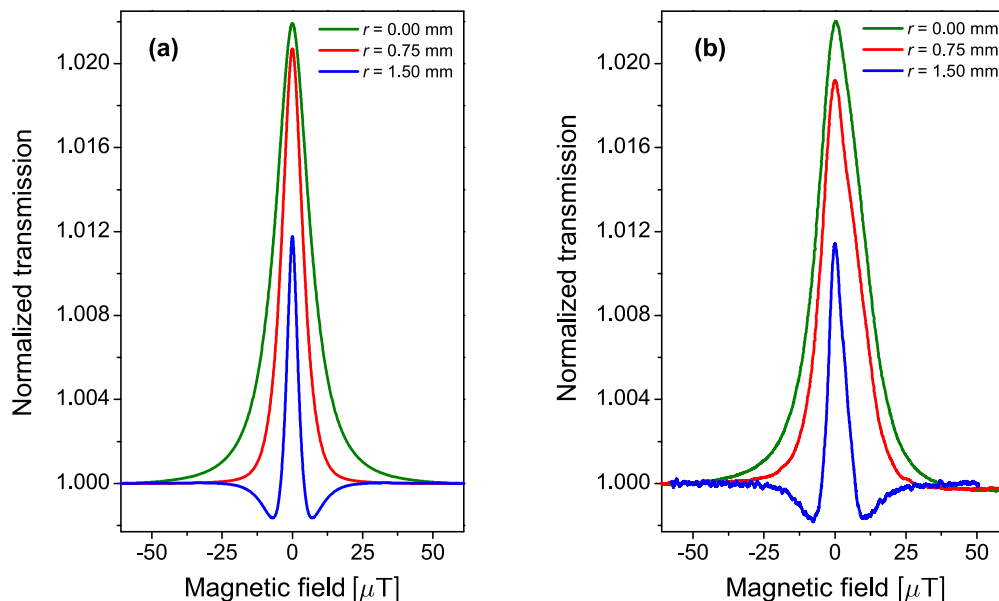


Figure 3.7: Theoretical (a) and experimental (b) Hanle EIT resonances obtained from the small parts of the Gaussian beam. The green, the red and the blue curves are for $r = 0$ mm, 0.75 mm and 1.5 mm, respectively, where r is the radial distance of the aperture from the beam center. The beam diameter is 3 mm and the total intensity is 0.5 mW/cm^2 . Theoretical results were normalized to the experimental results such that peak values at $r = 0$ mm are equal.

atomic state with light in the Gaussian laser beam. The theoretical description distinguish the contribution to the EIT resonances from the atoms coming to the wings from central parts of the laser beam and from the outside of the beam.

The curves in Fig. 3.7 represent theoretical and experimental resonances obtained for different positions of the aperture along the beam diameter, with $r = 0$ mm referring to the laser beam center. The laser intensity is 0.5 mW/cm^2 . There is a good agreement between the theory and the experiment. Figure 3.7 reveals significant differences in line-shapes, widths and amplitudes of the resonances at different positions within the beam. The Hanle EIT resonances from the wings of the beam show the two transmission minima at certain values of the magnetic field. The origin of such line-shape is in the interaction of light in the wings of the laser beam with the coherently prepared atoms coming from the central part of the Gaussian beam. Namely, during the interaction with the strong laser electric field near the center of the Gaussian beam an atom is coherently prepared into the dark state. The dark state is coherent superposition of Zeeman sublevels of $F_g = 2$

ground level and is ideally non-coupled to the laser light only in the absence of external magnetic field. Zeeman sublevel populations and coherences are subjected to various relaxation processes. The transit time of the atoms through the laser beam is much shorter than the relaxation times of the ground state coherences. During the time that atom spends in the laser beam the coherences vary due to competitive effects of the laser excitation and the external magnetic field. The laser continuously forces the atomic coherence to be in-phase with the electric field. The external magnetic field \mathbf{B} causes oscillations of the coherence phase at Larmor frequency that is proportional to B . Such oscillations can turn the dark atomic state into the bright state and vice versa. When atoms move away from the central to the outer parts of the beam (outgoing atoms), the oscillatory behavior prevails when the laser field is low enough. Thenceforth the phase of the atomic coherence oscillates and the atoms are cycling between dark and bright states. The outer section of the Gaussian beam, where this cycling occurs, is *the interference region*. Aside from outgoing atoms there are also atoms coming into the interference region from the outside of the beam (incoming atoms). Note that the incoming atoms are not coherently prepared and do not contribute to the interference. Consider an outgoing atom from the certain velocity class traversing the interference region along the certain trajectory. While passing through the laser beam the atom experiences nearly constant magnetic field due to its slow variation in the experiment. The phase shift of the atomic coherence at the point r along this trajectory depends on the value of the magnetic field B . If the coherence at r is in-phase with the laser electric field, the atom is in the dark state and the transparency at r is increased. It is clear that $B = 0$ fulfills this condition since the atom is continuously in the dark state regardless of the location in the interference region. If the magnetic field is such that the difference between the phases of the atomic coherence and the laser field equals to $\pi/2 + n\pi$ ($n \in \mathbb{Z}$) the atom is in the bright state, and the minima of transparency at r occur. These minima and maxima of the transparency are interference fringes. The atoms inside the cell move with different velocities and traverse different trajectories with respect to the laser beam. The averaging over the velocity and trajectory distributions results in the lowering of the amplitude and in washing out the higher-than-first order interference fringes in the transmission signal.

Previous considerations are supported by the results given in Fig. 3.8. The results are shown the magnetic field $B = 10 \mu\text{T}$ at which transmission minima appear in

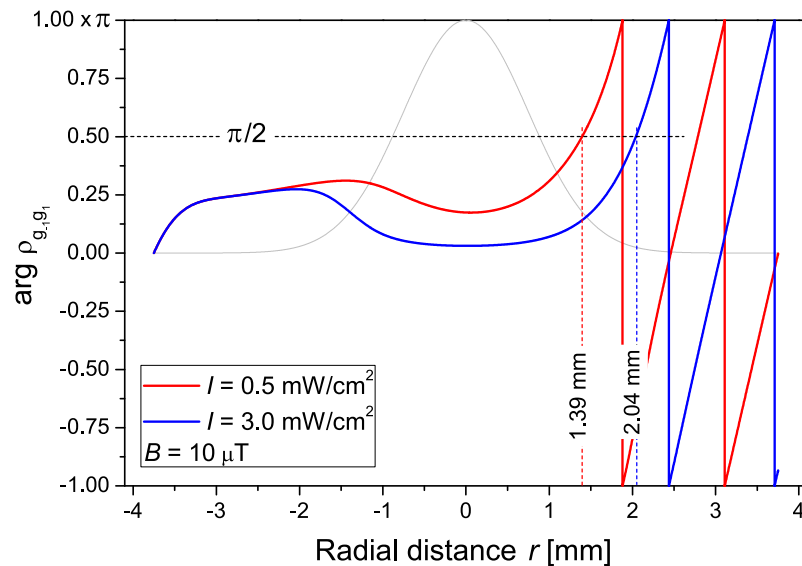


Figure 3.8: Change of the argument of atomic coherence ρ_{g_{-1}, g_1} during atomic passage through the 3-mm-wide Gaussian laser beam at constant magnetic field. The dashed lines denote the positions along the beam radius where the Hanle EIT resonances for the given laser intensities exhibit very pronounced transmission minima. The transmission minima at the Hanle EIT resonances appear in the wings of the Gaussian beam cross section when $\arg \rho_{g_{-1}, g_1}$, i.e., the atomic phase is equal to $\pi/2$. The magnetic field value $10 \mu\text{T}$ is chosen because the transmission minima in the Hanle EIT resonances appear exactly at this value. The beam profile is presented by the gray line.

Hanle EIT resonances. Since the laser electric field tends to keep the phase of the coherence constant while the magnetic field tends to change the phase, when both magnetic and electric field are present, the phase of atomic coherence depends on the magnitudes of these two fields. The atom is coherently prepared and the phase is kept fixed by the laser field in the central parts of the Gaussian beam. In the wings of the Gaussian beam the phase value of the same atomic coherence depends on the local laser intensity. When the atomic phase reaches $\pi/2$, i.e., the atomic state becomes bright, two transmission minima appear in Hanle EIT resonances obtained in the wings of the Gaussian laser beam. Naturally, the distance from the beam center where that happens increases with the laser intensity, as can be seen from the curves in Fig. 3.8.

Figure 3.9 shows Hanle EIT resonances calculated by considering outgoing, incoming and both groups of atoms. The results are given for two distances from the

3.3 HANLE EIT RESONANCES FROM SELECTED SEGMENTS OF THE GAUSSIAN LASER BEAM CROSS SECTION

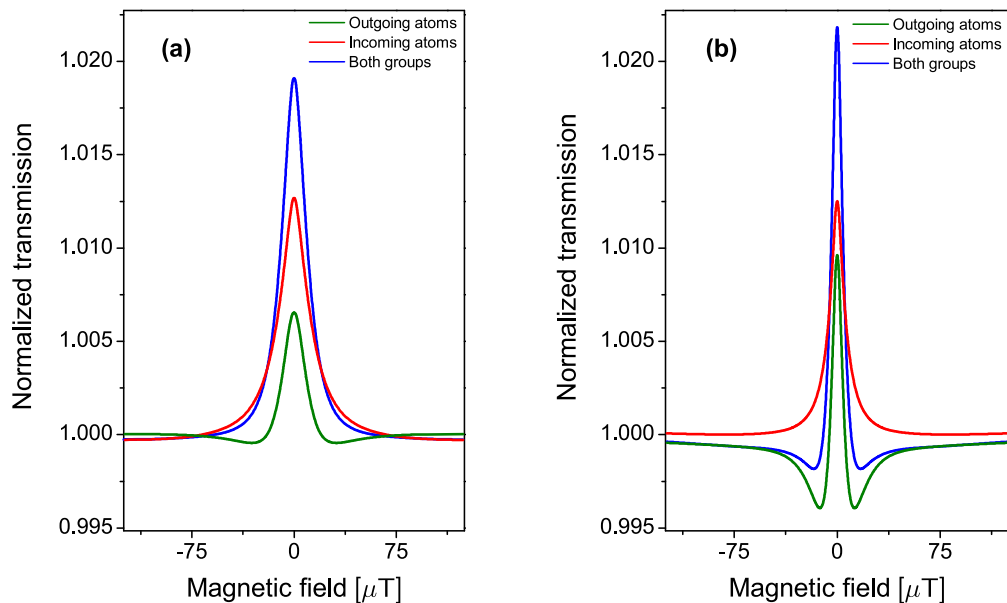


Figure 3.9: Calculated contribution of outgoing (green), incoming (red) and both outgoing and incoming (blue) atoms to the Hanle EIT resonances for two distances from the laser beam center: $r = 1.00$ mm (a) and $r = 1.75$ mm (b). The laser intensity is 3 mW/cm^2 .

laser beam center, $r = 1$ mm (Fig. 3.9(a)) and $r = 1.75$ mm (Fig. 3.9(b)). It is evident that only outgoing atoms are responsible for the appearance of the two sideband transmission minima. Effect of outgoing atoms on the resonance line-shape, at certain distance r , depends on the laser intensity. Results in Fig. 3.9 show that for 3 mW/cm^2 , the contribution of outgoing atoms to Hanle EIT resonances is negligible at the distance $r = 1$ mm, while it is very strong at $r = 1.75$ mm. The physical mechanism used in the above explanation of these results is the same as in Ramsey interference. The resulting Hanle line-shapes are similar to those obtained due to Ramsey interference in separated pump and probe laser fields in vacuum gas cells [58]. In this case, the extended low intensity wings of the Gaussian laser beam play the role of the probe laser beam.

Figure 3.10 shows theoretical (a) and experimental (b) behavior of the Hanle EIT line-widths as a function of the aperture radial position r . There are two reasons for narrowing of the Hanle EIT resonances in the wings of the Gaussian laser beam profile. The first is the lower power broadening in the outer parts of the laser beam. Another reason is the Ramsey-like narrowing caused by the aforementioned physical

3.3 HANLE EIT RESONANCES FROM SELECTED SEGMENTS OF THE GAUSSIAN LASER BEAM CROSS SECTION

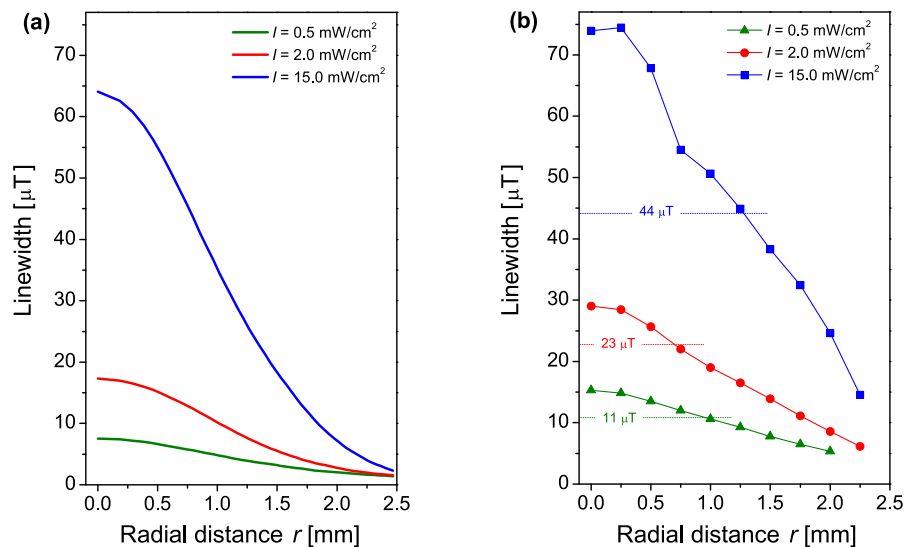


Figure 3.10: Theoretical (a) and experimental (b) Hanle EIT line-widths for the different positions r of the aperture along the laser beam diameter. The blue, the red, and the green curves are for the intensities $I = 15 \text{ mW/cm}^2$, 2 mW/cm^2 , and 0.5 mW/cm^2 , respectively. The dashed bars in (a) represent the Hanle EIT line-widths obtained by detecting the entire laser beam.

processes. The line narrowing at larger radial distances becomes more prominent as the total laser intensity increases. The dashed bars in (a) denote the line-widths of the Hanle EIT resonances for the three laser beam intensities when the whole laser beam is detected. At this point we find suitable to compare with results of Ref. [28]. Line-shape Rabi power broadening corresponding to local intensities within the Gaussian beam, was also observed in [28], but without altering local resonance Lorentzian shape due to interference effects. One possible reason for the absence of the interference effects in such experiment is in the used experimental conditions. Namely, the mean free path of ^4He atoms at the pressure of 1.5 Torr is of the order 0.1 mm, while used laser beam diameter is 6 mm. Motion of ^4He atoms is diffusive so that they are effectively localized and cannot freely traverse the laser beam as in our case. Therefore, the interference effects could not occur in the experiment performed in Ref. [28] due to frequent atom-atom collisions.

3.4 Hanle EIT resonances from selected segments of the Π -shaped laser beam cross section

This section contains the study of time and space evolution of atomic states as the Rb atoms traverse the Π -shaped laser beam, i.e., laser electric field of nearly constant intensity. Such studies were performed by obtaining EIT line shapes from different circular segments of the laser beam cross section, much smaller than the laser beam diameter, after the entire beam had already passed through the Rb cell. Hanle configuration with the laser locked to the $F_g = 2 \rightarrow F_e = 1$ hyperfine transition of the D_1 line in the ^{87}Rb isotope in the vacuum vapor cell is used. This is similar to the examinations presented in the previous section. Due to interaction with a laser electric field having different distributions in the Gaussian and Π -shaped beams, the atomic state develops differently in the presence of a small external magnetic field. Narrowing of the Hanle EIT in the wings of the Gaussian laser beam was attributed to the interference of the laser light and coherently prepared atoms coming from the central part of the beam. The narrowing is accompanied by the appearance of Ramsey-like transmission minima in Hanle EIT line shapes detected in the Gaussian beam wings. Therefore, it is expected that examination of EIT line shapes obtained in different segments of Π laser beam cross section should reveal some details about the transient evolution of interacting atoms. It can also help in understanding differences in line-widths and amplitudes of EIT resonances obtained using two laser beam profiles and reported in Refs. [25, 26, 27]. Partial Hanle EIT resonances from different segments of the Π laser beam were not thoroughly investigated. The significance of using the Π profile is in the elimination of the effects due to transverse variation of the laser intensity, providing conditions for more direct insight into the laser-atom interaction. Theoretical calculations of the spatial dependence of EIT line shapes along the laser beam profile are compared with the experimental results. The calculations are based on time-dependent optical Bloch equations model presented in the section 2.3. It unveils the influence of the optical pumping into the uncoupled ground-state hyperfine level on the obtained Hanle EIT resonance line-shapes.

The actual beam profile used in the experiment is shown in Fig. 3.11. The beam profiles obtained at 30 cm from the aperture are given to show relatively small changes in the profile with distance and to justify use of the Π -shaped profile in the calculations. Theoretical and experimental Hanle EIT resonances obtained at

3.4 HANLE EIT RESONANCES FROM SELECTED SEGMENTS OF THE Π -SHAPED LASER BEAM CROSS SECTION

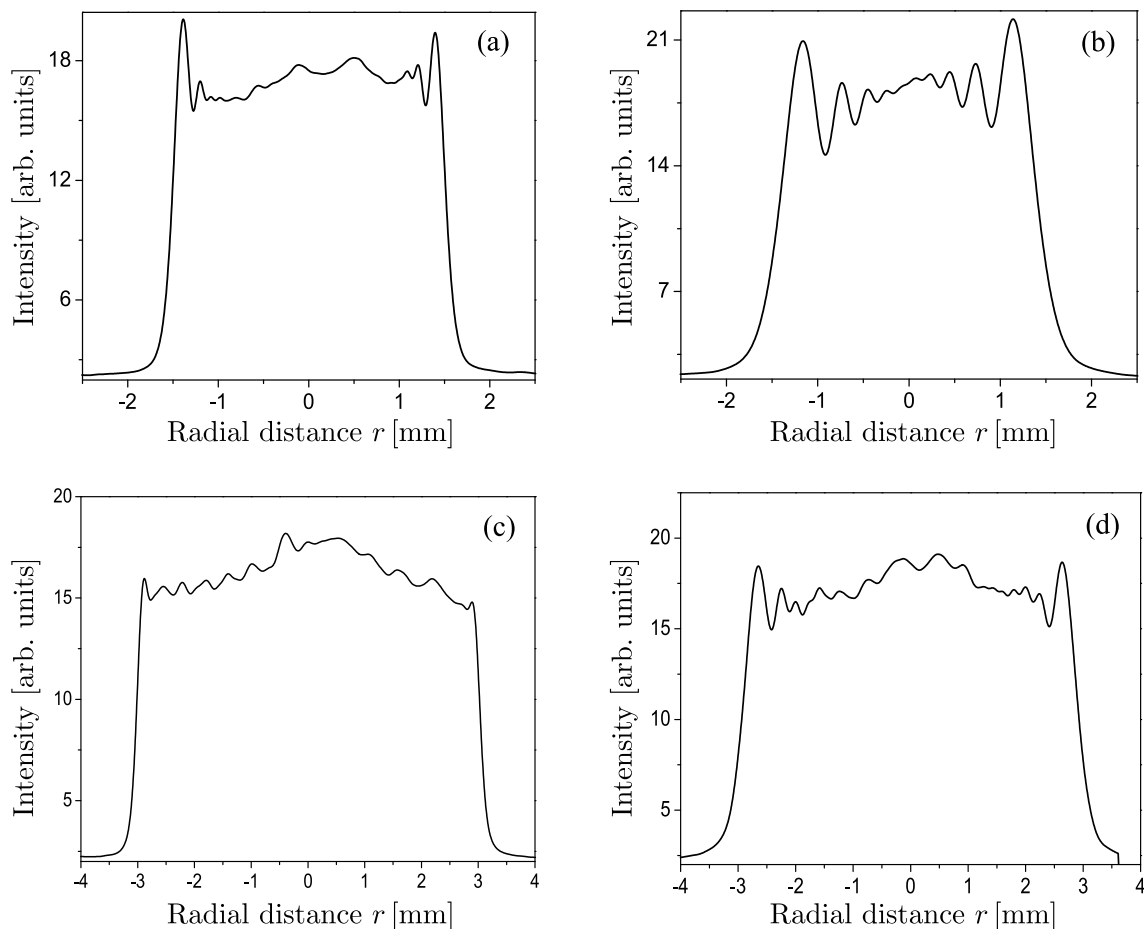


Figure 3.11: Two Π -shaped beam profiles recorded by a beam profiler placed at different distances from the circular aperture: at 3 cm (a) and 30 cm (b) for the 3-mm profile, and at 3 cm (c) and 30 cm (d) for the 6-mm profile.

different positions of the small aperture along the beam diameter are presented in Figs. 3.12(a) and 3.12(b), respectively. Hereafter $r = 0$ mm refers to the center of the laser beam cross section. The beam diameter is 3 mm and overall intensity is 4 mW/cm^2 . Results in Fig. 3.12 show significant differences in shapes, widths, and amplitudes of resonances obtained at different positions within the cross section of the Π -profiled laser beam. The Hanle EIT resonances originating from the central parts of the Π beam cross section exhibit two transmission minima next to the central maximum of the EIT resonance. Additionally, resonances in the center of the laser beam cross section are narrower than those originating from the outer parts of the beam. These results are reversed to the results obtained from different

3.4 HANLE EIT RESONANCES FROM SELECTED SEGMENTS OF THE Π -SHAPED LASER BEAM CROSS SECTION

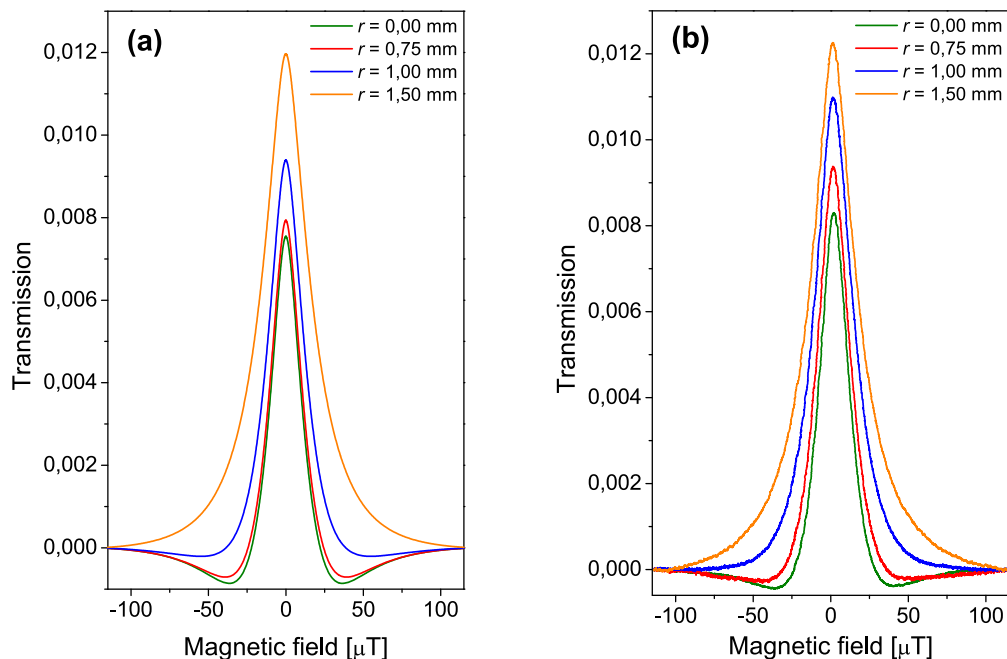


Figure 3.12: Theoretical (a) and experimental (b) Hanle EIT resonances obtained from the small segments of the Π laser beam cross section. Green, red, blue, and orange curves are for $r = 0$ mm, 0.75 mm, 1.0 mm and 1.5 mm, from bottom to top, respectively, where r is the radial distance of the small aperture from the beam center. The beam diameter is 3 mm and the total intensity is 4 mW/cm². The theoretical results were normalized to the experimental results at $r = 0$ mm.

segments of a Gaussian laser beam cross section presented in the previous section. In the latter case two minima appear, and the resonances are narrower, when the small aperture is placed at the wings of the Gaussian beam cross section.

Neglecting small intensity variations of the Π -shaped laser beam (see Fig. 3.11) atoms interact with a constant electric field of the laser in the presence of constant external magnetic field during the passage through the laser beam. The evolution of the atomic state under these conditions is different than in the case of the Gaussian beam. In Fig. 3.13 we present a calculated variation of the total population of the excited state $F_e = 1$ as a function of distance from the entrance in the laser beam (leftmost), considering atoms with the most probable radial velocity of 180 m/s at room temperature (300 K). When an atom enters the laser beam at zero magnetic field ($B = 0$), it starts to absorb photons and the population of the excited state, i.e., the sum of the populations of all excited-state Zeeman sublevels, increases (red thick line in Fig. 3.13). Shortly after entering the laser beam, atoms are prepared into

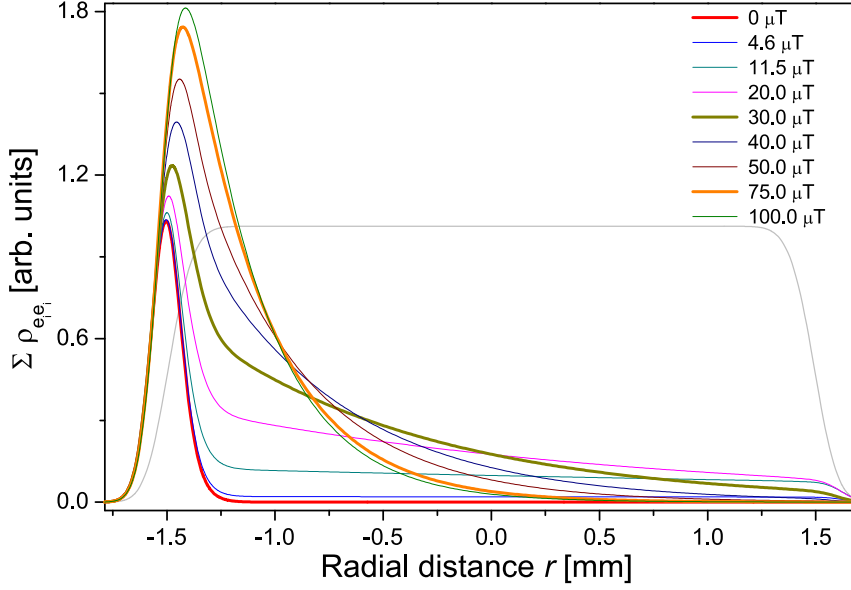


Figure 3.13: Calculated total population $\sum \rho_{e_i, e_i}$ of all Zeeman sublevels of the $F_e = 1$ excited level at different magnetic fields as a function of position along the 3-mm beam diameter of the Π -shaped laser beam. The curves corresponding to the magnetic fields 0 – 100 μT from the legend appear from bottom to top, respectively, at $r = -1.25$ mm. The beam intensity is 4 mW/cm^2 . The atomic velocity is 180 m/s . The thin gray line represents the cross section of the laser beam with an arbitrary intensity unit. The atom enters the beam from the left.

the dark state and do not absorb photons afterward yielding maximal transmission. At small magnetic fields the preparation of atoms into the dark state is less efficient and there is certain probability for photon absorption during the entire interaction of the atom and the laser light. Thus, the excited-state population decreases less rapidly than for $B = 0$ as atoms move through the laser beam and transmission decreases. As Fig. 3.13 shows, the atomic total excited-state population, for atoms near the laser beam center, is largest for a magnetic field at about 30 μT (dark yellow thick line) when transmission reaches minimum. At larger magnetic fields (e.g., 75 μT , orange thick line), pumping into the uncoupled $F_g = 1$ hyperfine level becomes considerable and transmission noticeably increases. The observed behavior of the excited-state populations and resulting laser transmission are due to the fact that the rates of pumping into the dark state and into the uncoupled level depend oppositely on the external magnetic field. Therefore, the appearance of two transmission minima at about 30 μT is a joint effect of preparation of atoms into the dark state and optical pumping into the uncoupled ground hyperfine level.

3.4 HANLE EIT RESONANCES FROM SELECTED SEGMENTS OF THE II-SHAPED LASER BEAM CROSS SECTION

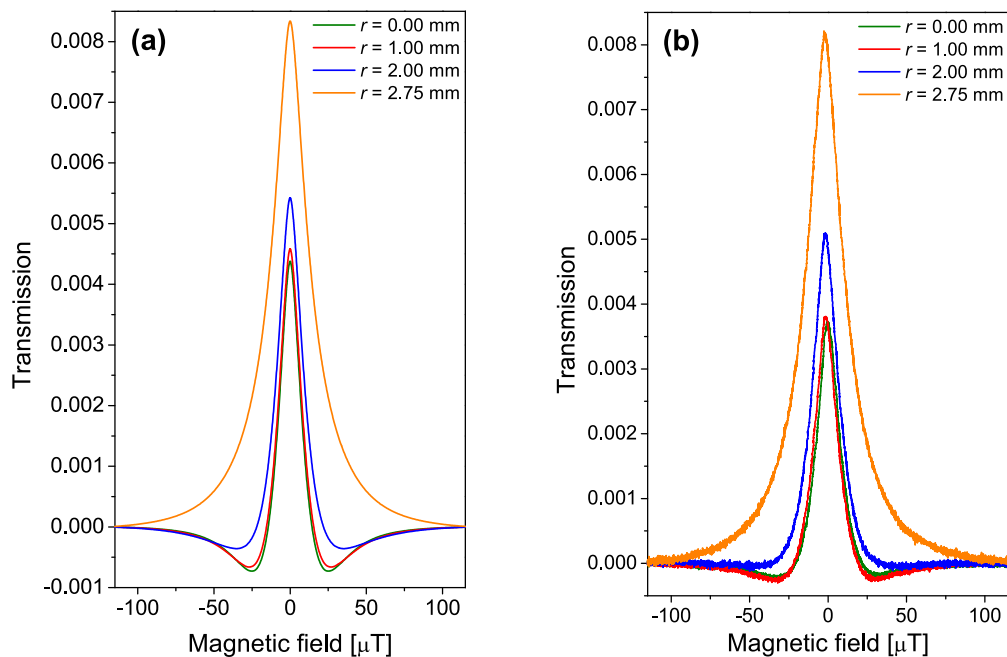


Figure 3.14: Theoretical (a) and experimental (b) Hanle EIT resonances obtained from the small segments of the II laser beam cross section at four distances from the beam center: 0, 1.0, 2.0, and 2.75 mm (from bottom to top, respectively). The beam diameter is 6 mm and the total laser intensity is 4 mW/cm^2 . The theoretical results were normalized to the experimental results at $r = 0$ mm. Note that the curves for $r = 0$ and $r = 1.0$ mm almost overlap.

Behavior of the excited-level population at different magnetic fields explains the origin of the two symmetrically placed, with respect to the central transmission peak, transmission minima present in the Hanle EIT resonances recorded near the center of the laser beam. For a given laser intensity, atoms have to spend a certain time in the laser beam before these minima emerge in the Hanle EIT curves. It turns out that if the laser beam has a 3 mm diameter, for most atoms this shape of the EIT would only be observed in the laser beam center. If one considers a laser beam with a diameter larger than 3 mm, under the same experimental conditions (the same cell temperature, i.e., the most probable velocity, and the same laser intensity), it is expected that optical pumping would significantly affect EIT line shapes at the same distances of ~ 1.5 mm from the edge of the beam. Consequently, with the larger beam diameter, transmission minima should occur in the wider domain around the beam center. The curves in Fig. 3.14 present theoretical and experimental Hanle EIT resonances obtained at different positions of the small aperture along the 6-mm

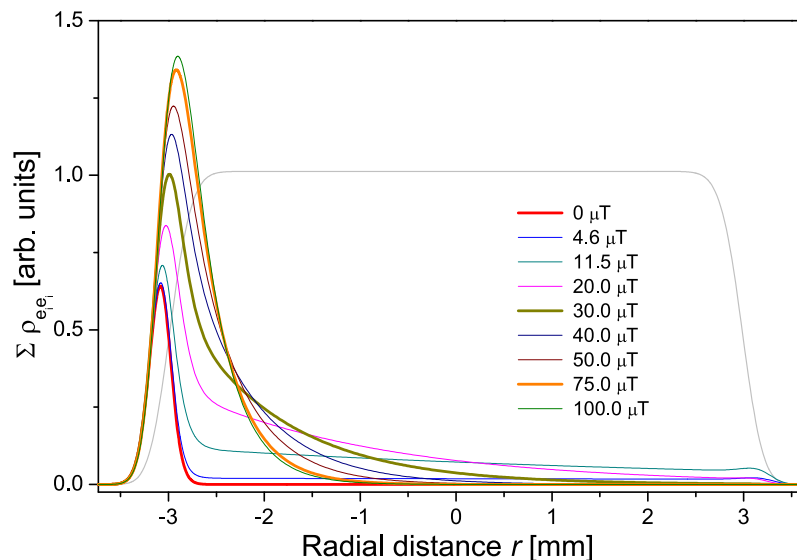


Figure 3.15: Calculated total population $\sum \rho_{e_i, e_i}$ of all Zeeman sublevels of the $F_e = 1$ excited level at different magnetic fields as a function of position along the 6-mm beam diameter of the Π -shaped laser beam. The curves corresponding to the magnetic fields 0 – 100 μT from the legend appear from bottom to top, respectively, at $r = -2.75$ mm. The beam intensity is 4 mW/cm^2 . The atomic velocity is the most probable velocity at room temperature (180 m/s). The thin gray line represents the laser beam cross section profile. The atom enters the beam from the left.

diameter Π -shaped laser beam. Overall intensity is similar as before, 4 mW/cm^2 . Now, transmission minima are present in Hanle EIT resonances obtained not only in the center of the laser beam, but also up to a certain distance away from the center. Moreover, the resonances obtained up to that distance are almost the same, as in the case of overlapping resonances for $r = 0$ and $r = 1$ mm in Fig. 3.14.

The explanation for the appearance of transmission minima in Hanle EIT line shapes in the case of a 6-mm-diameter laser beam could be made tracing the behavior of the total excited state populations given in Fig. 3.15 and applying the same logic as in Fig. 3.13, i.e., for the 3-mm beam diameter. It is apparent from Figs. 3.13 and 3.15 that under the same experimental conditions, the distance from the beam edge where the total excited-state population at $B = 75 \mu\text{T}$ (orange thick line) falls down to zero is the same in both cases, approximately 1.5 mm. For the 3-mm beam diameter this point coincides with the location of the beam center, while for the 6-mm-diameter beam this location is, of course, away from the beam center. Therefore, for the 6-mm-diameter beam, transmission minima in Hanle EIT

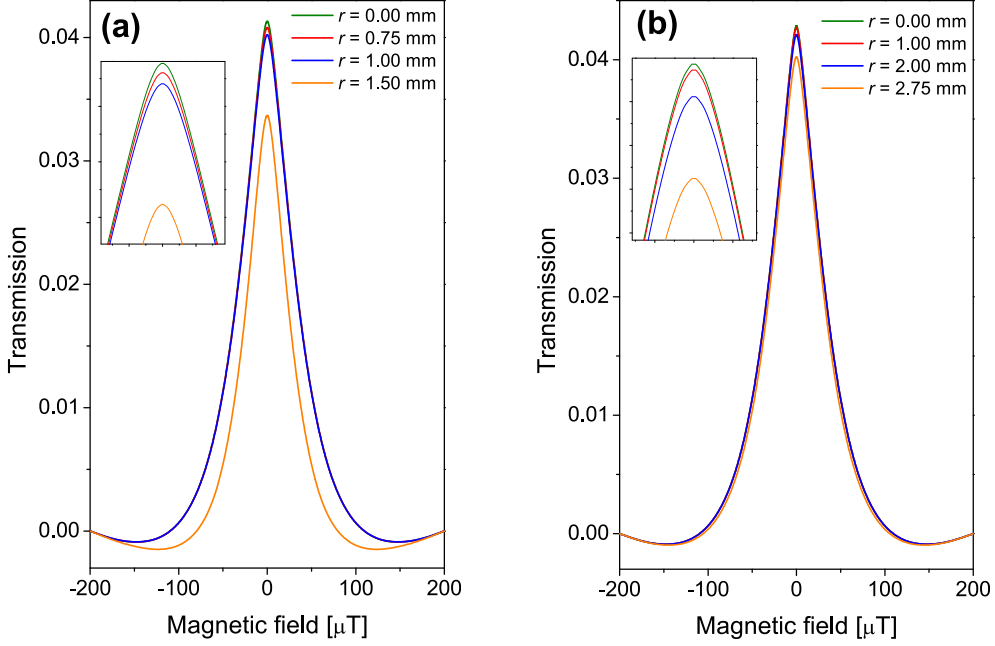


Figure 3.16: Calculated Hanle EIT resonances obtained from the small segments of the Π laser beam cross section of (a) 3 mm and (b) 6 mm diameter. It is taken that the transition $F_g = 2 \rightarrow F_e = 1$ is closed. The resonances almost completely overlap and can be barely distinguished only near $B = 0$ (see insets). The curves corresponding to decreasing radial distances from the legends appear from bottom to top, respectively. The laser intensity is $4 \text{ mW}/\text{cm}^2$. Note a different scale for the magnetic field than in Figs. 3.12 and 3.14 and broader resonances than in the case of the open transition.

resonances at around $B = 30 \mu\text{T}$ will occur as long as EIT resonances are taken from the central region of 3 mm in diameter.

To further clarify the influence of optical pumping on Hanle EIT line shapes the calculations for artificially closed transition $F_g = 2 \rightarrow F_e = 1$ were performed, i.e., the optical pumping was eliminated. Calculated Hanle EIT resonances, for the laser intensity of $4 \text{ mW}/\text{cm}^2$, are shown in Fig. 3.16. Obtained Hanle EIT line shapes are broader than for the open system because there is no population-loss-induced narrowing [59, 60]. The absence of population loss also yields the same line shapes regardless of the distance from the beam center. There are no transmission minima in line shapes obtained at the central regions of the beam cross section. In this case, a slight increase of transmission at very large magnetic fields ($\sim 200 \mu\text{T}$) is due to the broad single-photon Hanle background on which the EIT resonances are superimposed. Next, we investigate the influence of the

3.4 HANLE EIT RESONANCES FROM SELECTED SEGMENTS OF THE Π -SHAPED LASER BEAM CROSS SECTION

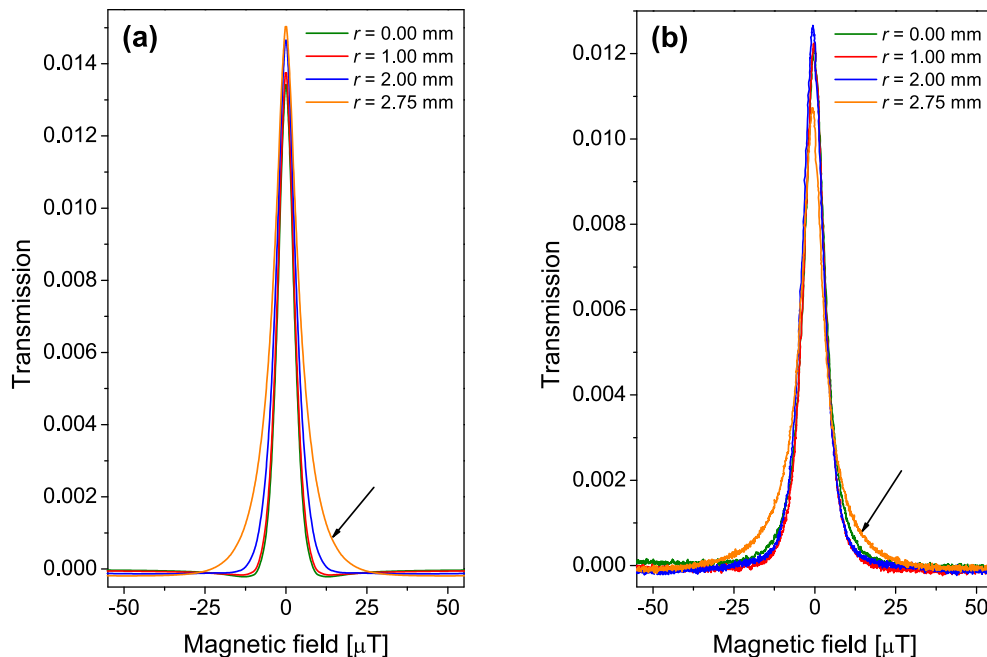


Figure 3.17: Theoretical (a) and experimental (b) Hanle EIT resonances obtained from the small segments of the Π laser beam cross section at four distances r from the beam center. The resonances are nearly identical except for the resonance obtained close to rim of the beam (pointed to with the arrow). The beam diameter is 6 mm and the total intensity is 0.5 mW/cm^2 . Note that the magnetic field range is smaller than in Figs. 3.12 and 3.14.

overall laser intensity on line shapes of the EIT obtained in different segments of the Π -shaped laser beam. The curves in Figs. 3.17(a) and 3.17(b) are theoretical and experimental Hanle EIT resonances obtained for the laser intensity 0.5 mW/cm^2 at different positions of the small aperture along the beam diameter of 6 mm. At lower laser intensity, transmission minima are barely visible (theory) or missing (experiment) in the Hanle EIT profiles, because of the weak optical pumping. Since there are diffraction effects between the planes of the two apertures (see Fig. 3.11) the radial position of the collecting aperture does not map exactly the corresponding position in the atomic cell. This introduces some averaging that may explain why the structures are smoother in the experiments with respect to the calculations. In Fig. 3.18 we show the total excited-state populations for an atom traversing the beam with velocity 180 m/s as a function of the radial distance from the beam center at different magnetic fields. Even at a very high magnetic field ($75 \mu\text{T}$), the population is not zero as it was at high laser intensities (see Fig. 3.15) because

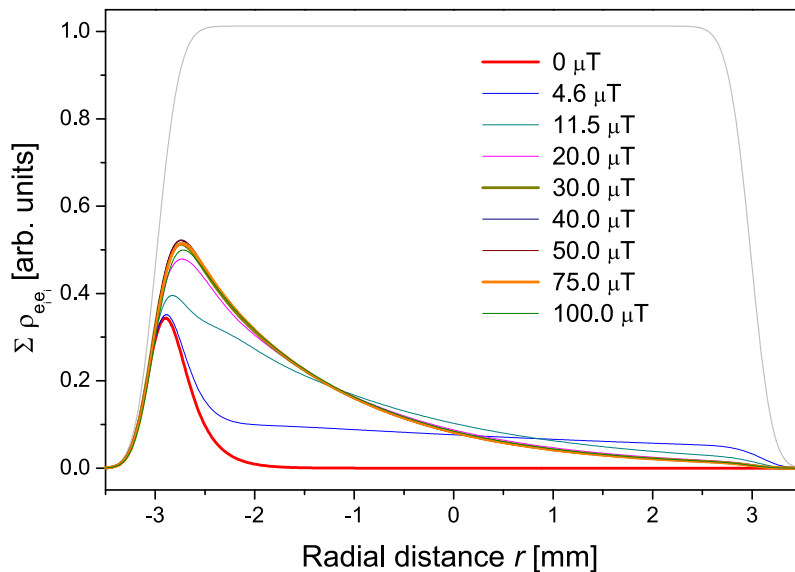


Figure 3.18: Calculated total population of all Zeeman sublevels of the $F_e = 1$ excited level at different magnetic fields as a function of position along the 6-mm beam diameter of II-shaped laser beam. The curves corresponding to the magnetic fields 0 – 100 μT from the legend appear from bottom to top, respectively, at $r = -2.5$ mm. The curves for $B \gtrsim 20$ μT are almost identical. The atomic velocity is the most probable velocity at room temperature (180 m/s). The thin gray line represents the laser beam cross section profile.

optical pumping to the $F_g = 1$ level is not as efficient. In this case the transmission of the vapor will not increase at high magnetic fields and consequently there are no transmission minima at Hanle EIT resonance profiles at any position along the beam diameter.

As discussed above, EIT line shapes obtained in different parts of the II-shaped laser beam cross section are determined by evolution of the dark states and (particularly around the beam center) by the optical pumping. On the other hand, the change of atomic coherence in the magnetic field is found to play a significant role in the line shapes obtained in parts of the Gaussian laser beam cross section. Results in Figs. 3.19(a) and 3.19(b) confirm that the phase of atomic coherence is almost constant during atomic transit through the II-shaped laser beam. Here we compare the calculated phase of the coherence, induced between the $m_F = -1$ and $m_F = 1$ Zeeman sublevels of $F_g = 2$ hyperfine level for atoms passing through the II laser beam. The magnetic field during transit time of an atom is assumed constant. The results are shown for the magnetic field of 30 μT at which transmission minima

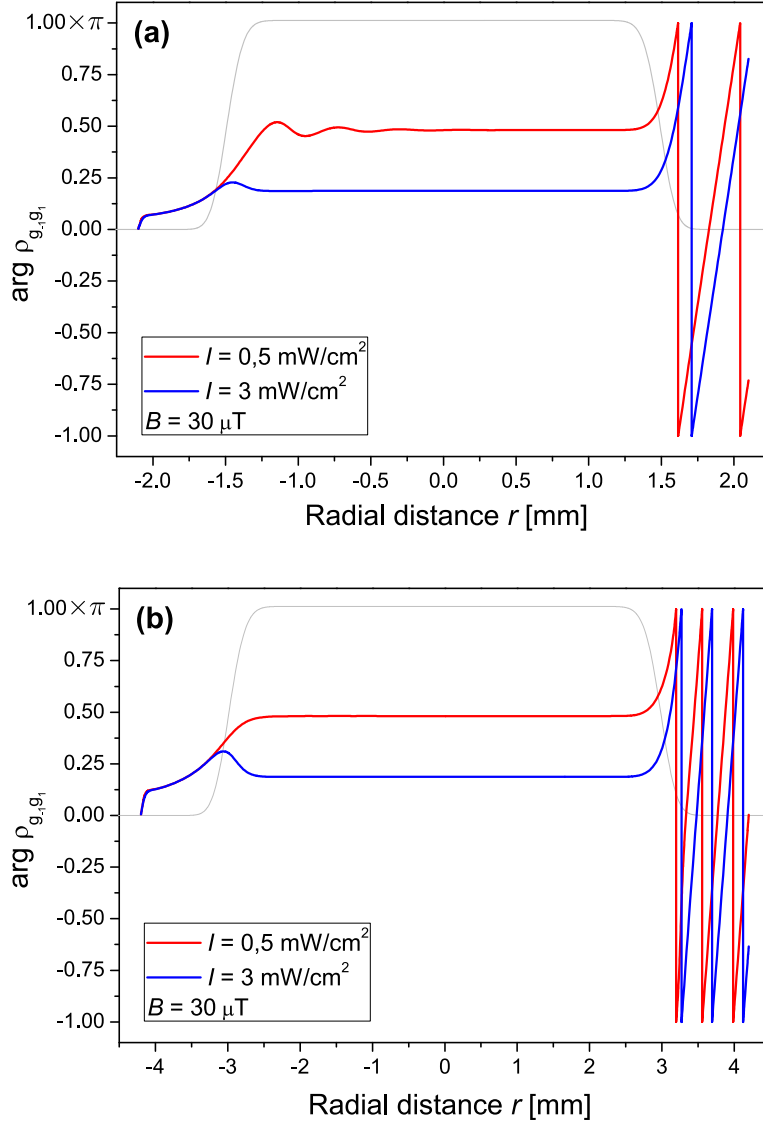


Figure 3.19: Change of the argument of atomic coherence ρ_{g_{-1}, g_1} during atomic passage through the 3 mm (a) or 6 mm (b) wide Π laser beam for two laser intensities 0.5 mW/cm^2 and 3 mW/cm^2 . It is obvious that the phase is constant during atom passage through the Π laser beam, regardless of the laser intensity. The magnetic field value of $30 \text{ } \mu\text{T}$ is chosen because the transmission minima in the Hanle EIT resonances appear exactly at those values in corresponding laser beam profiles. The beam profile is presented by the gray line.

appear in the related Hanle EIT resonances. Since the laser electric field tends to keep the phase of the coherence constant while the magnetic field tends to change the phase, when both magnetic and electric field are present, the phase of atomic

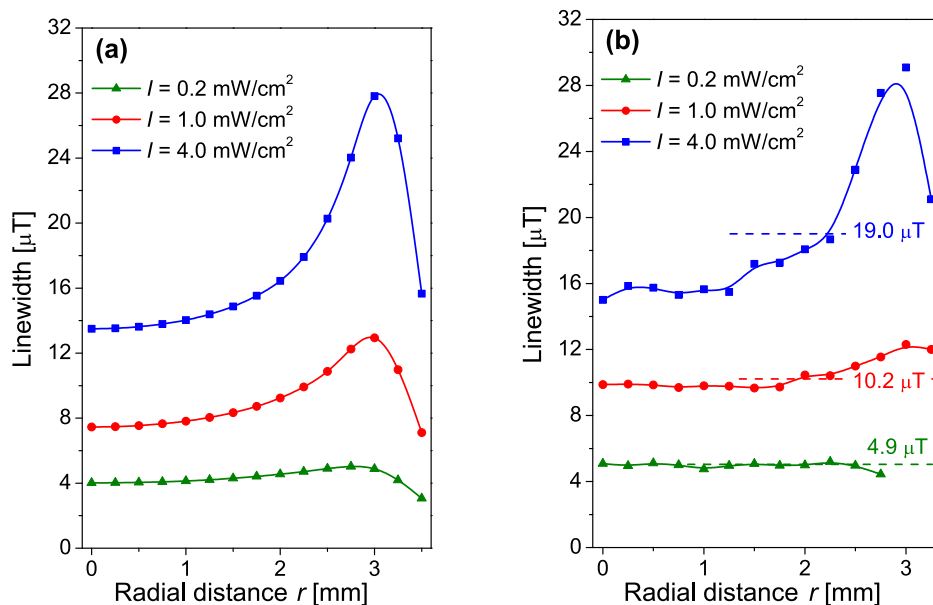


Figure 3.20: Theoretical (a) and experimental (b) Hanle EIT line-widths at different positions of small aperture along the 6-mm-diameter II-shaped laser beam. I is the laser intensity. The dashed lines in (b) denote the Hanle EIT line-widths when the entire laser beam is detected.

coherence will depend on the magnitudes of these two fields. The atom is coherently prepared shortly after entering the laser beam and the phase is kept fixed by the strong laser field across the beam. Therefore, it is not the change of the phase that affects the observed Hanle EIT line shapes for the II laser beam.

Figures 3.20(a) and 3.20(b) show theoretical and experimental results for the dependence of line-widths of the Hanle EIT resonances on the radial position r of the small aperture along the 6-mm diameter of the II-shaped laser beam. The dashed lines in Fig. 3.20(b) denote the Hanle EIT line-widths when the whole laser beam is detected. Results are given for three different laser intensities. It is obvious that there is Hanle EIT line narrowing from the edge toward the beam center. This is population-loss-induced transit time narrowing [59, 60]. As seen in Fig. 3.20, it is more pronounced at higher laser intensities, when most significant Hanle EIT narrowing apparently occurs in the region close to the beam edges, i.e., very soon after the atom enters the beam.

At the end this section, one note is suitable. The appearance of transmission minima, as sidebands to the EIT resonance, in the inner regions of the II laser beam is shown to be due to strong dependence of optical pumping on the magnetic field.

Transmission minima were also observed for Hanle EIT resonances obtained using the Gaussian laser beam, but such EIT line shapes were only observed in the wings of the beam. Their presence was attributed to the interference of the laser light in the beam wings and coherently prepared atoms coming from the central part of the beam. Thus, essentially different physical mechanisms, *optical pumping (incoherent)* in II laser beams and *Ramsey-like effect (coherent)* in Gaussian laser beams, yield seemingly similar results, i.e., the appearance of the transmission minima in Hanle EIT line shapes. Thus, it is apparent that for the proper modeling of experiments and identification and understanding of dominant processes affecting the atomic state evolution within the laser beam, it is essential to take into account a real beam profile.

3.5 Influence of laser beam profile on Hanle EIA

Electromagnetically induced absorption (EIA) [5, 6], is another coherent phenomenon that manifests in the increase of the medium resonant absorption of a probe beam in the presence of a pump beam. EIA appears in many different systems [8, 61, 62, 63, 64, 65]. It is shown that three different mechanisms can lead to the emergence of EIA: transfer of coherence (TOC) [8, 61], transfer of population (TOP) [8, 62] and quantum interference among competing two-photon transitions [65, 66]. EIA due to TOP between the Zeeman levels of the ground hyperfine state occurs when pump and probe lasers have the same polarization, while EIA due to TOC occurs for perpendicularly polarized lasers. In Hanle configuration, EIA depends on the ground-state Zeeman coherences and on the efficiency of spontaneous coherence transfer from the excited to the ground levels [67].

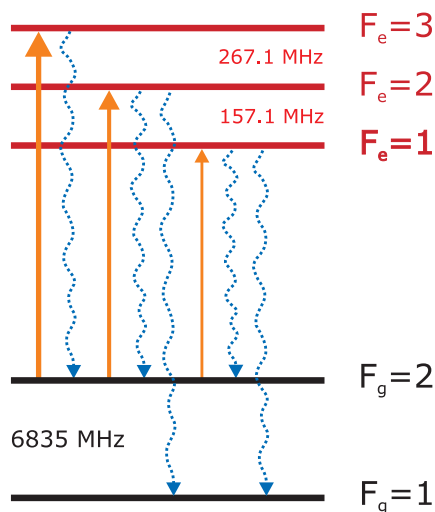


Figure 3.21: Energy level diagram for D_2 line transitions considered in the theoretical model. Solid lines represent transitions induced by the laser, while dotted lines correspond to possible spontaneous emission channels from excited levels. Frequency differences between adjacent hyperfine levels are shown.

The goal of this section is to give a comparative study of the Hanle EIA resonances obtained with two radial laser beam profiles, Gaussian and Π -shaped. The investigation was performed on ^{87}Rb vapor in a vacuum cell at the D_2 line transition $F_g = 2 \rightarrow F_e = 3$ in the Hanle configuration. EIA obtained from two beam profiles from the entire 3-mm-diameter laser beam and, also, obtained from the

small segments of the laser beam cross section is examined. Studies of EIA from selected parts of the laser beam were done by using the aperture movable along the laser beam radius. Similar investigations for EIT presented in previous sections have demonstrated the essential influence of different parts of the laser beam cross section on the overall EIT resonances, that is, on the EIT from the entire laser beam. The theoretical model gives the Hanle resonance line-shapes in accordance with measurements. Calculations are based on the optical Bloch equations for transient evolution of the atomic state during interaction with laser light of a profiled intensity. The details of the theoretical model are given in the section 2.3. Diagram of energy levels taken into account in calculations is shown in Fig. 3.21. Although the laser is locked to the $F_g = 2 \rightarrow F_e = 3$ transition, the excited hyperfine levels $F_e = 2$ and $F_e = 1$ are also laser coupled due to the Doppler broadening and must be considered.

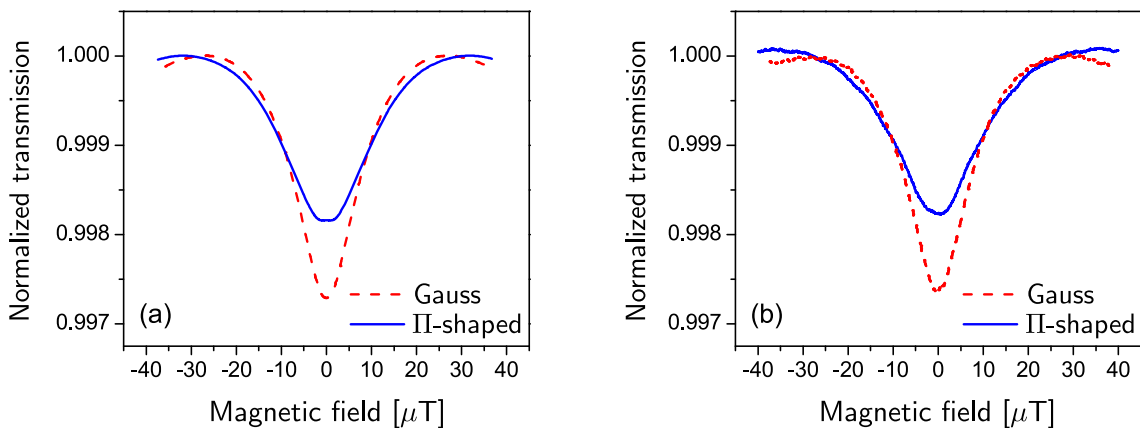


Figure 3.22: Theoretical (a) and experimental (b) Hanle EIA resonances for the Gaussian (dashed red curves) and II-shaped (solid blue curves) beam profiles. Laser intensity is 2 mW/cm^2 .

Figure 3.22 shows a comparison of Hanle EIA resonances for Gaussian and II-shaped profiles, at a laser intensity of 2 mW/cm^2 . The quoted laser intensity corresponds to the intensity of the whole laser beam, that is, the measured laser power at the entrance of the cell divided by the beam area. Figure 3.22(a) shows theoretical results and Fig. 3.22(b) corresponds to experiment. Key features of any resonance are amplitude and line-width. It can be seen that for an intensity of 2 mW/cm^2 , the II-shaped beam profile yields resonances with a greater line-width. Figure 3.23 presents theoretical, and Fig. 3.24 experimental, results for the amplitudes and line-

widths of EIA resonances as a function of the laser intensity, for both laser profiles. EIA amplitudes are normalized to transmitted laser intensity. In each figure we give results obtained using two radial laser beam profiles. It is shown that amplitude intensity dependences for both profiles initially rise quite rapidly, until they reach a maximum at approximately 0.5 mW/cm^2 . Further decrease with the laser intensity is a consequence of saturation.

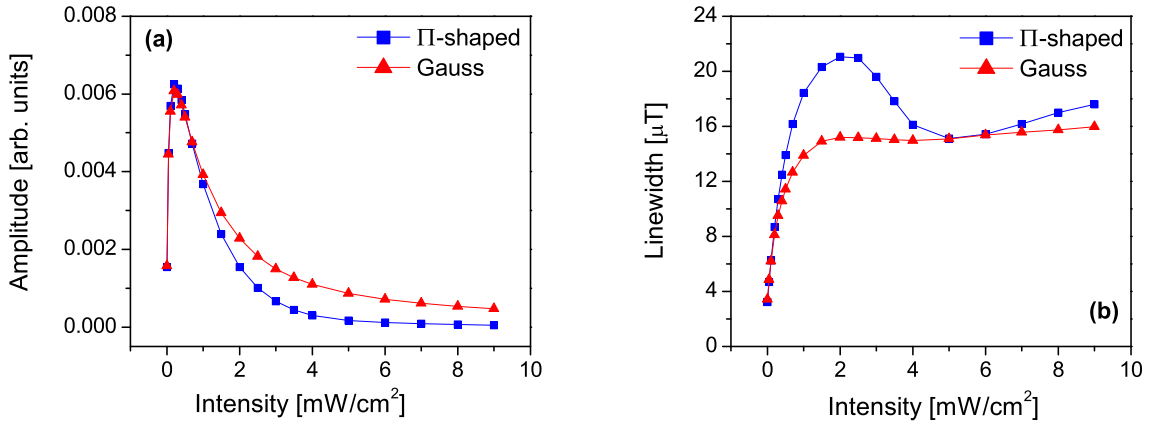


Figure 3.23: Theoretical (a) amplitudes and (b) line-widths for Gaussian (red, triangles) and Π -shaped (blue, squares) beam profiles as a function of the laser intensity.

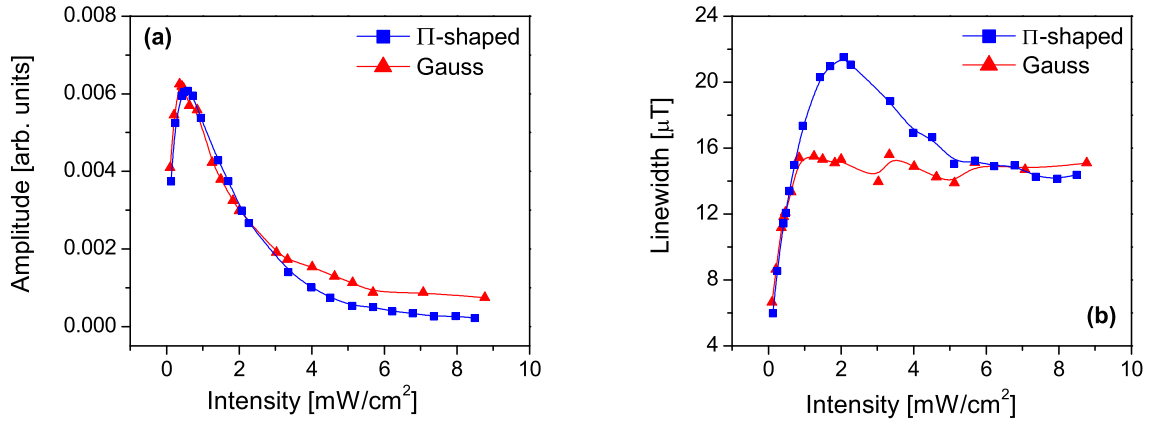


Figure 3.24: Experimental (a) amplitudes and (b) line-widths for Gaussian (red, triangles) and Π -shaped (blue, squares) beam profiles as a function of the laser intensity.

Resonance line-widths obtained from the two beam profiles have different dependences on the laser intensity. For both beam profiles there is a very rapid increase

at low intensities. However, the Π -shaped profile gives a pronounced maximum at about 2 mW/cm^2 , while the Gaussian profile provides an almost-flat line-width dependence at these and higher intensities. EIA intensity narrowing at high laser intensities, assuming a Π -shaped beam, was already noted in [47]. Differences in line-widths are most notable for moderate intensities and are due to different transient dynamics of atoms passing through the laser beam. During atomic transit through the laser beam the atomic state changes due to competitive effects of the laser excitation and the external magnetic field. The laser continuously forces the atom to be “aligned” with the electric field, in which case the state of the atom relates to the appearance of EIA. The external magnetic field causes oscillations of the atomic state at the corresponding Larmor frequency. At low laser intensities, the influence of the magnetic field is more significant, so that the atomic state “aligned” with the electric field is degraded more easily. For the Gaussian laser beam, the atoms experience an omnichanging laser field, while the Π -shaped beam provides an almost-constant electric field. This difference reflects directly on the robustness of the “aligned” atomic state with respect to the external magnetic field because the spatial change in the laser field decreases the robustness by inducing an extra variation of the atomic state. Under a zero external magnetic field atoms reach an “aligned” state, and absorption reaches a maximum. A nonzero magnetic field degrades that state, reducing the absorption. If the “aligned” state is more robust, the absorption decreases less for the same magnetic field. Therefore, greater robustness of the EIA with respect to the external magnetic field requires a larger magnetic field to halve the peak absorption and hence yields larger EIA line-widths for the Π -shaped beam, compared to the Gaussian beam. When the laser intensity is high enough, differences in laser beam profile become less important, yielding very similar line-widths for both profiles.

Hanle EIA obtained from only a small parts of the laser beam cross section, as a function of the magnetic field, are also studied. When the intensity of the light passing through the small part of the beam cross section is low, the part plays the role of the probe beam. Therefore, throughout the text it will be referred as quasi-probe. The rest of the laser beam can be considered as the pump. In such case, resulting resonances are either due to coherently prepared atoms coming into the quasi-probe from the surrounding pump region or because of EIA induced by the quasi-probe. Relative contributions of probing and inducing EIA within the quasi-probe depend on the overall laser intensity, shape of the beam (Gaussian or

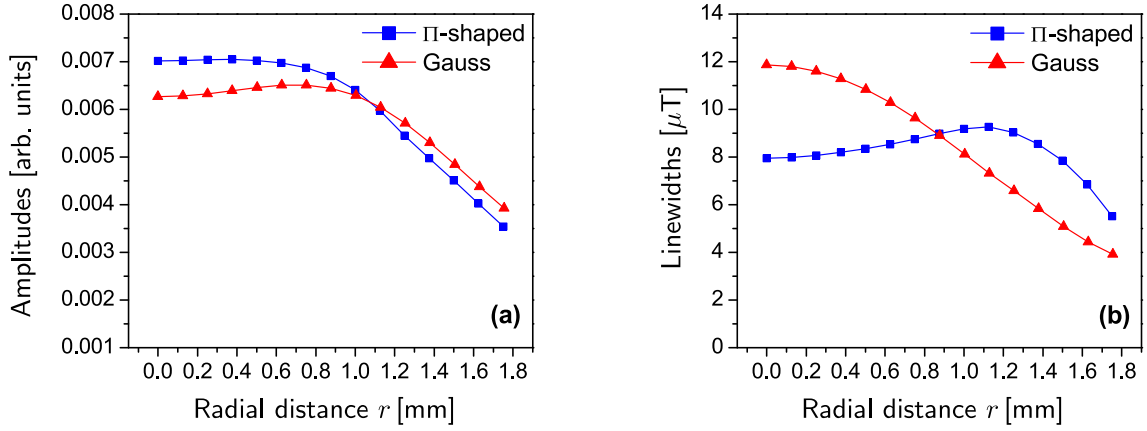


Figure 3.25: Theoretical results for (a) amplitudes and (b) line-widths as a function of the radial position of the 0.5-mm aperture for Gaussian (red, triangles) and Π -shaped (blue, squares) beam profiles. Laser intensity is 0.2 mW/cm^2 . Points correspond to different radial distances of the 0.5-mm aperture selecting the beam sections.

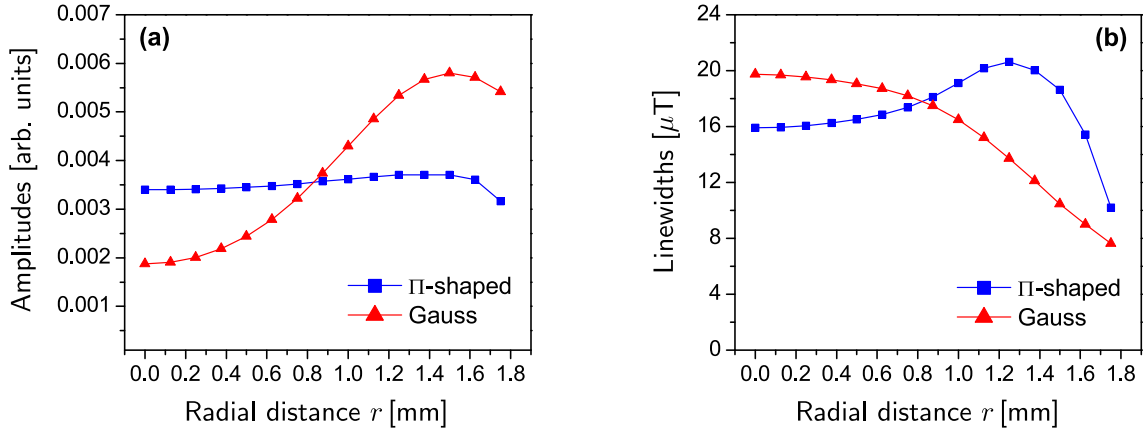


Figure 3.26: Theoretical results for (a) amplitude and (b) line-width dependence on the radial position of the 0.5-mm aperture determining the beam segment for Gaussian (red, triangles) and Π -shaped (blue, squares) beam profiles. Laser intensity is 1 mW/cm^2 .

Π -shaped), and radial distance of the quasi-probe from the laser beam center.

Figures 3.25 and 3.26 present theoretical results for amplitudes (Figs. 3.25(a) and 3.26(a)) and line-widths (Figs. 3.25(b) and 3.26(b)) of Hanle quasi-probe EIA resonances as a function of radial positions of the selected beam segment, at a laser intensity of 0.2 and 1 mW/cm^2 , respectively. Figures 3.27 and 3.28 are corresponding

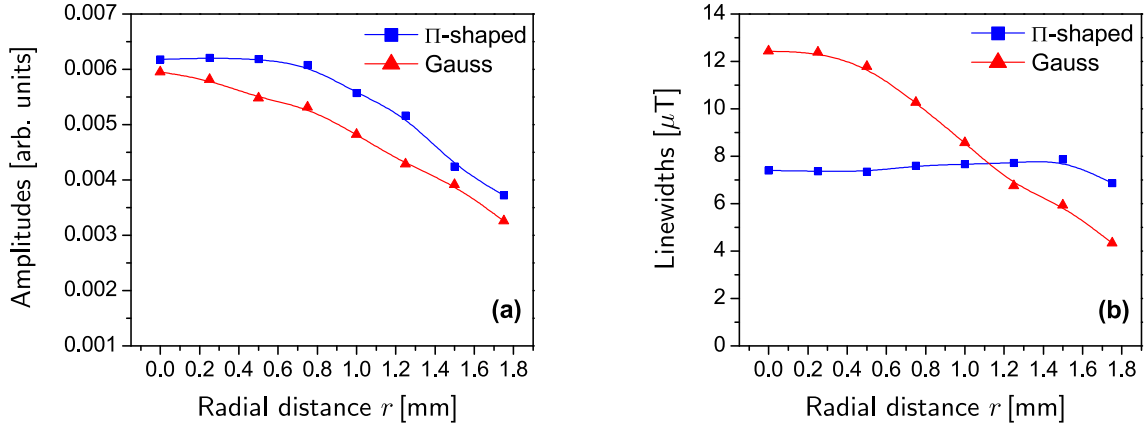


Figure 3.27: Experimental results for (a) amplitudes and (b) line-widths of EIA obtained from laser beam sections at different radial distances from the laser beam center for Gaussian (red, triangles) and Π -shaped (blue, squares) beam profiles. Laser intensity is 0.2 mW/cm^2 .

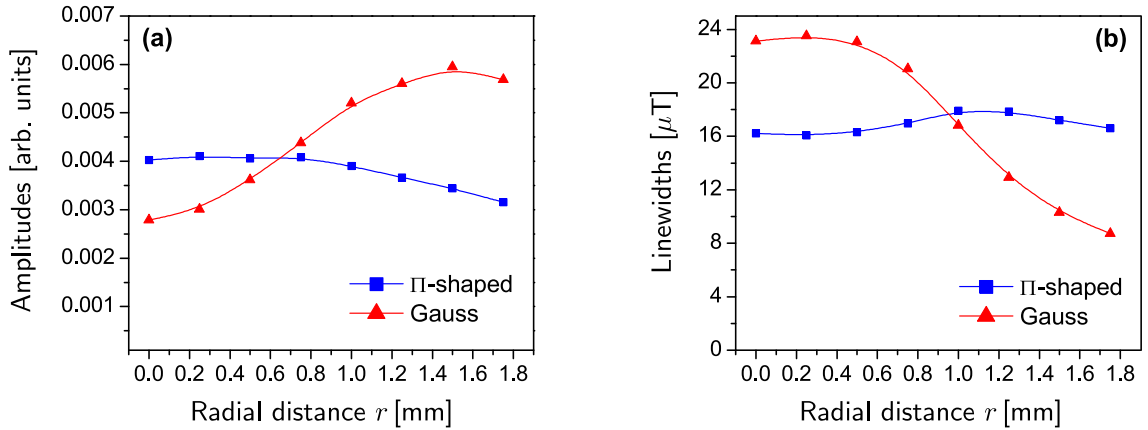


Figure 3.28: Experimental results for (a) amplitude and (b) line-width EIA dependence on the radial position of the 0.5-mm aperture for Gaussian (red, triangles) and Π -shaped (blue, squares) beam profiles. Laser intensity is 1 mW/cm^2 .

measurements. While resonance line-widths for the Π -shaped profile are largest at the outer parts of the laser beam, line-widths for the Gaussian laser beam are larger near the laser beam center. This can be attributed to the fact that in the region near the beam boundary, the Π -shaped profile has a higher intensity than the Gaussian. The intensity inside the Gaussian beam increases toward the beam center, causing EIA resonance broadening, so the situation reverses around the radial distance where the Gaussian beam becomes more intense (note that it is two times more intense at

the center than the Π -shaped beam of the same average intensity). Note that EIA resonances are particularly narrow in the wings of the Gaussian beam, where a very low intensity quasi-probe really probes the “aligned” EIA state of the atoms coming into the quasi-probe from the rest of the beam. At places closer to the beam center, the quasi-probe simultaneously probes and induces EIA, and eventually the induced effect dominates over probing. This leads to increased line-widths as the quasi-probe moves toward the beam center. In a Π -shaped beam, the passing atoms experience a very rapid increase in laser intensity only at the beam edge and a constant intensity inside the beam. A large variation in laser intensity causes broadening of line-widths and a resulting maximum of line-widths near the beam edge. As atoms move toward the beam center, the constant laser intensity experienced by the atoms and the longer average time of flight inside the Π -shaped beam cause the gradual narrowing of EIA resonances as the atoms move toward the beam center. In other words, the decrease in line-widths upon approaching the beam center for a Π -shaped beam is a typical transit-time narrowing.

Radial behavior of EIA amplitudes is notably different for two laser beam shapes at higher laser intensities, as shown in Figs. 3.26 and 3.28 for 1 mW/cm^2 . Amplitudes for the Π -shaped profile do not show large variations along the beam in comparison with the Gaussian profile, where the initial rise in amplitudes turns into a significant and constant decrease. A strong laser intensity near the center of the Gaussian beam, above $\sim 1 \text{ mW/cm}^2$, leads to a lower amplitude in comparison to amplitudes farther from the beam center. Similar behavior, a decrease upon approaching the center, becomes present also in Π -shaped beams of a laser intensity higher than 1 mW/cm^2 . This is attributed to the fact that at high intensities, the laser field dominates over the influence of the magnetic field, so that the effect of the beam profile on the EIA amplitudes becomes less pronounced.

EIA amplitudes and line-widths depend on ambient conditions, stray magnetic field, and room temperature. Effects of stray magnetic field are negligible due to shielding by the triple-layered μ -metal cylinder. The variation of room temperature from one set of measurements to the other was within $\pm 1 \text{ }^\circ\text{C}$. These temperature variations have a negligible influence on line-widths but may result in changes in EIA amplitudes. Ambient temperature variation shifts the amplitudes radial dependencies, presented in Figs. 3.27(a) and 3.28(a), by 10 %, preserving their shape.

In the present section it is demonstrated that the atoms evolve very differently depending on the passage through one or the another profiled beam. This is shown

by the Hanle EIA obtained in transmission from only small segment of the entire laser beam. In this way the quasi-probe EIA is studied, i.e., EIA due to some small beam part that is surrounded by the rest of the laser beam having the pump role. Since at very low laser intensities, the quasi-probe probes coherently prepared atoms moving toward the selected region, EIA resonances are narrower in outer regions of the Gaussian beam. At higher laser intensities the quasi-probe can also generate EIA in atoms. Thus, near the center of the Gaussian beam, EIA resonances are widest due to higher power broadening. For a Π -shaped laser beam, the quasi-probe gives the narrowest EIA resonances at the beam center, due to transit-time narrowing of the coherent resonances. EIA amplitudes, in the range of applied laser intensities, are lowest (highest) near the laser beam center for the Gaussian (Π -shaped) profile. Thus, outer regions of the Gaussian beam and central regions of the Π -shaped beam are the most valuable regions in the sense that they contribute the narrowest line-widths and highest amplitudes to the overall EIA. The opposite variation of quasi-probe EIA line-widths with the distance from the laser beam center for the two beam profiles makes the line-widths of whole-beam EIA less dependent on the laser beam profile. Only in the range of laser intensities $1 - 4 \text{ mW/cm}^2$ the overall EIA line-widths for the Π -shaped laser beam have a maximum which exceeds the corresponding values obtained with the Gaussian beam that yields a flat intensity dependence.

The results of this section show that it is important to take into account the real laser beam profile for proper modeling and analysis of coherent effects in alkali metal vapors. Differences in EIA line-widths obtained using two laser radial beam profiles imply that a theory with assumed Π -shaped radial dependence (common assumption in majority of models) will not produce good agreement with experiments done usually using a Gaussian or similar beam shape. One practical consequence of these results is that detecting only the wings of the Gaussian laser beam will give narrower EIA resonances than in the case of entire-beam detection.

4. Stark-chirped rapid adiabatic passage

4.1 Adiabatic passage

SCRAP technique is a special case of a general adiabatic passage technique. Thus, the essentials of adiabatic passage will be presented first and particularities of SCRAP will be addressed afterward.

The realization of specific changes in the state vector by resonant excitation requires careful control of the temporal laser pulse shape. Additionally, such excitation has limited applicability when the treated ensemble has a range of detunings, like in Doppler broadened atomic vapors. There is an alternative pulsed excitation procedure that overcomes such difficulties. It can yield equal excitation over a distribution of Doppler-induced detunings, independent of the temporal pulse shape. Specifically, the excitation pulse incorporates not only a variation of the Rabi frequency but a monotonic sweep of the laser detuning. Rapid adiabatic passage (RAP) [11, 12] technique requires that state vector changes must be finished during a time interval that is shorter than any decoherence process (like spontaneous emission). Although the overall action must be rapid on that time scale, within that time the detuning should vary slowly with time, i.e. adiabatically. The resulting evolution of the state vector is an example of adiabatic following in which the state vector follows a path in Hilbert space defined by an adiabatic state.

In the simplest idealization of RAP the detuning linearly changes in time, i.e., $\Delta(t) = \Delta_0 + rt$, where r is the rate at which the detuning varies and Δ_0 is a fixed detuning, e.g. corresponding to a single Doppler shift. Such situation can be realized by varying the laser frequency linearly with time, i.e. by *chirping* the laser frequency. When an atom is excited by the laser subjected to a sweep of frequency around an atomic transition, the behavior of the population of the states coupled by the laser can be understood with the help of an alternative Hilbert-space basis, the one chosen

as instantaneous eigenbasis of the time varying Hamiltonian $W(t)$

$$W(t)\Phi_n(t) = \varepsilon_n\Phi_n(t). \quad (4.1)$$

The states $\Phi_n(t)$ are called *adiabatic* states, in contrast to the *diabatic* states $\tilde{\psi}_n(t)$ (2.6). The two-level RWA Hamiltonian of Eq. (2.7) that incorporates time variation of both the Rabi frequency and the detuning is

$$W(t) = \hbar \begin{bmatrix} 0 & \frac{1}{2}\Omega(t) \\ \frac{1}{2}\Omega^*(t) & \Delta(t) \end{bmatrix}. \quad (4.2)$$

The eigenvalues of the RWA Hamiltonian, the *adiabatic energies*, are

$$\varepsilon_{\pm}(t) = \frac{\hbar}{2}(\Delta(t) \pm \tilde{\Omega}(t)), \quad \text{where } \tilde{\Omega}(t) = \sqrt{|\Omega(t)|^2 + \Delta(t)^2}. \quad (4.3)$$

The diagonal elements of the RWA Hamiltonian, 0 and $\hbar\Delta(t)$ in the case of (4.2), are known as *diabatic energies*. The adiabatic states in the present case are of the form

$$\Phi_+(t) = \begin{bmatrix} e^{-i\phi} \sin \theta(t) \\ \cos \theta(t) \end{bmatrix}, \quad \Phi_-(t) = \begin{bmatrix} \cos \theta(t) \\ -e^{i\phi} \sin \theta(t) \end{bmatrix}, \quad (4.4)$$

where $\cot(2\theta(t)) = \Delta(t)/|\Omega(t)|$.

When the state vector is initially aligned with one adiabatic state, and the RWA Hamiltonian changes slowly (adiabatically), then the state vector remains aligned with this single adiabatic state. In other words, the state vector adiabatically follows the adiabatic state during the adiabatic evolution. This is known as *adiabatic following*. The adiabatic state varies with time, and so the state vector varies when viewed in the basis of diabatic states. The result of the adiabatic following can be a transfer of population if the followed adiabatic state initially corresponds to one of the diabatic states and changes into another diabatic state at the end of the evolution. This can be realized by aligning the initial state with $\tilde{\psi}_1$ and adiabatically changing $\Delta(t)$ and $\Omega(t)$ so that $\theta(t)$ sweeps from $\theta(t_i) = 0$ to $\theta(t_f) = \pi/2$. This corresponds to the change of the adiabatic state from $\Phi_-(t_i) = \tilde{\psi}_1(t_i)$ to $\Phi_-(t_f) = \tilde{\psi}_2(t_f)$ and enables the adiabatic passage of the population from the state 1 to the state 2.

The adiabatic passage is often visualized by presenting plots of adiabatic energies along with plots of diabatic energies. For a two-level system case the diabatic energies are 0 and $\Delta(t)$. When there is a sweep of detuning from e.g. negative to

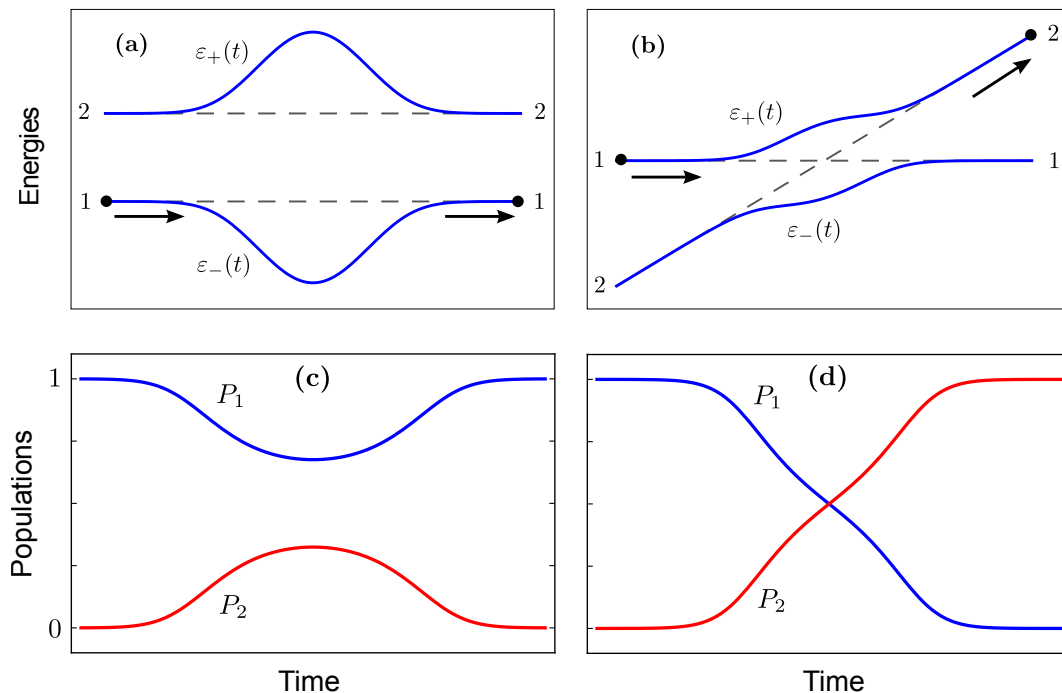


Figure 4.1: Top parts: diabatic (dashed curves) and adiabatic energies (solid curves) for two-level system. Bottom parts: corresponding population histories for state 1 (blue curve) and state 2 (red curve). Left: adiabatic evolution with constant detuning. Right: adiabatic evolution with chirped detuning. System points on the energy curves are related to initial and final states. Arrows indicate the motion of the system points along adiabatic energy curves.

positive values, then the diabatic energy curves cross – this occurs when $\Delta(t) = 0$. However, the adiabatic curves $\varepsilon_{\pm}(t)$ do not cross if there is any, however small, Rabi frequency at the moment of crossing of diabatic energy curves. The adiabatic energy curves have so called *avoided crossing*. Figure 4.1 shows the behavior of these curves, and the corresponding population histories during adiabatic evolution, for two cases of a two-level system subject to a pulsed Rabi frequency. The left-hand pair of plots illustrates the case when the detuning is kept fixed. The diabatic energies remain constant, while the adiabatic energies exhibit reversible changes produced by the Rabi-frequency variation with time. With the presented choice of parameters, there occurs complete population return. The right-hand pair of plots shows the influence of a chirped detuning on these curves. The diabatic curve for state 2 rises linearly with time, crossing that of state 1 at $t = 0$. For large values of $|t|$, far from $t = 0$, the Rabi frequency is negligible, and the adiabatic curves coincide with the diabatic

curves 0 and $\Delta(t)$. However, as the Rabi frequency becomes larger, the two sets of curves differ and avoided crossing occurs.

To explain the population histories associated with such curves let us begin by considering the system at early times - the left-hand side of the figures. Suppose the state vector is initially aligned with a single diabatic state, $\tilde{\psi}_1$. At these times there is no Rabi interaction, and so the diabatic and adiabatic states coincide. The initial state vector is represented by a system point on the coinciding diabatic and adiabatic curves. As time increases and the energies vary, this system point passes from left to right, denoting the changes of the energies with time. Its association with a single curve can be valid only for two extreme idealized cases - corresponding to either fast (diabatic) or slow (adiabatic) variation of the RWA Hamiltonian.

During the rapid variation of the RWA Hamiltonian, the state vector will remain aligned with the starting diabatic state, and the system point will follow the (dashed) diabatic curve in Figure 4.1(b), corresponding to the energy of the diabatic state 1. The system point moving along this line, crosses the diabatic curve for the state 2. The system remains in the state 1 until the end, i.e., no transition occurs.

By contrast, when the changes of the RWA Hamiltonian are sufficiently slow (adiabatic), the state vector will remain aligned with the starting adiabatic state. The system point will follow the adiabatic curve that starts from the state 1 and does not cross any other curve. Initially its path coincides with diabatic curve for the state 1, but at later times the path joins the diabatic curve for the state 2, i.e., an adiabatic transition occurs.

The realization of complete population transfer via adiabatic passage requires the detuning to sweep slowly through the resonance. Detuning is the difference between the Bohr atomic transition frequency and the laser carrier frequency, so the variation of either of these two frequencies will provide the required result. The Bohr frequency, being proportional to the energy difference between two atomic levels, can be changed by any slowly varying non-resonant electric or magnetic field. One possibility is to use pulses of non-resonant laser light to subject the atom to a slowly varying electric field and to induce a (dynamic) Stark shifts of the atomic energy levels [68, 69], i.e., Stark chirp of the detuning. This is the basic idea of SCRAP.

4.1.1 Two-state SCRAP

Two-state SCRAP technique uses two sequential laser pulses: pump laser pulse having the carrier frequency ω_p near the atomic Bohr transition frequency $\omega_2 - \omega_1$ and strong far-off-resonant Stark laser pulse. Pump pulse drives the population between the states 1 and 2, while Stark pulse modifies the transition frequency by Stark shifting the energies of the two states, so that the detuning $\Delta(t)$ becomes

$$\Delta(t) = \omega_2 - \omega_1 - \omega_p + S_2(t) - S_1(t). \quad (4.5)$$

The detuning can be naturally represented as the sum of two terms $\Delta(t) = \Delta_{21} + S_{21}(t)$. The first term, $\Delta_{21} = \omega_2 - \omega_1 - \omega_p$, is static detuning of the pump laser from the Bohr atomic transition frequency in the absence of radiation. The ground state Stark shift $S_1(t)$ and the excited state Stark shift $S_2(t)$ are different (usually $|S_1(t)| \ll |S_2(t)|$) leading to the net Stark shift $S_{21}(t) = S_2(t) - S_1(t)$ of the detuning (4.5). The dynamic Stark shift $S_n(t)$ of the state n ($n = 1, 2$) has the contribution of both the pump and the Stark fields

$$S_1(t) = S_1^p \mathcal{P}(t) + S_1^S \mathcal{S}(t), \quad (4.6a)$$

$$S_2(t) = S_2^p \mathcal{P}(t) + S_2^S \mathcal{S}(t), \quad (4.6b)$$

where the dimensionless functions $\mathcal{P}(t)$ and $\mathcal{S}(t)$ are the envelopes of the pump and the Stark laser intensities, while S_n^p and S_n^S ($n = 1, 2$) are maximal Stark shifts of the state n due to pump and Stark laser, respectively. The pump laser induced Stark shifts can be significant for multiphoton transitions but are negligible for single photon transitions. Thus, the shifts induced by the Stark field are predominant

$$S_{21}(t) \approx (S_2^S - S_1^S) \mathcal{S}(t). \quad (4.7)$$

The SCRAP technique can be explained by inspecting a time variation of the diabatic and adiabatic energy curves (Fig. 4.2). Initially, the pump carrier frequency is chosen such that the diabatic energy $\varepsilon_2(t)$ of the state 2 is higher than the diabatic energy $\varepsilon_1(t)$ of the state 1. During the pulse sequence, the Stark pulse shifts $\varepsilon_2(t)$ relative to $\varepsilon_1(t)$ producing two diabatic energy crossings – first during the rise and second during the fall of the Stark pulse. The adiabatic evolution occurs at some crossing if the pump pulse is sufficiently strong. SCRAP method relies on delayed

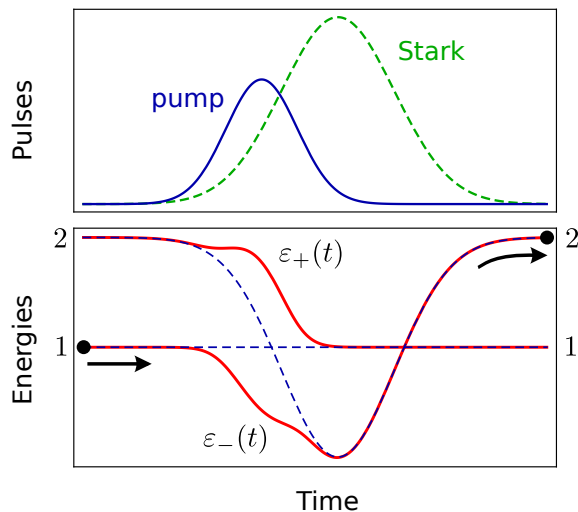


Figure 4.2: Top: Time dependencies of the pump (blue curve) and the Stark (green curve) laser pulses. Bottom: Related adiabatic (solid curves) and diabatic (dashed curves) energies versus time. System points on the energy curves are related to initial and final states. Arrows indicate the motion of the system points along adiabatic energy curves.

pulses so that the pump Rabi frequency is significant at exactly one of the crossings. In the case shown in Fig. 4.2, the system starting in the state 1, passes through the first crossing adiabatically following the state $\Phi_-(t)$, and makes a transition to the state 2. At the second crossing the pump laser field is negligible and the system diabatically follows the diabatic state $\tilde{\psi}_2(t)$, to which it was associated prior to this crossing. The final result of this adiabatic-diabatic evolution sequence is the complete population transfer from the state 1 to the state 2.

4.1.2 Three-state SCRAP

SCRAP in a three-state system provides an efficient way of transferring the population from ground state 1 to ground state 2 via minimally populated excited state 3. The transfer is realized by use of three sequential laser pulses: pump and Stokes pulses coupling the transitions $1 \rightarrow 3$ and $2 \rightarrow 3$, respectively, and far-off-resonant Stark pulse that creates a suitable set of level crossings in the energy diagram of the

system. The RWA Hamiltonian of the laser-excited three-state system is

$$\mathbf{W}(t) = \hbar \begin{bmatrix} 0 & 0 & \frac{1}{2}\Omega_p(t) \\ 0 & \Delta_{21} + S_{21}(t) & \frac{1}{2}\Omega_S(t) \\ \frac{1}{2}\Omega_p^*(t) & \frac{1}{2}\Omega_S^*(t) & \Delta_{31} + S_{31}(t) \end{bmatrix}, \quad (4.8)$$

where $\Omega_p(t)$ and $\Omega_S(t)$ are Rabi frequencies associated with the pump and Stokes fields, respectively. Δ_{21} and Δ_{31} represent the static detunings, which for one-photon transitions are given by

$$\Delta_{21} = \omega_2 - \omega_1 + \omega_S - \omega_p, \quad (4.9a)$$

$$\Delta_{31} = \omega_3 - \omega_1 - \omega_p. \quad (4.9b)$$

The dynamical Stark shifts

$$S_{mn}(t) = S_m(t) - S_n(t), \quad (4.10)$$

are the differences between the Stark shifts $S_m(t)$ and $S_n(t)$ of the states m and n ($m, n = 1, 2, 3$). Similarly to two-state SCRAP, the shifts induced by the Stark field are overwhelming, so that

$$S_{mn}(t) \approx (S_m^S - S_n^S)\mathcal{S}(t), \quad (4.11)$$

where S_m^S and S_n^S are maximal shifts due to Stark laser and $\mathcal{S}(t)$ is the envelope of the Stark laser intensity. The adiabatic eigenenergies $\varepsilon_1(t)$, $\varepsilon_2(t)$ and $\varepsilon_3(t)$ of the Hamiltonian (4.8) are roots of a cubic equation and are too cumbersome to be given in detail. Denote with $\Phi_1(t)$, $\Phi_2(t)$ and $\Phi_3(t)$ the corresponding adiabatic eigenstates.

It was shown in [31] that successful population transfer from the state 1 to the state 2 requires appropriate choice of the process parameters: the timing of the pump and Stokes pulses relative to each other and to the Stark pulse, the static detunings and the strengths of the peak Rabi frequencies and the peak Stark shift. The plots of adiabatic and diabatic energy curves in Fig. 4.3 correspond to the optimal process parameters and illustrate the population transfer from the state 1 to the state 2. Note that the timing of the pulses is somewhat counter-intuitive, i.e., the Stokes pulse precedes the pump pulse. It can be seen that the system starting

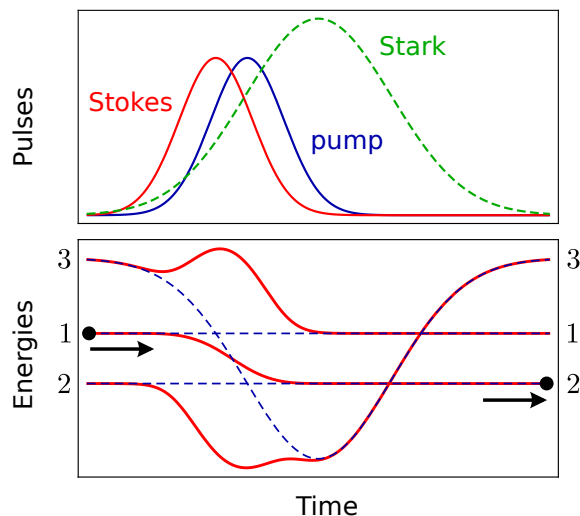


Figure 4.3: Top: Time dependencies of the pump (blue curve), Stokes (red curve) and the Stark (green curve) laser pulses. Bottom: Corresponding adiabatic (solid curves) and diabatic (dashed curves) energies versus time. System points on the energy curves are related to initial and final states. Arrows indicate the motion of the system points along adiabatic energy curves.

in the state 1 adiabatically follows the state $\Phi_1(t)$ and makes transition to the state 2. In the region where diabatic crossings 1 – 3 and 2 – 3 occur for the first time, the state $\Phi_1(t)$ has a small contribution of the excited state 3. However, the transient population of the state 3 is minimized by the counter-intuitive choice of pump and Stokes pulse timings [31].

In the next two sections SCRAP will be generalized to the case of two and three degenerate-level manifolds. The analysis of a degenerate-level system will be facilitated by its subdivision into a set of smaller independently evolving subsystems corresponding to the minimal-sized invariant subspaces of the Hamiltonian. As an illustration, the degenerate-level SCRAP formalism will be applied to the transitions in the ^{87}Rb atom.

4.2 SCRAP in a two-level atom

In this section the notation will be introduced and the stage set for a developed general formalism. Consider SCRAP population transfer among two atomic degenerate-level manifolds: ground g and final f , with corresponding energies E_g and E_f , respectively. Transition $g - f$ is driven by the classical field pump pulse, while strong off-resonant Stark field pulse introduces dynamic Stark detunings. Let $\mathcal{G} = \{|g_i\rangle | i = 1, \dots, n_g\}$ and $\mathcal{F} = \{|f_j\rangle | j = 1, \dots, n_f\}$ be the bases of Hilbert spaces for manifolds g and f , respectively, consisting of bare atomic states. The state $|\Psi(t)\rangle$ of the system is represented in basis $\mathcal{F} \cup \mathcal{G}$ by the vector $\mathbf{C}(t)$ that incorporates explicit phases taken from frequency of the pump pulse, ω_p . We are concerned with coherent excitation so we will describe the dynamics by the time-dependent Schrödinger equation. In the rotating-wave picture and using rotating wave approximation (RWA) we get the time-dependent Schrödinger equation for $\mathbf{C}(t)$,

$$i\hbar \frac{d}{dt} \mathbf{C}(t) = \mathbf{H}(t) \mathbf{C}(t). \quad (4.12)$$

Hamiltonian of the system is represented as

$$\mathbf{H}(t) = \hbar \begin{bmatrix} \Delta_f + \mathcal{S}(t) \mathbf{S}_f & \frac{1}{2} \Omega_p(t) \mathbf{V}^\dagger \\ \frac{1}{2} \Omega_p(t) \mathbf{V} & \mathcal{S}(t) \mathbf{S}_g \end{bmatrix} \quad (4.13)$$

where $\Omega_p(t)$ is the pump field Rabi frequency and \mathbf{V} is the matrix representation of the lowering operator that connects the states in manifold f to the states in manifold g . The n_f -dimensional diagonal matrix Δ_f describes the static detuning of the pump frequency from the Bohr frequency of the transition $g - f$ and can be represented as $\Delta_f = \Delta_f \mathbf{1}_{n_f}$, where $\mathbf{1}_{n_f}$ is n_f -dimensional unit matrix and $\Delta_f = (E_f - E_g)/\hbar - \omega_p$ is the common static detuning of all f states. The matrices \mathbf{S}_f and \mathbf{S}_g represent the Stark shift operators of the states in manifolds f and g , respectively. Their diagonal elements are proportional to the Stark shifts of the sublevels. All Stark shifts share the same time dependence, expressed by $\mathcal{S}(t)$, that arises from the laser Stark field variation in time. The quantity $\mathcal{S}(t)$ is proportional to the Stark pulse envelope and could be taken equal to the Stark shift of some chosen sublevel.

The structure of the RWA Hamiltonian of Eq. (4.13) is similar to that of the ordinary two-state SCRAP [13]. All time dependences are stored into $\Omega_p(t)$ and

$\mathcal{S}(t)$, but instead of single ground and final states we now have degenerate manifolds of substates, and hence we have matrices \mathbf{V} , \mathbf{S}_f , \mathbf{S}_g and $\mathbf{\Delta}_f$, instead of the single elements in ordinary two-state SCRAP case.

As an introduction to the general degenerate-level case, we examine the simplest case of equal sublevel Stark shifts

$$\mathbf{S}_f = s_f \mathbf{1}_{n_f}, \quad \mathbf{S}_g = s_g \mathbf{1}_{n_g}, \quad (4.14)$$

where s_f and s_g correspond to the common Stark shifts of the f and g substates, respectively. This will serve as a starting point for development of a degenerate-level formalism. The basic idea is to facilitate the analysis of a degenerate-level system by its subdivision into a set of smaller independently evolving subsystems. In the present case it is possible to find a suitable Morris-Shore (MS) transformation [36] of diabatic basis yielding a new adapted basis in which the dynamics of a coupled degenerate two-level system is reduced to a set of independently evolving non-degenerate two-state systems and a number of uncoupled (dark) states. It is easily seen that each two-state subsystem under SCRAP process evolves in a well-known manner [13, 31]. Consequently, the case of a SCRAP population transfer between two atomic degenerate-level manifolds having equal sublevel Stark shifts is simply reduced to a set of independent non-degenerate two-state subsystems and dark states. Let us restate the above consideration from a more general point of view. Effectively, the MS transformation yields the decomposition of the state space into a set of minimal-sized subspaces to which the evolution is restricted. These subspaces correspond to minimal-sized invariant subspaces (hereafter, invariant subspaces) of the Hamiltonian $\mathbf{H}(t)$. Hence, to each independent non-degenerate two-state system and to each dark state corresponds an invariant subspace of the Hamiltonian. Concept of invariant subspaces extends the scope of the former approach based on MS transformation. Namely, two-photon resonance condition expressed by equal sublevel shifts in Eq. (4.14) is essential for the existence of MS transformation. Generally, the Stark field removes the sublevel degeneracy by detuning the atomic sublevels from the two-photon resonance. The MS transformation does not exist in that case [36], but our concept of invariant subspaces is still applicable with likely altered size and number of subspaces. Therefore, the decomposition of the state space on the invariant subspaces is a generalization of MS transformation that is applicable in the general case of the removed sublevel degeneracy.

Analysis of a multilevel system is performed essentially by identifying the Hamiltonian invariant subspaces that depend substantially on couplings of the transitions and sublevel Stark shifts. Let $\mathcal{H}^{\text{inv}} = \mathcal{H}_f \oplus \mathcal{H}_g$ be such an invariant subspace formed by subspaces \mathcal{H}_f and \mathcal{H}_g corresponding to manifolds f and g , respectively. The defining condition $\mathbf{H}(t)\mathcal{H}^{\text{inv}} < \mathcal{H}^{\text{inv}}$ leads to the following requirements:

$$\Delta_f \mathcal{H}_f < \mathcal{H}_f, \quad \Delta_g \mathcal{H}_g < \mathcal{H}_g, \quad (4.15a)$$

$$\mathbf{S}_f \mathcal{H}_f < \mathcal{H}_f, \quad \mathbf{S}_g \mathcal{H}_g < \mathcal{H}_g, \quad (4.15b)$$

$$\mathbf{V} \mathcal{H}_f < \mathcal{H}_g, \quad \mathbf{V}^\dagger \mathcal{H}_g < \mathcal{H}_f. \quad (4.15c)$$

The conditions (4.15a) are trivially fulfilled and can be disregarded because the matrices Δ_f and Δ_g are constant multiples of appropriate unit matrices. Let $\mathcal{H}_g^d = \ker \mathbf{V}^\dagger$ be the subspace of states in manifold g that are dark to the transition $g \rightarrow f$, and let $\mathcal{H}_f^d = \ker \mathbf{V}$ be the subspace of states in manifold f that are dark to the transition $f \rightarrow g$. The conditions (4.15c) determine \mathcal{H}_f (\mathcal{H}_g) up to a direct sum with some dark subspace from \mathcal{H}_f^d (\mathcal{H}_g^d), and yield more gainful conditions

$$\mathbf{V}^\dagger \mathbf{V} \mathcal{H}_f < \mathcal{H}_f, \quad \mathbf{V} \mathbf{V}^\dagger \mathcal{H}_g < \mathcal{H}_g. \quad (4.16)$$

Refer briefly to the meaning of the operators involved in Eq. (4.16). Operator \mathbf{V} couples the states from \mathcal{H}_f to the states in $\mathbf{V} \mathcal{H}_f$ that belong to manifold g . On the other side, operator \mathbf{V}^\dagger couples the states from $\mathbf{V} \mathcal{H}_f$ to the states in manifold f belonging to the subspace $\mathbf{V}^\dagger \mathbf{V} \mathcal{H}_f$ that may include the states external to \mathcal{H}_f . If one has to find the subsystems that evolve independently then the condition $\mathbf{V}^\dagger \mathbf{V} \mathcal{H}_f < \mathcal{H}_f$ naturally emerges because the interaction with the pump field must not drive the states out from \mathcal{H}_f . Therefore, \mathcal{H}_f has to be invariant subspace of operator $\mathbf{V}^\dagger \mathbf{V}$, so that the evolution of the system is restricted within the subspace $\mathcal{H}_f \oplus \mathbf{V} \mathcal{H}_f$.

We are now ready to give an explicit construction of aforementioned invariant subspaces. Relations (4.15b) and (4.16) indicate that \mathcal{H}_f should be common invariant subspace for \mathbf{S}_f and $\mathbf{V}^\dagger \mathbf{V}$. Let $\mathcal{H}_{f,k}^{\text{inv}}$, $k \in \{1, \dots, n_f^{\text{inv}}\}$, be minimal-sized common invariant subspaces of $\mathbf{V}^\dagger \mathbf{V}$ and \mathbf{S}_f . It is easily seen that the subspace $\mathcal{H}_{g,k} := \mathbf{V} \mathcal{H}_{f,k}^{\text{inv}}$ is invariant for $\mathbf{V} \mathbf{V}^\dagger$, but need not to be invariant for \mathbf{S}_g due to the possibility that \mathbf{S}_g couples the states from distinct subspaces $\mathcal{H}_{g,k}$ together with some states from dark subspace \mathcal{H}_g^d . Therefore, invariant subspaces $\mathcal{H}_{g,\kappa}^{\text{inv}}$, common for both \mathbf{S}_g and

$\mathbf{V}\mathbf{V}^\dagger$, may be formed from several subspaces $\mathcal{H}_{g,k}$, $k \in I_\kappa$, accompanied with some subspace $\mathcal{H}_{g,\kappa}^d$ of \mathcal{H}_g^d , i.e., $\mathcal{H}_{g,\kappa}^{\text{inv}} := \bigoplus_{k \in I_\kappa} \mathcal{H}_{g,k} \oplus \mathcal{H}_{g,\kappa}^d$, $\kappa \in \{1, \dots, n_g^{\text{inv}}\}$. It is worth noting that the set I_κ , containing the indices that label the subspaces $\mathcal{H}_{g,k}$ interlinked by \mathbf{S}_g , may be empty in the case that the corresponding invariant subspace entirely resides within an appropriate dark space. Finally, $\mathcal{H}_\kappa^{\text{inv}} := \bigoplus_{k \in I_\kappa} \mathcal{H}_{f,k}^{\text{inv}} \oplus \mathcal{H}_{g,\kappa}^{\text{inv}}$ is invariant subspace for Hamiltonian $\mathbf{H}(t)$, including all subspaces $\mathcal{H}_{f,k}^{\text{inv}}$ that are connected with $\mathcal{H}_{g,\kappa}^{\text{inv}}$. The evolution during SCRAP process is restricted to $\mathcal{H}_\kappa^{\text{inv}}$. Two different types of the invariant subspaces need to be considered.

First, if $\mathcal{H}_\kappa^{\text{inv}}$ does not contain dark states from \mathcal{H}_g^d , it is possible to transfer all population from the subspace $\mathcal{H}_{g,\kappa}^{\text{inv}}$ into the subspace $\bigoplus_{k \in I_\kappa} \mathcal{H}_{f,k}^{\text{inv}}$, irrespective of the starting state. Namely, during SCRAP pulse sequence, all starting states in $\mathcal{H}_{g,\kappa}^{\text{inv}}$ are adiabatically connected to corresponding final states in $\bigoplus_{k \in I_\kappa} \mathcal{H}_{f,k}^{\text{inv}}$. This occurs because the evolution is decoupled from dark states that prohibit population transfer. The final states cannot be traced analytically unless related common invariant subspaces $\mathcal{H}_{g,\kappa}^{\text{inv}}$ and $\bigoplus_{k \in I_\kappa} \mathcal{H}_{f,k}^{\text{inv}}$ are one-dimensional, in which case there is one-to-one correspondence between starting and final states. In other cases the final states can be found only numerically because they depend on the parameters of the SCRAP process.

The second case is when the dark states are present in $\mathcal{H}_{g,\kappa}^{\text{inv}}$ due to interaction with the Stark field. Because the dark states suppress transfer of population to final level, not all states from $\mathcal{H}_{g,\kappa}^{\text{inv}}$ have the corresponding final states in $\bigoplus_{k \in I_\kappa} \mathcal{H}_{f,k}^{\text{inv}}$. Generally, $\sum_{k \in I_\kappa} \dim \mathcal{H}_{g,k}$ states are adiabatically connected to final states in $\bigoplus_{k \in I_\kappa} \mathcal{H}_{f,k}^{\text{inv}}$ enabling the population transfer, while $\dim \mathcal{H}_{g,\kappa}^d$ states do not contribute to the population transfer and preserve the population within ground level. In order to obtain the complete population transfer, it is necessary to prepare the initial state into specific coherent superpositions. Subspaces corresponding to each of the two groups of superpositions cannot be determined without knowing the parameters of the SCRAP process, apart from the trivial case $\mathcal{H}_{g,\kappa}^{\text{inv}} = \mathcal{H}_{g,\kappa}^d$. In the following subsection we give an illustrative example.

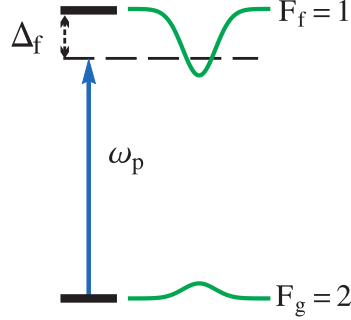


Figure 4.4: Atomic hyperfine level diagrams for two-level SCRAP. Solid curves schematically represent atomic dynamic level detuning induced by the Stark laser pulse. ω_p is the carrier frequency of the pump laser field. Δ_f is static level detuning.

4.2.1 SCRAP among two hyperfine levels in ^{87}Rb

Here we apply the above formalism to the SCRAP between two hyperfine levels $5S_{1/2}$, $F_g = 2$ and $5P_{1/2}$, $F_f = 1$ of ^{87}Rb that are coupled by classical field (see Fig. 4.4) with corresponding atomic lowering operator given by

$$\hat{V} = \hat{\mathbf{V}} \cdot \hat{\epsilon}_L \quad (4.17)$$

where $\hat{\epsilon}_L$ is the polarization of the light field. The vector operator $\hat{\mathbf{V}}$ is defined by

$$\begin{aligned} \hat{\mathbf{V}} = & (-1)^{F_f+J_g+I+1} \sqrt{(2F_f+1)(2J_g+1)} \begin{Bmatrix} J_f & J_g & 1 \\ F_g & F_f & I \end{Bmatrix} \\ & \times \sum_{q=-1}^1 \sum_{m_g, m_f} \langle F_g, m_g | F_f, m_f; 1, q \rangle |F_g, m_g\rangle \langle F_f, m_f | \mathbf{e}_q^*, \end{aligned} \quad (4.18)$$

where $I = 3/2$ is the nuclear quantum number of ^{87}Rb , $\{\cdot\cdot\cdot\}$ is Wigner $6j$ -symbol and $\langle F_g, m_g | F_f, m_f; 1, q \rangle$ is the Clebsch-Gordan coefficient that connects the final level state $|F_f, m_f\rangle$ to the ground level state $|F_g, m_g\rangle$ via polarization \mathbf{e}_q^* ,

$$\mathbf{e}_{\pm 1} = \mp \frac{1}{\sqrt{2}} (\mathbf{e}_x \pm i\mathbf{e}_y), \quad \mathbf{e}_0 = \mathbf{e}_z, \quad (4.19)$$

given in some orthonormal basis of polarization vectors. We choose the coordinate system such that the field propagates along the z axis, and define a basis of Zeeman states relative to this quantization axis. Bases of Hilbert spaces for level manifolds

f and g are

$$\mathcal{F} = \{|1, -1\rangle_f, |1, 0\rangle_f, |1, 1\rangle_f\}, \quad (4.20a)$$

$$\mathcal{G} = \{|2, -2\rangle_g, |2, -1\rangle_g, |2, 0\rangle_g, |2, 1\rangle_g, |2, 2\rangle_g\}. \quad (4.20b)$$

Generally, depending on the Stark field polarization, Stark shifts of magnetic hyperfine sublevels have scalar, vector, and tensor part, having none, linear, and quadratic dependence on magnetic quantum number m_F , respectively. Hence, Stark field can remove the degeneracy of hyperfine levels through the linear and quadratic dependence of shift on m_F . In this example we assume that the Stark field is linearly polarized so that the linear dependence vanishes. Alkali ground hyperfine sublevels gain the shift that does not have tensor part, so the degeneracy of ground sublevels is preserved. Excited hyperfine sublevels gain both scalar and tensor shifts. We will assume that pump frequency is chosen such that $\Delta_f > 0$, and that the Stark field frequency is such that the Stark shifts of the f (g) sublevels are negative (positive) (see Fig. 4.4). Off-diagonal elements of the Stark shift operators will be neglected for simplicity. In that manner we have the following structure of Stark shifts:

$$\mathbf{S}_g = s_g \text{diag}\{\underbrace{1, \dots, 1}_{2F_g+1}\}, \quad (4.21a)$$

$$\mathbf{S}_f = \text{diag}\{-(1 + s_f m_f^2 / F_f^2) \mid m_f = -F_f, \dots, F_f\}, \quad (4.21b)$$

where s_g and s_f are constants arbitrarily chosen in this example. $\mathcal{S}(t)$ is chosen equal to the absolute value of the Stark shift of the final sublevel $|1, 0\rangle_f$. For numerical calculations we will use Gaussian shapes for the laser pulses, yielding

$$\Omega_p(t) = \Omega_0 \exp\left(-\frac{(t - \tau_p)^2}{T_p^2}\right), \quad (4.22a)$$

$$\mathcal{S}(t) = S_0 \exp\left(-\frac{t^2}{T^2}\right). \quad (4.22b)$$

The Stark pulse center defines the time $t = 0$. Relative to this, the peak of the pump pulse is at time τ_p , chosen to correspond to the first intersection of diabatic energies of ground level and final sublevel $|1, 0\rangle_f$. We will use T_p as the unit of time and $1/T_p$ as the unit of frequency. We assume that the Stark pulse has duration $T = 2T_p$. The polarization of the pump field is chosen to be linear along x axis, so the matrix representing the lowering operator is

$$\mathbf{V} = \begin{bmatrix} \frac{1}{2} & 0 & 0 \\ 0 & \frac{1}{\sqrt{8}} & 0 \\ -\frac{1}{\sqrt{24}} & 0 & \frac{1}{\sqrt{24}} \\ 0 & -\frac{1}{\sqrt{8}} & 0 \\ 0 & 0 & -\frac{1}{2} \end{bmatrix}. \quad (4.23)$$

Ground level dark subspace determined as kernel of \mathbf{V}^\dagger is

$$\mathcal{H}_g^d = \text{span}\left\{\frac{1}{\sqrt{2}}|2, -1\rangle_g + \frac{1}{\sqrt{2}}|2, 1\rangle_g, \frac{1}{\sqrt{8}}|2, -2\rangle_g + \frac{\sqrt{3}}{2}|2, 0\rangle_g + \frac{1}{\sqrt{8}}|2, 2\rangle_g\right\}. \quad (4.24)$$

There are three common invariant subspaces of $\mathbf{V}^\dagger\mathbf{V}$ and \mathbf{S}_f

$$\mathcal{H}_{f,1}^{\text{inv}} = \text{span}\left\{\frac{1}{\sqrt{2}}|1, -1\rangle_f - \frac{1}{\sqrt{2}}|1, 1\rangle_f\right\}, \quad (4.25a)$$

$$\mathcal{H}_{f,2}^{\text{inv}} = \text{span}\left\{\frac{1}{\sqrt{2}}|1, -1\rangle_f + \frac{1}{\sqrt{2}}|1, 1\rangle_f\right\}, \quad (4.25b)$$

$$\mathcal{H}_{f,3}^{\text{inv}} = \text{span}\{|1, 0\rangle_f\}, \quad (4.25c)$$

and five common invariant subspaces of $\mathbf{V}\mathbf{V}^\dagger$ and \mathbf{S}_g

$$\mathcal{H}_{g,1}^{\text{inv}} = \text{span}\left\{\sqrt{\frac{3}{8}}|2, -2\rangle_g - \frac{1}{2}|2, 0\rangle_g + \sqrt{\frac{3}{8}}|2, 2\rangle_g\right\}, \quad (4.26a)$$

$$\mathcal{H}_{g,2}^{\text{inv}} = \text{span}\left\{\frac{1}{\sqrt{2}}|2, -2\rangle_g - \frac{1}{\sqrt{2}}|2, 2\rangle_g\right\}, \quad (4.26b)$$

$$\mathcal{H}_{g,3}^{\text{inv}} = \text{span}\left\{\frac{1}{\sqrt{2}}|2, -1\rangle_g - \frac{1}{\sqrt{2}}|2, 1\rangle_g\right\}, \quad (4.26c)$$

$$\mathcal{H}_{g,4}^{\text{inv}} = \text{span}\left\{\frac{1}{\sqrt{8}}|2, -2\rangle_g + \frac{\sqrt{3}}{2}|2, 0\rangle_g + \frac{1}{\sqrt{8}}|2, 2\rangle_g\right\}, \quad (4.26d)$$

$$\mathcal{H}_{g,5}^{\text{inv}} = \text{span}\left\{\frac{1}{\sqrt{2}}|2, -1\rangle_g + \frac{1}{\sqrt{2}}|2, 1\rangle_g\right\}. \quad (4.26e)$$

Note that $\mathcal{H}_{g,4}^{\text{inv}}$ and $\mathcal{H}_{g,5}^{\text{inv}}$ are dark subspaces of \mathcal{H}_g^d . Combining results (4.25) and (4.26) we get five invariant subspaces to which the evolution is restricted

$$\mathcal{H}_1^{\text{inv}} = \text{span}\left\{\frac{1}{\sqrt{2}}|1, -1\rangle_f - \frac{1}{\sqrt{2}}|1, 1\rangle_f, \sqrt{\frac{3}{8}}|2, -2\rangle_g - \frac{1}{2}|2, 0\rangle_g + \sqrt{\frac{3}{8}}|2, 2\rangle_g\right\}, \quad (4.27a)$$

$$\mathcal{H}_2^{\text{inv}} = \text{span}\left\{\frac{1}{\sqrt{2}}|1, -1\rangle_f + \frac{1}{\sqrt{2}}|1, 1\rangle_f, \frac{1}{\sqrt{2}}|2, -2\rangle_g - \frac{1}{\sqrt{2}}|2, 2\rangle_g\right\}, \quad (4.27b)$$

$$\mathcal{H}_3^{\text{inv}} = \text{span}\left\{|1, 0\rangle_f, \frac{1}{\sqrt{2}}|2, -1\rangle_g - \frac{1}{\sqrt{2}}|2, 1\rangle_g\right\}, \quad (4.27c)$$

$$\mathcal{H}_4^{\text{inv}} = \text{span}\left\{\frac{1}{\sqrt{8}}|2, -2\rangle_g + \frac{\sqrt{3}}{2}|2, 0\rangle_g + \frac{1}{\sqrt{8}}|2, 2\rangle_g\right\}, \quad (4.27d)$$

$$\mathcal{H}_5^{\text{inv}} = \text{span}\left\{\frac{1}{\sqrt{2}}|2, -1\rangle_g + \frac{1}{\sqrt{2}}|2, 1\rangle_g\right\}. \quad (4.27e)$$

Subspaces $\mathcal{H}_\kappa^{\text{inv}}$, $\kappa \in \{1, 2, 3\}$, do not contain dark states, thus it is possible to transfer all of the population from $\mathcal{H}_{g,\kappa}^{\text{inv}}$ to $\mathcal{H}_{f,\kappa}^{\text{inv}}$ for $\kappa \in \{1, 2, 3\}$. It is worth noting that the complete population transfer requires the starting states to be particular coherent superpositions. Contrary, population remains trapped within dark subspaces $\mathcal{H}_{g,4}^{\text{inv}}$ and $\mathcal{H}_{g,5}^{\text{inv}}$. Previous conclusions can be depicted by plotting the adiabatic energies corresponding to aforementioned invariant subspaces. Figure 4.5 shows time dependence of the pump and Stark pulse envelopes (left topmost part) and adiabatic and diabatic energies versus time (other parts). Two plots of energies (left column, from top to bottom) correspond to invariant subspaces $\mathcal{H}_\kappa^{\text{inv}}$, $\kappa \in \{1, 2\}$, while the right topmost part corresponds to invariant subspace $\mathcal{H}_3^{\text{inv}}$. It can be seen that starting from appropriate ground state, all the population transfers into the related final state. Note that the application of SCRAP for the complete population transfer requires the preparation of the initial state into the specific coherent superpositions of magnetic ground hyperfine substates. The opposite situation is shown in the two lower right-column plots where the population rests within ground level subspaces $\mathcal{H}_{g,4}^{\text{inv}}$ and $\mathcal{H}_{g,5}^{\text{inv}}$, respectively.

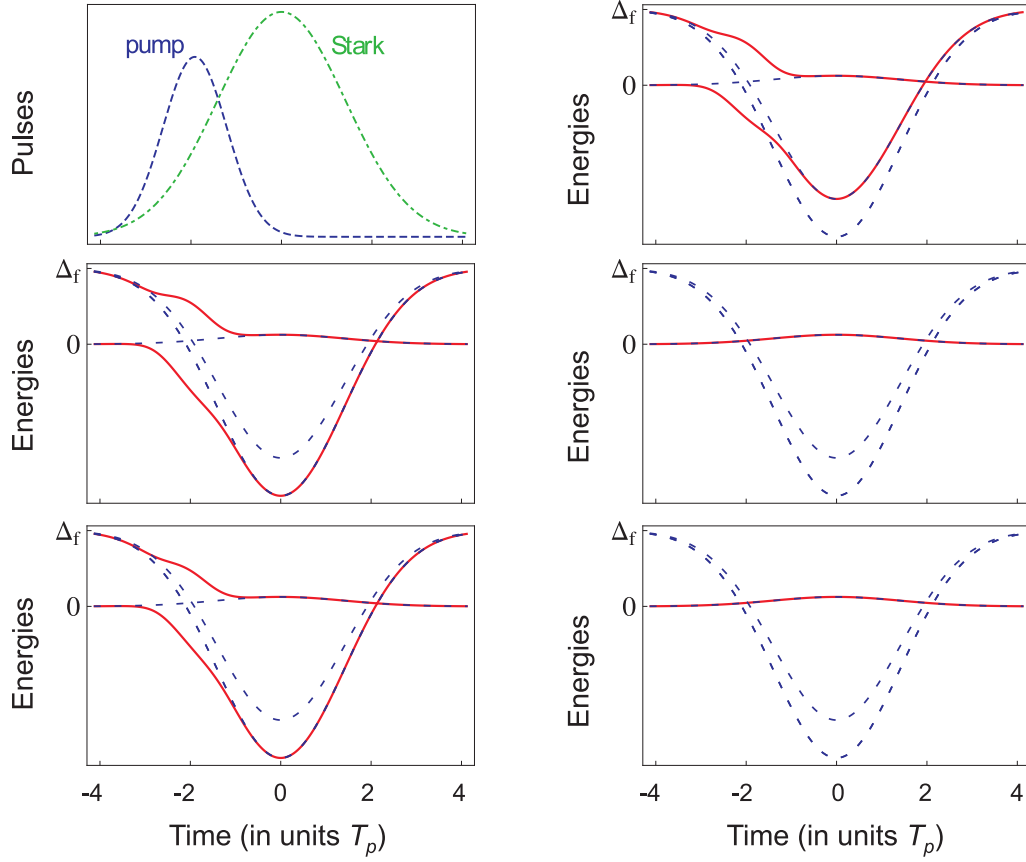


Figure 4.5: SCRAP among two hyperfine levels $5S_{1/2}, F_g = 2$ and $5P_{1/2}, F_f = 1$ in ^{87}Rb . Top-left: Time dependence of the pump and Stark pulse envelopes (arbitrary scaled). Other: Adiabatic (solid lines) and diabatic (dashed lines) energies versus time, related to the invariant subspaces $\mathcal{H}_\kappa^{\text{inv}}$, $\kappa = 1 - 2$ (left column) and $\kappa = 3 - 5$ (right column). The dashed line starting from energy 0 corresponds to degenerate g states. The two dashed lines originating from Δ_f correspond to the states $|1, 0\rangle_f$ (smaller shift) and $|1, \pm 1\rangle_f$ (larger shift). Used parameters are $\Delta_f = 200/T_p$, $S_0 = 500/T_p$, $\Omega_0 = 4/5 S_0$, $s_g = 1/20$, $s_f = 1/5$.

4.3 SCRAP in a three-level atom

We now analyze the SCRAP process between three atomic degenerate-level manifolds: ground g , excited e , and final f , with corresponding energies E_g , E_e , and E_f , respectively. The transitions $g - e$ and $f - e$ are driven by classical field pump and Stokes pulses, respectively. Strong off-resonant Stark field pulse is used to introduce dynamic Stark detunings. Similar to the section 4.2, let $\mathcal{G} = \{|g_i\rangle | i = 1, \dots, n_g\}$, $\mathcal{F} = \{|f_j\rangle | j = 1, \dots, n_f\}$, and $\mathcal{E} = \{|e_k\rangle | k = 1, \dots, n_e\}$, denote the bases of Hilbert spaces for manifolds g , f , and e , respectively, consisting of bare atomic states. In the same manner, the state $|\Psi(t)\rangle$ of the system is now represented in basis $\mathcal{E} \cup \mathcal{G} \cup \mathcal{F}$ by the vector $\mathbf{C}(t)$ incorporating explicit phases taken from frequency of the pump and Stokes pulses, ω_p and ω_S . In the rotating-wave picture and using RWA we get the time-dependent Schrödinger equation analog to Eq. (4.12). Matrix representation $\mathbf{H}(t)$ of the system Hamiltonian has the form

$$\mathbf{H}(t) = \hbar \begin{bmatrix} \Delta_e + \mathcal{S}(t)\mathbf{S}_e & \frac{1}{2}\Omega_p(t)\mathbf{V}_g^\dagger & \frac{1}{2}\Omega_S(t)\mathbf{V}_f^\dagger \\ \frac{1}{2}\Omega_p(t)\mathbf{V}_g & \mathcal{S}(t)\mathbf{S}_g & \mathbf{0} \\ \frac{1}{2}\Omega_S(t)\mathbf{V}_f & \mathbf{0} & \Delta_f + \mathcal{S}(t)\mathbf{S}_f \end{bmatrix}, \quad (4.28)$$

where $\Omega_p(t)$ and $\Omega_S(t)$ are Rabi frequencies of the pump and Stokes field, respectively, and \mathbf{V}_g (\mathbf{V}_f) is the matrix representing the lowering operator that connects the states in manifold e to the states in manifold g (f). The zeros $\mathbf{0}$ denote null rectangular matrices of appropriate dimensions. The diagonal matrices Δ_e and Δ_f describe static detunings and can be represented as $\Delta_e = \Delta_e \mathbf{1}_{n_e}$ and $\Delta_f = \Delta_f \mathbf{1}_{n_f}$, where common static detunings Δ_e and Δ_f for one-photon transitions are given by

$$\Delta_e = (E_e - E_g)/\hbar - \omega_p, \quad (4.29a)$$

$$\Delta_f = (E_f - E_g)/\hbar + \omega_S - \omega_p. \quad (4.29b)$$

The matrices \mathbf{S}_e , \mathbf{S}_g and \mathbf{S}_f correspond to the Stark shift operators of the states in manifolds e , g and f , respectively. Again, the quantity $\mathcal{S}(t)$ is proportional to the Stark pulse envelope and is chosen to introduce a referent Stark shift. The structure of the RWA Hamiltonian of Eq. (4.28) is similar to that of the conventional three-state SCRAP with single elements replaced by the matrices [31].

As in the section 4.2, we first inspect the case when Stark shifts of the sublevels

are equal

$$\mathbf{S}_e = s_e \mathbf{1}_{n_e}, \quad \mathbf{S}_g = s_g \mathbf{1}_{n_g}, \quad \mathbf{S}_f = s_f \mathbf{1}_{n_f}, \quad (4.30)$$

where s_e , s_g and s_f correspond to the common Stark shifts of the e , g , and f states, respectively. Again, we can utilize three-level MS transformation [37] to obtain sets of independently evolving non-degenerate three-state and two-state systems and a set of uncoupled (dark) states, provided the following condition is fulfilled

$$[\mathbf{V}_g^\dagger \mathbf{V}_g, \mathbf{V}_f^\dagger \mathbf{V}_f] = 0. \quad (4.31)$$

To each such independently evolving non-degenerate system corresponds an invariant subspace of the Hamiltonian, as is already mentioned in Sec. 4.2. The origin of operators involved in Eq. (4.31) has been addressed above, and we will briefly discuss the commutation condition. Consider some subspace \mathcal{H}_e of states in manifold e . Following the discussion in Sec. 4.2, if one has to find the subsystems that are dynamically independent, then \mathcal{H}_e has to be common invariant subspace of operators $\mathbf{V}_g^\dagger \mathbf{V}_g$ and $\mathbf{V}_f^\dagger \mathbf{V}_f$, so that the evolution of the system is restricted to the subspace $\mathcal{H}_e \oplus \mathbf{V}_g \mathcal{H}_e \oplus \mathbf{V}_f \mathcal{H}_e$. The condition (4.31) assures that all minimal-sized common invariant subspaces are one-dimensional, i.e., that the corresponding three-state and two-state systems are non-degenerate. We note that two-state subsystems arise when one of subspaces $\mathbf{V}_g \mathcal{H}_e$ or $\mathbf{V}_f \mathcal{H}_e$ contains only null vector, i.e., when the states from \mathcal{H}_e are dark to one of transitions $e \rightarrow g$ or $e \rightarrow f$. Conditions (4.30) and (4.31) that are essential for the MS transformation only affect the size and number of independently evolving invariant subspaces. Therefore, as in the two-level SCRAP case, the decomposition of the state space on the invariant subspaces generalizes MS transformation.

Let $\mathcal{H}^{\text{inv}} = \mathcal{H}_e \oplus \mathcal{H}_g \oplus \mathcal{H}_f$ be an invariant subspace for the Hamiltonian. The necessary condition $\mathbf{H}(t)\mathcal{H}^{\text{inv}} \subset \mathcal{H}^{\text{inv}}$ yields the following requirements:

$$\Delta_e \mathcal{H}_e \subset \mathcal{H}_e, \quad \Delta_g \mathcal{H}_g \subset \mathcal{H}_g, \quad \Delta_f \mathcal{H}_f \subset \mathcal{H}_f, \quad (4.32a)$$

$$\mathbf{S}_e \mathcal{H}_e \subset \mathcal{H}_e, \quad \mathbf{S}_g \mathcal{H}_g \subset \mathcal{H}_g, \quad \mathbf{S}_f \mathcal{H}_f \subset \mathcal{H}_f, \quad (4.32b)$$

$$\mathbf{V}_g^\dagger \mathcal{H}_g \subset \mathcal{H}_e, \quad \mathbf{V}_f^\dagger \mathcal{H}_f \subset \mathcal{H}_e, \quad (4.32c)$$

$$\mathbf{V}_g \mathcal{H}_e \subset \mathcal{H}_g, \quad \mathbf{V}_f \mathcal{H}_e \subset \mathcal{H}_f. \quad (4.32d)$$

The conditions (4.32a) can be disregarded as trivially fulfilled. Let $\mathcal{H}_{ge}^d = \ker \mathbf{V}_g^\dagger$

($\mathcal{H}_{fe}^d = \ker \mathbf{V}_f^\dagger$) be the subspace of states in manifold g (f) that are dark to the transition $g \rightarrow e$ ($f \rightarrow e$), and let $\mathcal{H}_{ef}^d = \ker \mathbf{V}_f$ be the subspace of states in manifold e that are dark to the transition $e \rightarrow f$. The conditions (4.32c) determine \mathcal{H}_g (\mathcal{H}_f) up to a direct sum with some dark subspace of \mathcal{H}_{ge}^d (\mathcal{H}_{fe}^d), and together with Eq. (4.32d) yield more useful conditions

$$\mathbf{V}_g^\dagger \mathbf{V}_g \mathcal{H}_e < \mathcal{H}_e, \quad \mathbf{V}_f^\dagger \mathbf{V}_f \mathcal{H}_e < \mathcal{H}_e, \quad (4.33a)$$

$$\mathbf{V}_g \mathbf{V}_g^\dagger \mathcal{H}_g < \mathcal{H}_g, \quad \mathbf{V}_f \mathbf{V}_f^\dagger \mathcal{H}_f < \mathcal{H}_f. \quad (4.33b)$$

Let $\mathcal{H}_{e,k}^{\text{inv}}$, $k \in \{1, \dots, n_e^{\text{inv}}\}$, be common invariant subspaces of $\mathbf{V}_g^\dagger \mathbf{V}_g$, $\mathbf{V}_f^\dagger \mathbf{V}_f$ and \mathbf{S}_e . It is trivial to see that the subspace $\mathcal{H}_{g,k} := \mathbf{V}_g \mathcal{H}_{e,k}^{\text{inv}}$ ($\mathcal{H}_{f,k} := \mathbf{V}_f \mathcal{H}_{e,k}^{\text{inv}}$) is invariant for $\mathbf{V}_g \mathbf{V}_g^\dagger$ ($\mathbf{V}_f \mathbf{V}_f^\dagger$), but need not to be invariant for \mathbf{S}_g (\mathbf{S}_f) due to the possibility that it links the states from different subspaces $\mathcal{H}_{g,k}$ ($\mathcal{H}_{f,k}$) together with some states from dark subspace \mathcal{H}_{ge}^d (\mathcal{H}_{fe}^d). Hence, invariant subspaces $\mathcal{H}_{g,\kappa'}^{\text{inv}}$, common for both \mathbf{S}_g and $\mathbf{V}_g \mathbf{V}_g^\dagger$ and connected with some of the subspaces $\mathcal{H}_{e,k}^{\text{inv}}$, may be formed from several subspaces $\mathcal{H}_{g,k}$ accompanied with some subspace $\mathcal{H}_{ge,\kappa'}^d$ of dark space \mathcal{H}_{ge}^d , i.e., $\mathcal{H}_{g,\kappa'}^{\text{inv}} := \bigoplus_{k \in I_{g,\kappa'}} \mathcal{H}_{g,k} \oplus \mathcal{H}_{ge,\kappa'}^d$, $\kappa' \in \{1, \dots, n_g^{\text{inv}}\}$, where the set $I_{g,\kappa'}$ contains the indices k labeling the subspaces $\mathcal{H}_{g,k}$ that are interconnected by \mathbf{S}_g . Analogously, $\mathcal{H}_{f,\kappa''}^{\text{inv}} := \bigoplus_{k \in I_{f,\kappa''}} \mathcal{H}_{f,k} \oplus \mathcal{H}_{fe,\kappa''}^d$, $\kappa'' \in \{1, \dots, n_f^{\text{inv}}\}$. The sets of indices $I_{g,\kappa'}$ may be empty in case that related invariant subspace entirely belongs to the appropriate dark subspace. Some of the nonempty sets $I_{g,\kappa'}$ may have a nonempty intersection with exactly one corresponding set $I_{f,\kappa''}$, because for at least one $k \in I_{g,\kappa'} \cap I_{f,\kappa''}$ the relations $\mathbf{V}_g \mathcal{H}_{e,k}^{\text{inv}} < \mathcal{H}_{ge,\kappa'}^d$ and $\mathbf{V}_f \mathcal{H}_{e,k}^{\text{inv}} < \mathcal{H}_{fe,\kappa''}^d$ may hold. Such subspaces $\mathcal{H}_{g,\kappa'}^{\text{inv}}$ and $\mathcal{H}_{f,\kappa''}^{\text{inv}}$ are then dynamically connected via the excited level subspace $\mathcal{H}_{e,k}^{\text{inv}}$ and the invariant subspace for Hamiltonian is composed as $\mathcal{H}_{\kappa}^{\text{inv}} := \bigoplus_{k \in I_{g,\kappa'} \cup I_{f,\kappa''}} \mathcal{H}_{e,k}^{\text{inv}} \oplus \mathcal{H}_{g,\kappa'}^{\text{inv}} \oplus \mathcal{H}_{f,\kappa''}^{\text{inv}}$ including all subspaces $\mathcal{H}_{e,k}^{\text{inv}}$ that are connected with $\mathcal{H}_{g,\kappa'}^{\text{inv}}$ and $\mathcal{H}_{f,\kappa''}^{\text{inv}}$. If some of the nonempty sets $I_{g,\kappa'}$ does not have a nonempty intersection with any of the sets $I_{f,\kappa''}$, then the invariant subspace is constructed solely from subspaces related to g and e manifolds, i.e., $\mathcal{H}_{\kappa}^{\text{inv}} := \bigoplus_{k \in I_{g,\kappa}} \mathcal{H}_{e,k}^{\text{inv}} \oplus \mathcal{H}_{g,\kappa}^{\text{inv}}$. That occurs if $\bigoplus_{k \in I_{g,\kappa}} \mathcal{H}_{e,k}^{\text{inv}} < \mathcal{H}_{ge,\kappa}^d$. Similar situation may involve final end excited level resulting in $\mathcal{H}_{\kappa}^{\text{inv}} := \bigoplus_{k \in I_{f,\kappa}} \mathcal{H}_{e,k}^{\text{inv}} \oplus \mathcal{H}_{f,\kappa}^{\text{inv}}$. Distinct types of the invariant subspaces depending of the presence of dark states need to be examined.

First, if $\mathcal{H}_{\kappa}^{\text{inv}}$ does not contain any dark state from \mathcal{H}_{ge}^d nor from \mathcal{H}_{ef}^d , it is possible to transfer all the population from $\mathcal{H}_{g,\kappa'}^{\text{inv}}$ into $\mathcal{H}_{f,\kappa''}^{\text{inv}}$, irrespective of the starting state. All ground starting states from the subspace $\mathcal{H}_{g,\kappa'}^{\text{inv}}$ are adiabatically connected

to the related ending states in the subspace $\mathcal{H}_{f,\kappa''}^{\text{inv}}$ enabling the complete population transfer. Exact ending states cannot be known in advance, unless the aforementioned invariant subspaces are one-dimensional. In such case there is one-to-one correspondence between the states at the beginning of the SCRAP process to the appropriate states at the end. In all other cases the ending states can be determined only numerically because of their dependence on the particular parameters of the SCRAP process.

The situation changes when the dark states are present in $\mathcal{H}_{\kappa}^{\text{inv}}$. The states from \mathcal{H}_{ge}^d prevent population transfer from the level g to the level e , while the states from \mathcal{H}_{ef}^d obstruct transfer of population from the level e toward the level f . Due to the presence of dark states from \mathcal{H}_{ge}^d (or \mathcal{H}_{fe}^d), part of the starting population remains trapped within these states. If a number of dark states from \mathcal{H}_{ef}^d are contained within appropriate excited level subspace of $\mathcal{H}_{\kappa}^{\text{inv}}$, there is the same number of ground starting states that are adiabatically connected to the states in the excited level subspace of $\mathcal{H}_{\kappa}^{\text{inv}}$. The rest of ground starting states are adiabatically connected to the ending states in the final level. Thus, it is required to prepare the starting state into specific coherent superpositions in order to perform the complete population transfer. Exact starting and ending superpositions cannot be found in advance, except in the case of one-dimensional adiabatically connected starting and ending subspaces. Otherwise, one must resort to numerics for particular choice of SCRAP parameters. In the next subsection we demonstrate previous considerations on the real atomic system.

4.3.1 SCRAP among three hyperfine levels in ^{87}Rb

As an example we will analyze SCRAP in ^{87}Rb from the ground hyperfine level $5S_{1/2}$, $F_g = 2$ to the final level $5S_{1/2}$, $F_f = 1$ via the excited level $5P_{1/2}$, $F_e = 1$. Transitions $g - e$ and $f - e$ are driven by classical fields (see Fig. 4.6), pump and Stokes respectively, with corresponding atomic lowering operators given by

$$\hat{V}_g = \hat{\mathbf{V}}_g \cdot \hat{\epsilon}_p, \quad \hat{V}_f = \hat{\mathbf{V}}_f \cdot \hat{\epsilon}_S, \quad (4.34)$$

where $\hat{\epsilon}_p$ and $\hat{\epsilon}_S$ are the polarizations of the pump and Stokes field, respectively. The vector operators $\hat{\mathbf{V}}_g$ and $\hat{\mathbf{V}}_f$ are defined in analogy with Eq. (4.18). We choose the coordinate system such that the fields propagate along the z axis, and define a

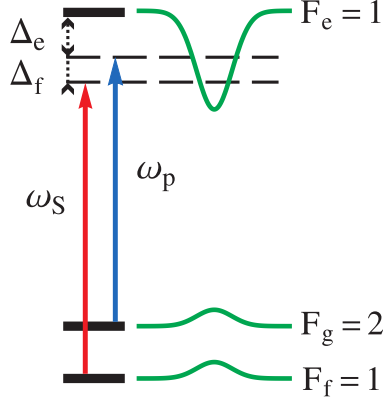


Figure 4.6: Atomic hyperfine level diagrams for three-level SCRAP. Solid curves schematically represent atomic dynamic level detuning induced by the Stark laser pulse. ω_p and ω_S are carrier frequencies of the pump and Stokes laser fields, respectively. $\Delta_{f(e)}$ are static level detunings.

basis of Zeeman states relative to this quantization axis. Bases of Hilbert spaces for manifolds e , g , and f are

$$\mathcal{E} = \{|1, -1\rangle_e, |1, 0\rangle_e, |1, 1\rangle_e\}, \quad (4.35a)$$

$$\mathcal{G} = \{|2, -2\rangle_g, |2, -1\rangle_g, |2, 0\rangle_g, |2, 1\rangle_g, |2, 2\rangle_g\}, \quad (4.35b)$$

$$\mathcal{F} = \{|1, -1\rangle_f, |1, 0\rangle_f, |1, 1\rangle_f\}. \quad (4.35c)$$

Similar to the section 4.2.1, we assume that the Stark field is linearly polarized, so the degeneracy of ground levels is preserved. Excited hyperfine sublevels gain both scalar and tensor shifts. To assure necessary conditions for adiabatic connection between ground and final level [31], we choose pump and Stokes frequencies such that $\Delta_f < 0$ and $\Delta_e > 0$, and take Stark field frequency so that the Stark shifts of the e (g and f) sublevels are negative (positive) (see Fig. 4.6). Off-diagonal elements of the Stark shift operators are again neglected for simplicity. Sublevel Stark shifts have the form

$$\mathbf{S}_g = s_g \text{diag}\{\underbrace{1, \dots, 1}_{2F_g+1}\}, \quad \mathbf{S}_f = s_f \text{diag}\{\underbrace{1, \dots, 1}_{2F_f+1}\}, \quad (4.36a)$$

$$\mathbf{S}_e = \text{diag}\{-(1 + s_e m_e^2 / F_e^2) \mid m_e = -F_e, \dots, F_e\}, \quad (4.36b)$$

where s_g , s_f and s_e are constants arbitrarily chosen in this example. $\mathcal{S}(t)$ is taken equal to the absolute value of the Stark shift of the excited sublevel $|1, 0\rangle_e$. For

numerical calculations we shall assume Gaussian shapes for all pulses, and take the pump and Stokes Rabi frequencies to have identical peak values Ω_0 , obtaining

$$\Omega_p(t) = \Omega_0 \exp\left(-\frac{(t - \tau_p)^2}{T_p^2}\right), \quad (4.37a)$$

$$\Omega_S(t) = \Omega_0 \exp\left(-\frac{(t - \tau_S)^2}{T_S^2}\right), \quad (4.37b)$$

$$\mathcal{S}(t) = S_0 \exp\left(-\frac{t^2}{T^2}\right). \quad (4.37c)$$

We will also take equal pump and Stokes durations, $T_p = T_S$ and $T = 2T_p$. Stark field peak value is taken large enough to assure necessary diabatic energy crossings. The timings τ_p and τ_S of pulses are chosen to correspond to appropriate first crossings of diabatic energies of ground and final level with diabatic energy of excited sublevel $|1, 0\rangle_e$, in the ‘‘counter-intuitive’’ order [31]. The polarizations of the pump and Stokes field are both chosen to be linear along x axis, so the matrices representing lowering operators are

$$\mathbf{V}_g = \begin{bmatrix} \frac{1}{2} & 0 & 0 \\ 0 & \frac{1}{\sqrt{8}} & 0 \\ \frac{1}{\sqrt{24}} & 0 & \frac{1}{\sqrt{24}} \\ 0 & \frac{1}{\sqrt{8}} & 0 \\ 0 & 0 & \frac{1}{2} \end{bmatrix}, \quad \mathbf{V}_f = \begin{bmatrix} 0 & -\frac{1}{\sqrt{24}} & 0 \\ \frac{1}{\sqrt{24}} & 0 & -\frac{1}{\sqrt{24}} \\ 0 & \frac{1}{\sqrt{24}} & 0 \end{bmatrix}, \quad (4.38)$$

Dark subspaces are the following:

$$\begin{aligned} \mathcal{H}_{ge}^d = \text{span}\{ & 1/\sqrt{2}|2, -1\rangle_g + 1/\sqrt{2}|2, 1\rangle_g, \\ & 1/\sqrt{8}|2, -2\rangle_g + \sqrt{3}/2|2, 0\rangle_g + 1/\sqrt{8}|2, 2\rangle_g\}, \end{aligned} \quad (4.39)$$

$$\mathcal{H}_{fe}^d = \text{span}\{1/\sqrt{2}|1, -1\rangle_f - 1/\sqrt{2}|1, 1\rangle_f\}, \quad (4.40)$$

$$\mathcal{H}_{ef}^d = \text{span}\{1/\sqrt{2}|1, -1\rangle_e - 1/\sqrt{2}|1, 1\rangle_e\}. \quad (4.41)$$

There are three common invariant subspaces for $\mathbf{V}_g^\dagger \mathbf{V}_g$, $\mathbf{V}_f^\dagger \mathbf{V}_f$ and \mathbf{S}_e

$$\mathcal{H}_{e,1}^{\text{inv}} = \text{span}\left\{\frac{1}{\sqrt{2}}|1, -1\rangle_e - \frac{1}{\sqrt{2}}|1, 1\rangle_e\right\}, \quad (4.42a)$$

$$\mathcal{H}_{e,2}^{\text{inv}} = \text{span}\left\{\frac{1}{\sqrt{2}}|1, -1\rangle_e + \frac{1}{\sqrt{2}}|1, 1\rangle_e\right\}, \quad (4.42b)$$

$$\mathcal{H}_{e,3}^{\text{inv}} = \text{span}\{|1, 0\rangle_e\}, \quad (4.42c)$$

five invariant subspaces for $\mathbf{V}_g \mathbf{V}_g^\dagger$ and \mathbf{S}_g

$$\mathcal{H}_{g,1}^{\text{inv}} = \text{span}\left\{\sqrt{\frac{3}{8}}|2, -2\rangle_g - \frac{1}{2}|2, 0\rangle_g + \sqrt{\frac{3}{8}}|2, 2\rangle_g\right\}, \quad (4.43a)$$

$$\mathcal{H}_{g,2}^{\text{inv}} = \text{span}\left\{\frac{1}{\sqrt{2}}|2, -2\rangle_g - \frac{1}{\sqrt{2}}|2, 2\rangle_g\right\}, \quad (4.43b)$$

$$\mathcal{H}_{g,3}^{\text{inv}} = \text{span}\left\{\frac{1}{\sqrt{2}}|2, -1\rangle_g - \frac{1}{\sqrt{2}}|2, 1\rangle_g\right\}, \quad (4.43c)$$

$$\mathcal{H}_{g,4}^{\text{inv}} = \text{span}\left\{\frac{1}{2\sqrt{2}}|2, -2\rangle_g + \frac{\sqrt{3}}{2}|2, 0\rangle_g + \frac{1}{2\sqrt{2}}|2, 2\rangle_g\right\}, \quad (4.43d)$$

$$\mathcal{H}_{g,5}^{\text{inv}} = \text{span}\left\{\frac{1}{\sqrt{2}}|2, -1\rangle_g + \frac{1}{\sqrt{2}}|2, 1\rangle_g\right\}, \quad (4.43e)$$

and three invariant subspaces for $\mathbf{V}_f \mathbf{V}_f^\dagger$ and \mathbf{S}_f

$$\mathcal{H}_{f,1}^{\text{inv}} = \text{span}\{|1, 0\rangle_f\}, \quad (4.44a)$$

$$\mathcal{H}_{f,2}^{\text{inv}} = \text{span}\left\{\frac{1}{\sqrt{2}}|1, -1\rangle_f + \frac{1}{\sqrt{2}}|1, 1\rangle_f\right\}, \quad (4.44b)$$

$$\mathcal{H}_{f,3}^{\text{inv}} = \text{span}\left\{\frac{1}{\sqrt{2}}|1, -1\rangle_f - \frac{1}{\sqrt{2}}|1, 1\rangle_f\right\}. \quad (4.44c)$$

Six invariant subspaces of the Hamiltonian can be constructed using (4.42) – (4.44)

$$\mathcal{H}_1^{\text{inv}} = \text{span}\left\{\frac{1}{\sqrt{2}}|1, -1\rangle_e - \frac{1}{\sqrt{2}}|1, 1\rangle_e, \sqrt{\frac{3}{8}}|2, -2\rangle_g - \frac{1}{2}|2, 0\rangle_g + \sqrt{\frac{3}{8}}|2, 2\rangle_g\right\}, \quad (4.45a)$$

$$\mathcal{H}_2^{\text{inv}} = \text{span}\left\{\frac{1}{\sqrt{2}}|1, -1\rangle_e + \frac{1}{\sqrt{2}}|1, 1\rangle_e, \frac{1}{\sqrt{2}}|2, -2\rangle_g - \frac{1}{\sqrt{2}}|2, 2\rangle_g, |1, 0\rangle_f\right\}, \quad (4.45b)$$

$$\mathcal{H}_3^{\text{inv}} = \text{span}\left\{|1, 0\rangle_e, \frac{1}{\sqrt{2}}|2, -1\rangle_g - \frac{1}{\sqrt{2}}|2, 1\rangle_g, \frac{1}{\sqrt{2}}|1, -1\rangle_f + \frac{1}{\sqrt{2}}|1, 1\rangle_f\right\}, \quad (4.45c)$$

$$\mathcal{H}_4^{\text{inv}} = \text{span}\left\{\frac{1}{2\sqrt{2}}|2, -2\rangle_g + \frac{\sqrt{3}}{2}|2, 0\rangle_g + \frac{1}{2\sqrt{2}}|2, 2\rangle_g\right\}, \quad (4.45d)$$

$$\mathcal{H}_5^{\text{inv}} = \text{span}\left\{\frac{1}{\sqrt{2}}|2, -1\rangle_g + \frac{1}{\sqrt{2}}|2, 1\rangle_g\right\}, \quad (4.45e)$$

$$\mathcal{H}_6^{\text{inv}} = \text{span}\left\{\frac{1}{\sqrt{2}}|1, -1\rangle_f - \frac{1}{\sqrt{2}}|1, 1\rangle_f\right\}. \quad (4.45f)$$

Subspaces $\mathcal{H}_\kappa^{\text{inv}}$, $\kappa \in \{2, 3\}$, do not contain dark states, therefore it is possible to obtain complete population transfer from $\mathcal{H}_{g,\kappa'}^{\text{inv}}$ to $\mathcal{H}_{f,\kappa''}^{\text{inv}}$ for pairs $(\kappa', \kappa'') \in \{(2, 1), (3, 2)\}$. Note that the complete population transfer requires the starting states to be particular coherent superpositions. Conversely, the subspace $\mathcal{H}_1^{\text{inv}}$ con-

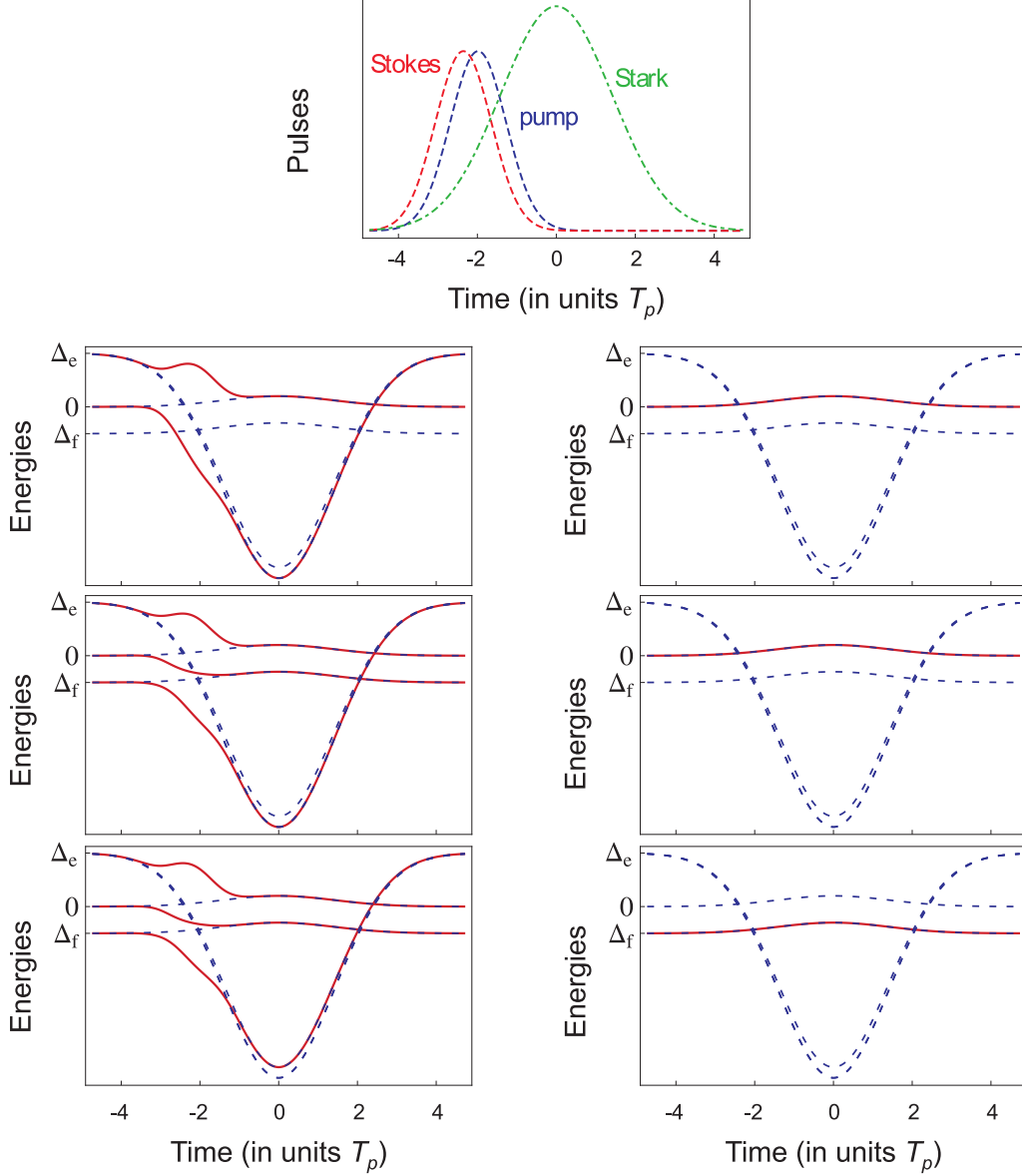


Figure 4.7: SCRAP in ^{87}Rb among hyperfine levels $5S_{1/2}, F_g = 2$ and $5S_{1/2}, F_f = 1$ via $5P_{1/2}, F_e = 1$. Topmost: Time dependence of the Stokes, pump and Stark pulse envelopes (arbitrary scaled). Other: Adiabatic (solid lines) and diabatic (dashed lines) energies versus time, related to the invariant subspaces $\mathcal{H}_\kappa^{\text{inv}}$, $\kappa = 1 - 3$ (left column, top to bottom) and $\kappa = 4 - 6$ (right column, top to bottom). The dashed line starting from energy 0 (Δ_f) corresponds to the degenerate g (f) states. The two dashed lines originating from Δ_e correspond to the states $|1, 0\rangle_e$ (smaller shift) and $|1, \pm 1\rangle_e$ (larger shift). Used parameters are $\Delta_e = 100/T_p$, $\Delta_f = -1/2\Delta_e$, $S_0 = 400/T_p$, $\Omega_0 = 4/5 S_0$, $s_g = s_f = 1/20$, $s_e = 1/20$.

tains the dark state from \mathcal{H}_{ef}^d , so that the population transfers exclusively to the excited level, not to the final. The subspaces $\mathcal{H}_4^{\text{inv}}$ and $\mathcal{H}_5^{\text{inv}}$ ($\mathcal{H}_6^{\text{inv}}$) are dark for transition from ground (final) to excited level and retain the initial population during the SCRAP process. Previous results can be illustrated by plotting the adiabatic energies corresponding to above-mentioned invariant subspaces. Figure 4.7 shows time dependence of the pump, Stokes and Stark pulse envelopes (topmost part) and adiabatic and diabatic energies versus time (lower parts). Topmost plot of energies in the left column is related to $\mathcal{H}_1^{\text{inv}}$ and shows that the population adiabatically transfers to the excited level. Second and third energy plots in the left column correspond to invariant subspaces $\mathcal{H}_\kappa^{\text{inv}}$, $\kappa \in \{2, 3\}$. It is obvious that starting from appropriate ground state, all the population transfers into the related final state. Similar to the two-level case in the section 4.2.1, the total population transfer requires that the initial ground state is prepared into the specific coherent superpositions. Different situation is shown in the three right-column plots where the population rests within ground (final) level subspaces $\mathcal{H}_{g,4}^{\text{inv}}$ and $\mathcal{H}_{g,5}^{\text{inv}}$ ($\mathcal{H}_{f,3}^{\text{inv}}$), respectively.

5. Conclusion

Alkali-metal vapors represent suitable media for studying various coherent effects emerging from laser-atom interaction, e.g. EIT, EIA and SCRAP. In vacuum cells containing alkali-metal vapor at low pressures, mean free path of the atoms is larger than the cell dimensions. If an atom freely traverses the laser beam, its state will continuously evolve. The unperturbed laser-atom interaction during the atomic passage through the laser beam in vacuum cells enables the examination of a development of the coherent effects. Different atomic states in various parts of the laser beam will yield different coherent resonances obtained from these beam parts. In general, coherent effects depend in a nonlinear way on the laser light intensity. Transient atomic evolution will be essentially determined by the intensity profile of the laser beam. Distinct physical processes can dominate the atomic evolution and affect line shapes of the coherent resonances depending on the laser beam profile. In this thesis coherent effects were studied for two laser beam profiles: Gaussian and uniform intensity Π profile. Gaussian profile is commonly used in experiments, while Π profile is usually assumed in theoretical treatments.

Examination of Hanle EIT resonances obtained from selected parts of the cross-section of the Gaussian laser beam is performed. The open transition $F_g = 2 \rightarrow F_e = 1$ of ^{87}Rb D_1 line is used. The line shapes, widths and contrasts of the EIT resonances strongly depend on the radial position of the sampled area of the laser beam. The resonances originating from the central parts are different than those obtained from the wings of the Gaussian laser beam. In the latter case the resonances are much narrower with two sideband transmission minima. The theoretical model reproduces the experimental EIT resonances and explains the obtained EIT line shapes by the Ramsey-like interference between the atoms coherently prepared in the central parts of the Gaussian beam with the laser light in the wings of the beam. The interference features are partially masked due to simultaneous contribution from atoms coming from the outside of the laser beam.

The Ramsey-like interference together with lower power broadening leads to the narrowing of the Hanle EIT resonances in the wings of the Gaussian laser beam. The EIT line narrowing at larger distances from the beam axis becomes more prominent as the total laser intensity increases. This kind of investigation revealed for the first time that Ramsey-like interference can occur within a single laser beam. In addition, it pointed out that the choice of the detected laser beam part is important and can yield diverse results.

The evolution of atomic states in constant intensity laser field is investigated using Π -shaped laser beam resonant to the aforementioned open transition of ^{87}Rb . The Π laser intensity profile allows the studies to be unaffected by intensity variations of the laser electric field. Information about the transient evolution of the atomic state during the interaction with the laser beam was obtained by detailed inspection of features in line shapes of the Hanle EIT resonances from small segments of the laser beam cross section. Theoretically and experimentally such resonances were obtained by sampling the transmitted laser light at various positions of the small aperture along the radius of laser beam, after the entire beam had passed through the Rb cell. It is shown that considerable absorption occurs immediately after atoms enter the laser beam. At low magnetic fields this leads to the efficient preparation into a dark state and consequent evolution with low light absorption throughout the inner region of the beam cross section. At higher magnetic fields, the initial absorption is followed by optical pumping into an uncoupled ground hyperfine level $F_g = 1$ which dominates the evolution of the atomic state throughout the laser beam cross section. The appearance of transmission minima, as sidebands to the EIT resonance, in the inner regions of the Π laser beam is due to strong dependence of optical pumping on the magnetic field. Thus, essentially different physical mechanisms, optical pumping (incoherent) in Π laser beams and Ramsey-like interference (coherent) in Gaussian laser beams, yield seemingly similar results, i.e., the appearance of the transmission minima in Hanle EIT line shapes. In addition, the observed narrowing of Hanle EIT resonances toward the center of the Π -shaped laser beam cross section is induced by population loss during the atomic transit through the laser beam. The aforementioned studies of the influence of the laser beam profile imply that for the proper modeling of experiments and identification and understanding of dominant processes affecting the atomic state evolution within the laser beam, it is essential to take into account a real beam profile.

Hanle EIA resonances at the D_2 line transition $F_g = 2 \rightarrow F_e = 3$ in ^{87}Rb

were studied using Gaussian and Π -shaped laser beams of the same radius. It is demonstrated that the atomic state experiences completely different evolution depending on whether it traverses one or the other profiled laser beam. This is shown by the Hanle EIA obtained from transmission of small segments of the entire laser beam cross-section. EIA resonances are narrower in outer regions of the Gaussian beam. In central parts of the Gaussian beam, EIA resonances are widest due to highest power broadening. For a Π -shaped laser beam, the narrowest EIA resonances are obtained at the beam center, due to transit-time narrowing of the coherent resonance. EIA amplitudes, in the range of applied laser intensities, are lowest (highest) near the laser beam center for the Gaussian (Π -shaped) profile. Thus, outer regions of the Gaussian beam and central regions of the Π -shaped beam are the most valuable regions in the sense that they contribute the narrowest linewidths and highest amplitudes to the whole-beam EIA resonance. The opposite variation of EIA linewidths with the distance from the laser beam center for the two beam profiles makes the linewidths of whole-beam EIA less dependent on the laser beam profile. The dependence of whole-beam EIA resonance linewidths on the laser intensity for the Π -shaped laser beam has a pronounced maximum which exceeds the values obtained with the Gaussian beam that yields a flat linewidths intensity dependence. Differences in EIA line shapes obtained using two laser beam profiles imply that a theory with assumed Π -shaped radial dependence (common assumption in majority of models) cannot produce good agreement with experiments done usually using a Gaussian or similar beam shape. This work has shown that it is important to take into account the real laser beam profile for proper modeling and analysis of coherent effects in alkali-metal vapors.

The last topic covered by this thesis is a general formalism for describing Stark-chirped rapid adiabatic passage among degenerate-level manifolds and the application to the ^{87}Rb atom. Cases of two and three degenerate manifolds were considered. Analysis of a degenerate-level system is facilitated by its subdivision into a set of smaller independently evolving subsystems that are related to the minimal-sized invariant subspaces of the Hamiltonian. The evolution is restricted within such invariant subspaces enabling separate analysis of each subsystem. Population transfer from the ground to the final level is considered for different types of invariant subspaces depending on the presence of dark states. It is shown that the complete transfer is feasible if the initial state is prepared into specific coherent superpositions. The developed formalism is applicable to the general case of arbitrary numbers of

degenerate states within each level and arbitrary couplings of the appropriate transitions. It represents a generalization of the Morris-Shore transformation to the case when the removed degeneracy of the sublevels leads to detuning from two-photon resonance. Applying the general formalism, SCRAP among two and three hyperfine levels in the ^{87}Rb atom is examined in detail. The formalism gives a full description of the SCRAP population transfer process and should be useful for analyzing adiabatic passage in a wide variety of atomic and molecular systems.

References

- [1] G. Alzetta, A. Gozzini, L. Moi, and G. Orriols, An experimental method for the observation of r.f. transitions and laser beat resonances in oriented Na vapour, *Il Nuovo Cimento B (1971-1996)* **36**, 5–20 (1976). 1
- [2] E. Arimondo, Coherent Population Trapping in Laser Spectroscopy, volume 35 of *Progress in Optics* pages 257–354. Elsevier (1996). 1, 12
- [3] S. E. Harris, J. E. Field, and A. Imamoglu, Nonlinear optical processes using electromagnetically induced transparency, *Physical Review Letters* **64**, 1107–1110 (1990). 1
- [4] M. Fleischhauer, A. Imamoglu, and J. P. Marangos, Electromagnetically induced transparency: Optics in coherent media, *Reviews of Modern Physics* **77**, 633–673 (2005). 1
- [5] A. M. Akulshin, S. Barreiro, and A. Lezama, Electromagnetically induced absorption and transparency due to resonant two-field excitation of quasidegenerate levels in Rb vapor, *Physical Review A* **57**, 2996–3002 (1998). 2, 46
- [6] A. Lezama, S. Barreiro, and A. M. Akulshin, Electromagnetically induced absorption, *Physical Review A* **59**, 4732–4735 (1999). 2, 46
- [7] A. V. Taichenachev, A. M. Tumaikin, and V. I. Yudin, Electromagnetically induced absorption in a four-state system, *Physical Review A* **61**, 011802 (1999). 2
- [8] C. Goren, A. D. Wilson-Gordon, M. Rosenbluh, and H. Friedmann, Electromagnetically induced absorption due to transfer of coherence and to transfer of population, *Physical Review A* **67**, 033807 (2003). 2, 46
- [9] G. Moruzzi and F. Strumia, *The Hanle effect and level-crossing spectroscopy*, Physics of atoms and molecules. Plenum Press (1991). 2

-
- [10] C. Andreeva, S. Cartaleva, Y. Dancheva, V. Biancalana, A. Burchianti, C. Marinelli, E. Mariotti, L. Moi, and K. Nasyrov, Coherent spectroscopy of degenerate two-level systems in Cs, *Physical Review A* **66**, 012502 (2002). 2
- [11] Nikolay V. Vitanov, Thomas Halfmann, Bruce W. Shore, and Klaas Bergmann, Laser-induced population transfer by adiabatic passage techniques, *Annual Review of Physical Chemistry* **52**(1), 763–809 (2001). 2, 54
- [12] N. V. Vitanov, M. Fleischhauer, B. W. Shore, and K. Bergmann, Coherent manipulation of atoms and molecules by sequential laser pulses, *Adv. Atom. Mol. Opt. Phy.* **46**, 55–190 (2001). 2, 54
- [13] L. P. Yatsenko, B. W. Shore, T. Halfmann, K. Bergmann, and A. Vardi, Source of metastable H(2s) atoms using the Stark chirped rapid-adiabatic-passage technique, *Physical Review A* **60**, R4237–R4240 (1999). 2, 62, 63
- [14] Marlan O. Scully and Michael Fleischhauer, High-sensitivity magnetometer based on index-enhanced media, *Physical Review Letters* **69**, 1360–1363 (1992). 2
- [15] Michael Fleischhauer and Marlan O. Scully, Quantum sensitivity limits of an optical magnetometer based on atomic phase coherence, *Physical Review A* **49**, 1973–1986 (1994). 2
- [16] D. Budker and M. Romalis, Optical magnetometry, *Nature Physics* **3**, 227–234 (2007). 2
- [17] M. Lindberg and R. Binder, Dark States in Coherent Semiconductor Spectroscopy, *Physical Review Letters* **75**, 1403–1406 (1995). 2
- [18] R. Wynands and A. Nagel, Precision spectroscopy with coherent dark states, *Applied Physics B: Lasers and Optics* **68**, 1–25 (1999). 2
- [19] J. Vanier, Atomic clocks based on coherent population trapping: a review, *Applied Physics B: Lasers and Optics* **81**, 421–442 (2005). 2
- [20] A. Weis and R. Wynands, Laser-based precision magnetometry in fundamental and applied research, *Optics and Lasers in Engineering* **43**(3–5), 387–401 (2005). 2

-
- [21] S. Knappe, V. Gerginov, P. D. D. Schwindt, V. Shah, H. G. Robinson, L. Hollberg, and J. Kitching, Atomic vapor cells for chip-scale atomic clocks with improved long-term frequency stability, *Optics Letters* **30**(18), 2351–2353 (2005). 2
- [22] S. Brandt, A. Nagel, R. Wynands, and D. Meschede, Buffer-gas-induced linewidth reduction of coherent dark resonances to below 50 Hz, *Physical Review A* **56**, R1063–R1066 (1997). 3
- [23] M. Klein, M. Hohensee, D. F. Phillips, and R. L. Walsworth, Electromagnetically induced transparency in paraffin-coated vapor cells, *Physical Review A* **83**, 013826 (2011). 3, 28
- [24] E. Pfleghaar, J. Wurster, S.I. Kanorsky, and A. Weis, Time of flight effects in nonlinear magneto-optical spectroscopy, *Optics Communications* **99**(5-6), 303–308 (1993). 3, 20
- [25] M. Radonjić, D. Arsenović, Z. Grujić, and B. M. Jelenković, Coherent population trapping linewidths for open transitions: Cases of different transverse laser intensity distribution, *Physical Review A* **79**, 023805 (2009). 3, 14, 20, 34
- [26] F. Levi, A. Godone, J. Vanier, S. Micalizio, and G. Modugno, Line-shape of dark line and maser emission profile in CPT, *The European Physical Journal D - Atomic, Molecular, Optical and Plasma Physics* **12**, 53–59 (2000). 3, 20, 34
- [27] A. V. Taichenachev, A. M. Tumaikin, V. I. Yudin, M. Stähler, R. Wynands, J. Kitching, and L. Hollberg, Nonlinear-resonance line shapes: Dependence on the transverse intensity distribution of a light beam, *Physical Review A* **69**, 024501 (2004). 3, 20, 34
- [28] Hervé Gilles, Bernard Cheron, Olivier Emile, Fabien Bretenaker, and Albert Le Floch, Rabi-Lorentzian Profile of an Atomic Resonance Obtained with Gaussian Beams, *Physical Review Letters* **86**, 1175–1178 (2001). 3, 20, 21, 28, 33
- [29] J. Anupriya, Nibedita Ram, and M. Pattabiraman, Hanle electromagnetically induced transparency and absorption resonances with a Laguerre Gaussian beam, *Physical Review A* **81**, 043804 (2010). 3, 20

-
- [30] T. Rickes, L. P. Yatsenko, S. Steuerwald, T. Halfmann, B. W. Shore, N. V. Vitanov, and K. Bergmann, Efficient adiabatic population transfer by two-photon excitation assisted by a laser-induced Stark shift, *The Journal of Chemical Physics* **113**(2), 534–546 (2000). 4
- [31] A. A. Rangelov, N. V. Vitanov, L. P. Yatsenko, B. W. Shore, T. Halfmann, and K. Bergmann, Stark-shift-chirped rapid-adiabatic-passage technique among three states, *Physical Review A* **72**, 053403 (2005). 4, 60, 61, 63, 71, 75, 76
- [32] Martin Oberst, Holger Münch, and Thomas Halfmann, Efficient Coherent Population Transfer among Three States in NO Molecules by Stark-Chirped Rapid Adiabatic Passage, *Physical Review Letters* **99**, 173001 (2007). 4
- [33] Martin Oberst, Holger Münch, Gayane Grigoryan, and Thomas Halfmann, Stark-chirped rapid adiabatic passage among a three-state molecular system: Experimental and numerical investigations, *Physical Review A* **78**, 033409 (2008). 4
- [34] M. Amnat-Talab, R. Khoda-Bakhsh, and S. Guérin, Quantum state engineering in a cavity by Stark chirped rapid adiabatic passage, *Physics Letters A* **359**(5), 366–372 (2006). 4
- [35] L. F. Wei, J. R. Johansson, L. X. Cen, S. Ashhab, and Franco Nori, Controllable Coherent Population Transfers in Superconducting Qubits for Quantum Computing, *Physical Review Letters* **100**, 113601 (2008). 4
- [36] James R. Morris and Bruce W. Shore, Reduction of degenerate two-level excitation to independent two-state systems, *Physical Review A* **27**, 906–912 (1983). 5, 63
- [37] A. A. Rangelov, N. V. Vitanov, and B. W. Shore, Extension of the Morris-Shore transformation to multilevel ladders, *Physical Review A* **74**, 053402 (2006). 5, 72
- [38] H. P. Breuer and F. Petruccione, *The theory of open quantum systems*, Oxford University Press New York (2002). 12

-
- [39] S. Attal, A. Joye, and C.A. Pillet, *Open Quantum Systems II: The Markovian Approach*, Lecture Notes in Mathematics. Springer (2006). 12
- [40] V. E. Tarasov, *Quantum Mechanics of Non-Hamiltonian and Dissipative Systems*, Monograph Series on Nonlinear Science and Complexity. Elsevier Science (2008). 12
- [41] Daniel A. Steck, *Quantum and Atom Optics*, available online at <http://steck.us/teaching> (revision 0.8.3), 25 May 2012. 13, 14, 15
- [42] Daniel A. Steck, *Rubidium 87 D Line Data*, available online at <http://steck.us/alkalidata> (revision 2.1.4), 23 December 2010. 18
- [43] Luigi Brugnano and Cecilia Magherini, The BiM code for the numerical solution of ODEs, *J. Comput. Appl. Math.* **164-165**(1), 145–158 (2004). 19
- [44] Ali Javan, Olga Kocharovskaya, Hwang Lee, and Marlan O. Scully, Narrowing of electromagnetically induced transparency resonance in a Doppler-broadened medium, *Physical Review A* **66**, 013805 (2002). 20
- [45] C. Y. Ye and A. S. Zibrov, Width of the electromagnetically induced transparency resonance in atomic vapor, *Physical Review A* **65**, 023806 (2002). 20
- [46] Aleksandar Krmpot, Marina Mijailović, Bratimir Panić, Dragan Lukić, Aleksander Kovačević, Dejan Pantelić, and Branislav Jelenković, Sub-Doppler absorption narrowing in atomic vapor at two intense laser fields, *Optics Express* **13**(5), 1448–1456 (2005). 20
- [47] J. Dimitrijević, D. Arsenović, and B. M. Jelenković, Intensity dependence narrowing of electromagnetically induced absorption in a Doppler-broadened medium, *Physical Review A* **76**, 013836 (2007). 20, 49
- [48] S. Knappe, M. Stähler, C. Affolderbach, A. V. Taichenachev, V. I. Yudin, and R. Wynands, Simple parameterization of dark-resonance line shapes, *Applied Physics B: Lasers and Optics* **76**, 57–63 (2003). 20
- [49] Yanhong Xiao, Irina Novikova, David F. Phillips, and Ronald L. Walsworth, Diffusion-Induced Ramsey Narrowing, *Physical Review Letters* **96**, 043601 (2006). 20, 28

-
- [50] Yanhong Xiao, Irina Novikova, David F. Phillips, and Ronald L. Walsworth, Repeated interaction model for diffusion-induced Ramsey narrowing, *Optics Express* **16**(18), 14128–14141 (2008). 20, 28
- [51] O. Firstenberg, M. Shuker, R. Pugatch, D. R. Fredkin, N. Davidson, and A. Ron, Theory of thermal motion in electromagnetically induced transparency: Effects of diffusion, Doppler broadening, and Dicke and Ramsey narrowing, *Physical Review A* **77**, 043830 (2008). 20
- [52] S. Mitra, M.M. Hossain, B. Ray, P.N. Ghosh, S. Cartaleva, and D. Slavov, On line shape of electromagnetically induced transparency in a multilevel system, *Optics Communications* **283**(7), 1500–1509 (2010). 20
- [53] A. J. Krmpot, S. M. Ćuk, S. N. Nikolić, M. Radonjić, D. G. Slavov, and B. M. Jelenković, Dark Hanle resonances from selected segments of the Gaussian laser beam cross-section, *Optics Express* **17**(25), 22491–22498 (2009). 21, 28
- [54] A. J. Krmpot, M. Radonjić, S. M. Ćuk, S. N. Nikolić, Z. D. Grujić, and B. M. Jelenković, Evolution of dark state of an open atomic system in constant intensity laser field, *Physical Review A* **84**, 043844 (2011). 21
- [55] S. M. Ćuk, M. Radonjić, A. J. Krmpot, S. N. Nikolić, Z. D. Grujić, and B. M. Jelenković, Influence of laser beam profile on electromagnetically induced absorption, *Physical Review A* **82**, 063802 (2010). 21
- [56] G. Wasik, W. Gawlik, J. Zachorowski, and W. Zawadzki, Laser frequency stabilization by Doppler-free magnetic dichroism, *Applied Physics B: Lasers and Optics* **75**, 613–619 (2002). 25
- [57] T. Petelski, M. Fattori, G. Lamporesi, J. Stuhler, and G.M. Tino, Doppler-free spectroscopy using magnetically induced dichroism of atomic vapor: a new scheme for laser frequency locking, *The European Physical Journal D - Atomic, Molecular, Optical and Plasma Physics* **22**, 279–283 (2003). 25
- [58] Z. D. Grujić, M. Mijailović, D. Arsenović, A. Kovačević, M. Nikolić, and B. M. Jelenković, Dark Raman resonances due to Ramsey interference in vacuum vapor cells, *Physical Review A* **78**, 063816 (2008). 32

-
- [59] F. Renzoni, W. Maichen, L. Windholz, and E. Arimondo, Coherent population trapping with losses observed on the Hanle effect of the D_1 sodium line, *Physical Review A* **55**, 3710–3718 (1997). 40, 44
- [60] Ferruccio Renzoni and Ennio Arimondo, Population-loss-induced narrowing of dark resonances, *Physical Review A* **58**, 4717–4722 (1998). 40, 44
- [61] C. Goren, A. D. Wilson-Gordon, M. Rosenbluh, and H. Friedmann, Atomic four-level N systems, *Physical Review A* **69**, 053818 (2004). 46
- [62] C. Goren, A. D. Wilson-Gordon, M. Rosenbluh, and H. Friedmann, Electromagnetically induced absorption due to transfer of population in degenerate two-level systems, *Physical Review A* **70**, 043814 (2004). 46
- [63] C. Goren, A. D. Wilson-Gordon, M. Rosenbluh, and H. Friedmann, Sub-Doppler and subnatural narrowing of an absorption line induced by interacting dark resonances in a tripod system, *Physical Review A* **69**, 063802 (2004). 46
- [64] C. Affolderbach, S. Knappe, R. Wynands, A. V. Taichenachev, and V. I. Yudin, Electromagnetically induced transparency and absorption in a standing wave, *Physical Review A* **65**, 043810 (2002). 46
- [65] Soo Kyoung Kim, Han Seb Moon, Kyoungdae Kim, and Jung Bog Kim, Observation of electromagnetically induced absorption in open systems regardless of angular momentum, *Physical Review A* **68**, 063813 (2003). 46
- [66] Hsiang-Shun Chou and Jörg Evers, Dressed-Atom Multiphoton Analysis of Anomalous Electromagnetically Induced Absorption, *Physical Review Letters* **104**, 213602 (2010). 46
- [67] J. Dimitrijević, D. Arsenović, and B. M. Jelenković, Coherent processes in electromagnetically induced absorption: a steady and transient study, *New Journal of Physics* **13**(3), 033010 (2011). 46
- [68] S. H. Autler and C. H. Townes, Stark Effect in Rapidly Varying Fields, *Physical Review* **100**, 703–722 (1955). 57
- [69] J. Wong, J. C. Garrison, and T. H. Einwohner, Dynamic Stark splitting by coupled one- and two-photon resonances, *Physical Review A* **16**, 213–220 (1977). 57

CURRICULUM VITAE - Milan Radonjić

Date and place of birth: 14.07.1983, Smederevska Palanka, Serbia

Education

- **(2008 - 2013)** PhD in Quantum Optics, Faculty of Physics, University of Belgrade, Serbia
- **(2002 - 2007)** BSc in Physics, Faculty of Physics, University of Belgrade, Serbia
Major: Theoretical Physics, graduated as the best in generation
BSc Thesis: "The Quantum Hall Effect in Graphene"
- **(1998 - 2002)** Mathematical High School, Kragujevac, Serbia
Graduated as the best in generation
Won a bronze medal at 33. International Physics Olympiad, Bali, Indonesia, 2002
Won a bronze medal at 18. Balkan Mathematical Olympiad, Belgrade, Serbia, 2001

Employment and Research Projects

- **(2011 - present)** National research project III45016 "Generation and characterization of nano-photon functional structures in bio-medicine and informatics"
- **(2011 - present)** National research project OI171038 "Holographic methods for generation of specific wave fronts for efficient control of quantum coherent effects in laser-atom interaction"
- **(2009 - 2011)** National research project 141003 "Quantum and optical interferometry"
- **(2009 - present)** Employed as a Research Assistant at Photonics Center, Institute of Physics, University of Belgrade, Serbia

Прилог 1.

Изјава о ауторству

Потписани-а _____ Милан Радоњић _____

број индекса _____ 10/2007 _____

Изјављујем

да је докторска дисертација под насловом

Electromagnetically Induced Coherent Effects in Laser Excited Raman Resonances in Rubidium Vapor

- резултат сопственог истраживачког рада,
- да предложена дисертација у целини ни у деловима није била предложена за добијање било које дипломе према студијским програмима других високошколских установа,
- да су резултати коректно наведени и
- да нисам кршио/ла ауторска права и користио интелектуалну својину других лица.

Потпис докторанда

У Београду, 12. 10. 2012.

Милан Радоњић

Прилог 2.

Изјава о истоветности штампане и електронске верзије докторског рада

Име и презиме аутора _____ Милан Радоњић _____

Број индекса _____ 10/2007 _____

Студијски програм _____ Класична, квантна и нанофизика _____

Наслов рада _____ Electromagnetically Induced Coherent Effects in Laser
Excited Raman Resonances in Rubidium Vapor _____

Ментор _____ др Бранислав Јеленковић _____

Потписани/а _____ Милан Радоњић _____

Изјављујем да је штампана верзија мог докторског рада истоветна електронској верзији коју сам предао/ла за објављивање на порталу **Дигиталног репозиторијума Универзитета у Београду**.

Дозвољавам да се објаве моји лични подаци везани за добијање академског звања доктора наука, као што су име и презиме, година и место рођења и датум одбране рада.

Ови лични подаци могу се објавити на мрежним страницама дигиталне библиотеке, у електронском каталогу и у публикацијама Универзитета у Београду.

Потпис докторанда

У Београду, 12.10.2012.

Милан Радоњић

Прилог 3.

Изјава о коришћењу

Овлашћујем Универзитетску библиотеку „Светозар Марковић“ да у Дигитални репозиторијум Универзитета у Београду унесе моју докторску дисертацију под насловом:

Electromagnetically Induced Coherent Effects in Laser Excited Raman Resonances in Rubidium Vapor

која је моје ауторско дело.

Дисертацију са свим прилозима предао/ла сам у електронском формату погодном за трајно архивирање.

Моју докторску дисертацију похрањену у Дигитални репозиторијум Универзитета у Београду могу да користе сви који поштују одредбе садржане у одабраном типу лиценце Креативне заједнице (Creative Commons) за коју сам се одлучио/ла.

1. Ауторство

- Ауторство - некомерцијално
- Ауторство –некомерцијално –без прераде
- Ауторство –некомерцијално –делити под истим условима
- Ауторство –без прераде
- Ауторство –делити под истим условима

(Молимо да заокружите само једну од шест понуђених лиценци, кратак опис лиценци дат је на полеђини листа).

Потпис докторанда

У Београду, 12.10.2012.

Милан Задочич

1. Ауторство - Дозвољаваате умножавање, дистрибуцију и јавно саопштавање дела, и прераде, ако се наведе име аутора на начин одређен од стране аутора или даваоца лиценце, чак и у комерцијалне сврхе. Ово је најслободнија од свих лиценци.

2. Ауторство – некомерцијално. Дозвољаваате умножавање, дистрибуцију и јавно саопштавање дела, и прераде, ако се наведе име аутора на начин одређен од стране аутора или даваоца лиценце. Ова лиценца не дозвољава комерцијалну употребу дела.

3. Ауторство - некомерцијално – без прераде. Дозвољаваате умножавање, дистрибуцију и јавно саопштавање дела, без промена, преобликовања или употребе дела у свом делу, ако се наведе име аутора на начин одређен од стране аутора или даваоца лиценце. Ова лиценца не дозвољава комерцијалну употребу дела. У односу на све остале лиценце, овом лиценцом се ограничава највећи обим права коришћења дела.

4. Ауторство - некомерцијално – делити под истим условима. Дозвољаваате умножавање, дистрибуцију и јавно саопштавање дела, и прераде, ако се наведе име аутора на начин одређен од стране аутора или даваоца лиценце и ако се прерада дистрибуира под истом или сличном лиценцом. Ова лиценца не дозвољава комерцијалну употребу дела и прерада.

5. Ауторство – без прераде. Дозвољаваате умножавање, дистрибуцију и јавно саопштавање дела, без промена, преобликовања или употребе дела у свом делу, ако се наведе име аутора на начин одређен од стране аутора или даваоца лиценце. Ова лиценца дозвољава комерцијалну употребу дела.

6. Ауторство - делити под истим условима. Дозвољаваате умножавање, дистрибуцију и јавно саопштавање дела, и прераде, ако се наведе име аутора на начин одређен од стране аутора или даваоца лиценце и ако се прерада дистрибуира под истом или сличном лиценцом. Ова лиценца дозвољава комерцијалну употребу дела и прерада. Слична је софтверским лиценцама, односно лиценцама отвореног кода.